Engineering Strong-Field Phenomena: From Attosecond Pulse Characterization to Nanostructured Electron Emitters

by

Phillip D. Keathley

Submitted to the Department of Electrical Engineering and Computer Science
in partial fulfillment of the requirements for the degree of

Doctor of Philosophy

at the

MASSACHUSETTS INSTITUTE OF TECHNOLOGY

September 2015

Author .....
Department of Electrical Engineering and Computer Science
August 27, 2015

Certified by .....
Franz X. Kärtner
Adjunct Professor
Thesis Supervisor

Accepted by .....
Leslie A. Kolodziejski
Chair, Department Committee on Graduate Students

Engineering Strong-Field Phenomena: From Attosecond Pulse Characterization to Nanostructured Electron Emitters

by

Phillip D. Keathley

Submitted to the Department of Electrical Engineering and Computer Science
on August 27, 2015, in partial fulfillment of the
requirements for the degree of
Doctor of Philosophy

Abstract

Strong-field phenomena are a driving force behind the latest innovations in ultrafast science. As ultrafast laser sources improve in terms of peak pulse energy and wavelength tunability, applications that utilize high peak electromagnetic field strengths to generate attosecond pulses of both photons and electrons are becoming readily available. Furthermore, through the coupling of these optical fields to nanostructures that further enhance peak field strengths, a new generation of electron emitters and "light-speed" electronics are now emerging. This thesis explores two such areas in detail: the generation and characterization of attosecond pulses of light, and strong-field photoemission from nanostructures.

Thesis Supervisor: Franz X. Kärtner
Title: Adjunct Professor

Acknowledgments

There are many who have contributed to this thesis, both directly and indirectly. First, I would like to thank my advisor Franz Kärtner. He has been the one constant throughout my many projects, brimming over with a never-ending supply of enthusiasm and encouragement. There is not a word that can quantify his optimism. Man has walked on the moon because of those like Franz.

Alexander Sell was the definition of a colleague. I can never thank him enough for providing me with a proper training in experimental optics.

I would like to thank Siddharth Bhardwaj for the many hours of discussion on atomic physics, quantum mechanics, wave packets and politics. Much of my work on attosecond pulse retrieval and modeling electron emission from nanostructures came from these conversations.

Working with Guillaume Laurent reminded me that a job worth doing is worth doing right. His meticulous attention to detail and emphasis on quality over quantity has reminded me why I started doing research to begin with. Godspeed Guillaume.

Michael Swanwick and Richard Hobbs have been a tremendous joy to work with. Beyond fabricating beautiful structures, they were always quick to provide a helping hand with anything in the laboratory.

Billy Putnam heavily influenced much of my understanding of strong-field electron emission, and was a great resource on all things physics.

In recent months, I have also enjoyed many wonderful conversations with Greg Stein. His enthusiasm for all manner of intellectual pursuits, from physics to Emacs, is a true source of inspiration.

To all the other members of the group with whom I have overlapped, thank you for the many memories I have made with you over the last six years. It was not always easy, but it was a truly rewarding and fruitful experience.

Thanks to Profs. Qing Hu and Erich Ippen for taking the time to serve on my thesis committee, and for providing me with valuable insights and suggestions.

I would like to also thank my family. My mother, brother and grandparents have always been supportive of my goals, no matter how far they have lead me away from them. Finally, none of this would have been possible without the constant support and companionship of my wife Yugu.

Contents

List of Figures

Chapter 1

Introduction

Research into strong-field (SF) driven electron dynamics has grown rapidly in the last two to three decades as laser sources producing peak electric fields capable of directly tunnel-ionizing atomic gases have become readily available. A key technology stemming from this work is the generation and control of attosecond pulses of extreme ultraviolet (EUV) light [1–9]. As stroboscopic light sources enabled the study of mechanical motion not directly observable by the naked eye, such technology enables the direct observation of electron motion within atoms and molecules. While attosecond science and SF phenomena have traditionally been studied in the realm of atomic and molecular systems, with growing advances and interest in nanotechnology, recent developments have emerged in the area of SF-driven electron emission from nanostructuress [10–16]. Such systems utilize the field-enhancement properties of nanostructures to achieve optical tunneling before the onset of structural damage due to peak average power.

This thesis presents two main contributions of the author: the development of the Volkov Transform Generalized Projections Algorithm (VTGPA), a new algorithm for attosecond EUV pulse characterization, and a thorough characterization of SF photoemission from nanostructured silicon cathodes. As both draw heavily from the use of the strong-field approximation (SFA) in quantum mechanics, it is discussed in detail in Chapter 2. Chapters 3-5 then go on to present the authors contributions to the fields of attosecond pulse characterization and SF emission

from nanostructures. To provide the reader with historical context, sections 1.1 and 1.2 below provide a more detailed introduction to each area. Finally, the thesis is concluded and outlook provided in Chapter 6.

1.1 The Attosecond Pulse

The first steps toward the development of attosecond pulses were taken with the discovery of high harmonic generation (HHG) of EUV light in rare gases over two decades ago [17–20]. While it was clear for many years that the physics predicted that the HHG process was generating trains of pulses just attoseconds in duration, it was necessary to develop new and improved temporal characterization techniques having the ability to measure such pulse durations before it could be confirmed experimentally. The best candidates for the characterization of such optical pulses came in the form of an electron streaking apparatus [2, 21–25]. As the photoionization process from a well defined initial state, such as that found in an atom, is coherent with respect to the ionizing EUV pulse, the magnitude and phase information of the EUV pulse is preserved during ionization. If ionization occurs within the presence of a long-wavelength, e.g. infrared (IR), pulse, the electron phase becomes modulated depending on its birth time within the IR pulse. Thus, by collecting spectra as a function of delay between the IR and EUV pulses, forming what is known as a spectrogram, one has enough information to completely reconstruct the original EUV pulse in time.

Such a measurement necessitates a precision optical delay-line coupled with a vacuum apparatus for the generation of EUV and measurement of electron spectra. A standard attosecond metrology setup is shown in Figure 1-1 below, and the design implemented in the Kärtner group at MIT is discussed in detail in Section 3.4. Both designs share key aspects of any attosecond metrology station:

- HHG generation chamber with gas cell. This chamber needs to withstand high gas flow from the HHG target.

- Delay line allowing for in-vacuum propagation of EUV pulses as they are readily absorbed at atmospheric pressures.
- Differential pumping to isolate spectroscopy chamber from HHG gas. This reduces background when the HHG gas differs from the target gas, and protects the sensitive microchannel plate detectors in the electron spectrometer from ion-induced arcing.
- Fine delay control for streaking. In Figure 1-1, it is a piezo that drives the central portion of the split mirror.
- Electron spectrometer (e.g. time of flight, velocity map imager (VMI), etc.).
- EUV spectrometer for diagnostics and calibration.

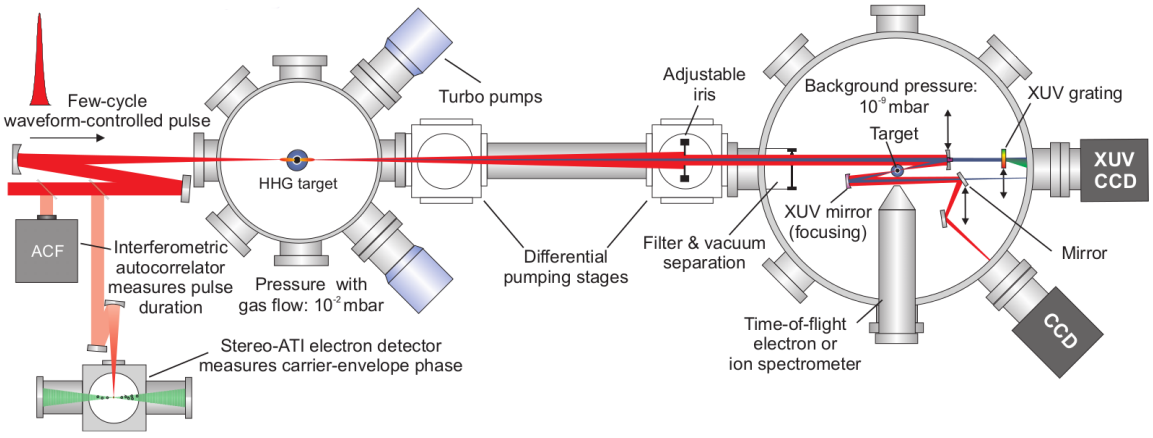

Figure 1-1: Schematic of a typical attosecond metrology station. Image adapted from [4]

An example of an experimentally measured spectrogram for an isolated attosecond pulse is shown in Figure 1-2. While there is enough information within the spectrogram to characterize both the EUV and IR streaking pulses, care has to be taken in the techniques and assumptions used to retrieve it. One attractive method combines a technique from ultrafast laser physics, known as frequency resolved optical gating (FROG), with the SF formulation of ionization and streaking of the electron, known as FROG for the complete retrieval of attosecond bursts (FROG-CRAB) [21, 23]. In the community, this technique is popular as it enables

the simultaneous characterization of both the IR and EUV pulses. While powerful, in its current form there is still much room for improvement. For instance, magnitude and phase changes during the ionization step are typically ignored, and the algorithm itself suffers from a reliance on Fourier transforms, which poorly models the physical process of streaking.

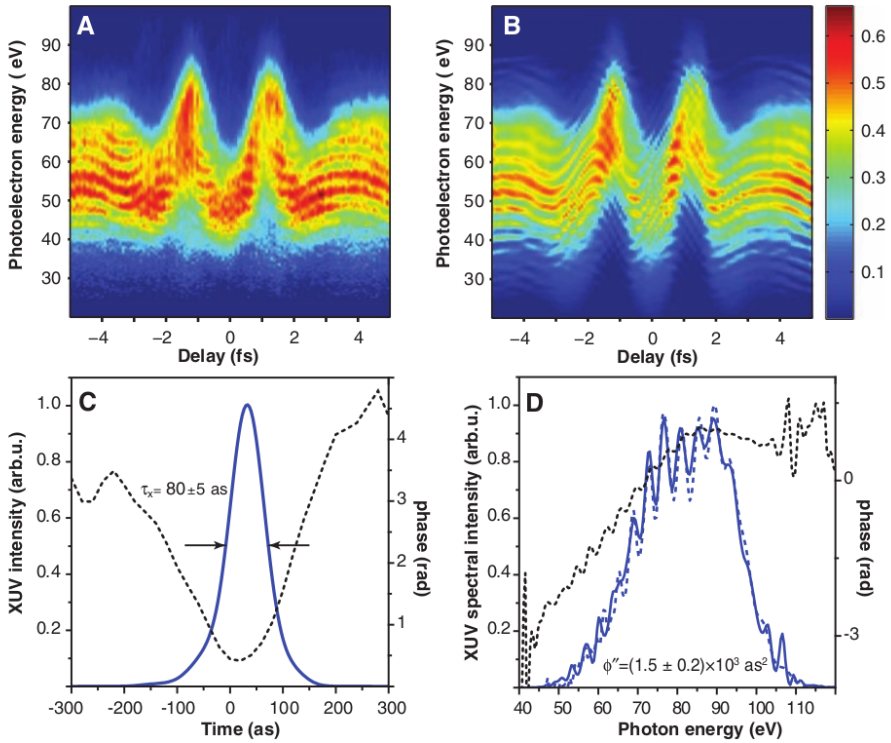

Figure 1-2: Example of an experimentally retreived spectrogram. Measured (a) and retrieved (b) spectrograms. Retrieved pulse form with phase (c), measured spectrum with phase (d). Image adapted from [3].

Others have investigated solutions to this problem by requiring relatively long and weak streaking pulses, ensuring that the process falls within the regime of a single EUV photon absorption followed by single IR photon absorption/emission [24, 25]. In this regime, the attosecond pulse can be retrieved by analyzing the magnitude and phase of oscillations in the spectrogram at the frequency of the streak pulse, hence the name phase retrieval by omega oscillation filtering (PROOF). While attractive for its speed and simplicity, it does not offer a solution that can simultaneously solve for the kinds of ultra-broadband, complex waveforms that

often accompany SF physics experiments, as well as the EUV pulse. In chapter 3 of this proposal, the VTGPA is presented, which completely solves the pulse retrieval problem within the context of the SF approximation without any further assumptions. Beyond its application to the problem of attosecond pulse retrieval, the general approach of the algorithm should prove useful for analyzing experimental results from SF driven pump-probe measurements that obey similar physics. Also, as it can be used at weaker streaking intensities, much can be learned about the general applicability of the SF approximation in describing attosecond streaking measurements versus perturbation theory by comparing the results to other methods such as iPROOF [24] or RABBITT [2]. This makes the VTGPA a potentially useful tool for studying and improving common assumptions used in SF physics.

1.2 Strong-Field Emission From Nanostructures

Aside from attosecond pulses of light, another area of rapidly growing interest is the formation of high-yield, ultrafast electron bursts from nanostructured cathodes [10–15, 26]. While the optical tunneling process utilized in HHG and above threshold ionization (ATI) from atoms [27, 28] is not limited to gaseous targets, it is not typically observed in solids due to the onset of material damage and/or a space-charge induced virtual cathode. However, field-driven electron oscillations and bunching within nanostructures cause the incident electric field from an optical pulse to be enhanced upwards of $(10-50)\times$. Given that the maximum field enhancement observable from a planar substrate is just $2\times$, if we assume a field enhancement factor of $20\times$ for a nanostructure, an increased peak local intensity of $100\mathrm{I}_0$, where I_0 is peak input intensity, is induced, avoiding damage from high average power absorption. Furthermore, due to the localization of the emission and laser acceleration from a curved emission site, average current density is reduced and the transverse electron energy spread is increased, thereby preventing the formation of a space-charge-induced virtual cathode [29].

Chapter 5 compares theoretical and experimental results of electron emission

from nanostructures in the presence of strong optical fields (i.e. exceeding 10^9 V/m). At low peak intensities, the electron emission follows the trend of multiphoton emission from planar surfaces, having a current yield that scales with the N^{th} power of peak intensity, where N is the required number of photons needed to promote an electron to the vacuum. However, at higher peak intensities the electron sees an increased potential barrier due to the enhanced field on the outer surface of the emitter equal to the ponderamotive potential, U_p, of the enhanced laser field. This leads to a sharp kink in the electron emission rate, and the emitter then starts to enter the tunneling, or SF regime of photoemission. Expressed in a time domain picture, this is when the tunneling time, $T_t = \sqrt{2m\phi}/(eF)$, is shorter than one optical cycle of the incident pulse [30]. In the expression for T_t, m is the electron mass, ϕ the material work function, e the electron charge and F the peak electric field. Beyond the total yield, the effects of laser acceleration and rescattering on the emitted electron energy spectra are discussed in the context of both a semi-classical quantum model and its relation to purely classical trajectories.

In Chapter 5, a complete theoretical framework describing SF emission from nanostructures is covered, and a full experimental characterization presented. In section 5.3, experimental measurements that characterize electron yield and spectra as a function of input intensity from arrays of nano-sharp Si tips are presented. These results strongly support the observation of SF emission from the nanostructures, as both the kink in electron yield and broad energy plateaus due to rescattering from the tip are observed. To further demonstrate that the emission is truly a field-driven process, two-color measurements are presented which demonstrate how the electron energy spectra can be significantly altered due to a change in form of the electric field waveform and confirm the ultrafast nature of the emission process.

Chapter 2

Theoretical Methods

In order to deal with the emission and subsequent propagation of an electron in a "strong", oscillating electric field, it is advantageous to introduce the fundamental solutions to the Schrödinger equation under such a condition. In section 2.1, the dipole Gordon-Volkov solution to the wave function in the presence of oscillating electric fields is presented. In section 2.2, SF perturbation theory is introduced and used to solve for electron emission, subsequent acceleration, and interaction with the coulomb potential in a uniform laser field. Section 2.2.2 then concludes the chapter with a discussion of the saddle point approximation and how it can be used to simplify the calculation of the integrals presented in section 2.2. These results will be continued in later chapters to develop models for EUV ionization and streaking, as well as SF photoemission from nanostructures.

2.1 Dipole Gordon-Volkov Solutions

The dipole Gordon-Volkov solution to the Schrödinger equation was developed almost a century ago by Gordon [31] and Volkov [32] to give a quantum mechanical description of a charged particle within an oscillating electric field. To start this derivation, we first make the dipole approximation, which assumes that the electric field is infinite in extent with no spatial distribution (i.e. it is only a function of time). From there, we can write the general Hamiltonian of an electron in such a

system as

$$H = \frac{1}{2m}(\mathbf{p} + q\mathbf{A}(t))^2 - q\phi(\mathbf{r}, t), \tag{2.1}$$

where $\mathbf{A}(t)$ is the magnetic vector potential, $\phi(\mathbf{r}, t)$ the scalar potential, $\mathbf{p}$ the momentum vector, q the absolute value of the electron charge, and m the mass of the electron. Choosing to set $\mathbf{A}(t) = 0$, it can be easily shown that $\phi(\mathbf{r}, t) = -\mathbf{r} \cdot \mathbf{F}(t)$, where $\mathbf{F}(t)$ is the electric field as a function of time. This yields the Hamiltonian in what is called the length gauge.

$$H^l = \frac{1}{2m}\mathbf{p}^2 + q\mathbf{r} \cdot \mathbf{F}(t) \tag{2.2}$$

If, however, it is solved by setting $\phi = 0$, one has the Hamiltonian in what is called the velocity gauge,

$$H^v = \frac{1}{2m}(\mathbf{p} + q\mathbf{A}(t))^2, \tag{2.3}$$

where the electric field is given as $\mathbf{F}(t) = -\partial\mathbf{A}(t)/\partial t$. One can then move back and forth between solutions in either gauge by using the unitary gauge transformation,

$$\psi^l(\mathbf{r}, t) = \psi^v(\mathbf{r}, t)\, e^{iq\mathbf{r}\cdot\mathbf{A}(t)/\hbar}. \tag{2.4}$$

The reader may be curious at this point why an oscillating magnetic field, $\mathbf{B}$, which would likely accompany any oscillating electric field, has yet to be mentioned. By enacting the dipole approximation, we have already eliminated the magnetic field. Since $\mathbf{B} = \nabla \times \mathbf{A}$, and $\mathbf{A}$ is assumed to depend explicitly on time, there can be no magnetic field. In Appendix A it is shown that this approximation is justified unless relativistic energies are achieved during acceleration by the electric field.

It is easiest to solve for the Gordon-Volkov solution in the velocity guage. In the momentum domain, the Schrödinger equation can be written as

$$i\hbar\frac{\partial}{\partial t}\tilde{\psi}(\mathbf{p}, t) = \frac{1}{2m}(p + q\mathbf{A}(t))^2\tilde{\psi}(\mathbf{p}, t), \tag{2.5}$$

which has the solution

$$\tilde{\psi}(\mathbf{p}, t) = \exp\left\{\frac{-i}{2\hbar m}\int^{t} d\tau\big(\mathbf{p} + q\mathbf{A}(\tau)\big)^2\right\}. \tag{2.6}$$

The action term,

$$S_{\mathbf{p}}(t) = \frac{1}{2m}\int^{t} d\tau\,(\mathbf{p} + q\mathbf{A}(\tau))^2\,, \tag{2.7}$$

in equation (2.6) accounts for the accumulated phase of the electron as it is accelerated in the electric field. This solution is then used to develop a complete basis [33] such that any wave packet in an oscillating electric field can be described as a summation of momentum components with coefficients $\tilde{B}(\mathbf{p})$ as

$$\psi(\mathbf{r}, t) = \int d^3\mathbf{p}\tilde{B}(\mathbf{p})\psi_{\mathbf{p}}^{Vv}(\mathbf{r}, t), \tag{2.8}$$

where

$$\psi_{\mathbf{p}}^{Vv}(\mathbf{r}, t) = (2\pi)^{-3/2}\exp\left\{\frac{i}{\hbar}\mathbf{p}\cdot\mathbf{r} - \frac{i}{\hbar}S_{\mathbf{p}}(t)\right\} \tag{2.9}$$

is the Gordon-Volkov solution for a plane wave in the velocity gauge. One can simply use the gauge transformation in equation (2.4) to switch to the length gauge form.

If the electric field is turned off by setting $\mathbf{A}(t) = 0$, $\psi_{\mathbf{p}}^{Vv}$ simply reduces to the plane wave solution for the case of no external potential. When $\mathbf{A}(t)$ is weak, i.e. when the electric field strength is small and/or the photon energy, $\hbar\omega$, large, as it is for many SF applications, one can treat the electric field as a perturbation during the emission process and use a summation of field-free plane waves as the basis set to describe the emitted wave packet in the continuum. However, the Gordon-Volkov wave becomes a valuable tool when modeling processes driven by long-wavelength fields where the electric field is often relatively large. In this case, it is not efficient to express the wave packet as a summation of field-free plane waves. This can be mathematically demonstrated by taking $\mathbf{A}(t) = \mathbf{A}_0\cos(\omega t)$ and expanding the Volkov wave solution above as a series of field-free plain waves,

which yields [34]

$$\psi_{\mathbf{p}}^{Vv}(\mathbf{r},t) = (2\pi)^{-3/2} e^{i\mathbf{p}\cdot\mathbf{r}/\hbar} \sum_{n=-\infty}^{\infty} e^{-i[(p^2+U_p)/(2\hbar m)+n\omega]t} \times J_n\left(\frac{q\mathbf{A}_0\cdot\mathbf{p}}{(\hbar m\omega)}, \frac{U_p}{(2\omega\hbar)}\right), \tag{2.10}$$

where $J_n(u,v)$ are the generalized Bessel functions, and $U_p = q^2F_0^2/(4m\omega^2)$ is the average kinetic drift energy of the electron over one cycle of a continuous wave electric field given a peak field strength F_0, also referred to as the ponderomotive potential. As the ratio of $\mathbf{A}_0/\omega$, and thus the excursion length of the electron, increases, more and more field-free plane waves need to be used to express the information contained in just one Volkov wave (see Figure 2-1). When this is the case, it becomes advantageous to set up a perturbation theory solution to the Schödinger equation using the Volkov states as the unperturbed basis set. This is discussed in Section 2.2.

2.2 Strong-Field Perturbation Theory

A typical approach to using the Gordon-Volkov solution to solve real-world problems is known as SF perturbation theory. Perturbation theory normally treats the states of the system as the unperturbed basis set and the oscillating electric field as a perturbation. For instance, the typical derivation of a single-photon absorption leading to the photoelectric effect is derived in this manner. On the other hand, SF perturbation theory treats the binding potential and/or laser interaction potential as a perturbation and the states of the oscillating electric field, i.e. the Gordon-Volkov solutions, as the unperturbed basis set. Some basic concepts of this approach are derived below. If the reader has further interest in the topic, he or she is directed to an excellent review by Becker et al. [27], book by Joachain et al. [35], or the PhD thesis of Bhardwaj [36].

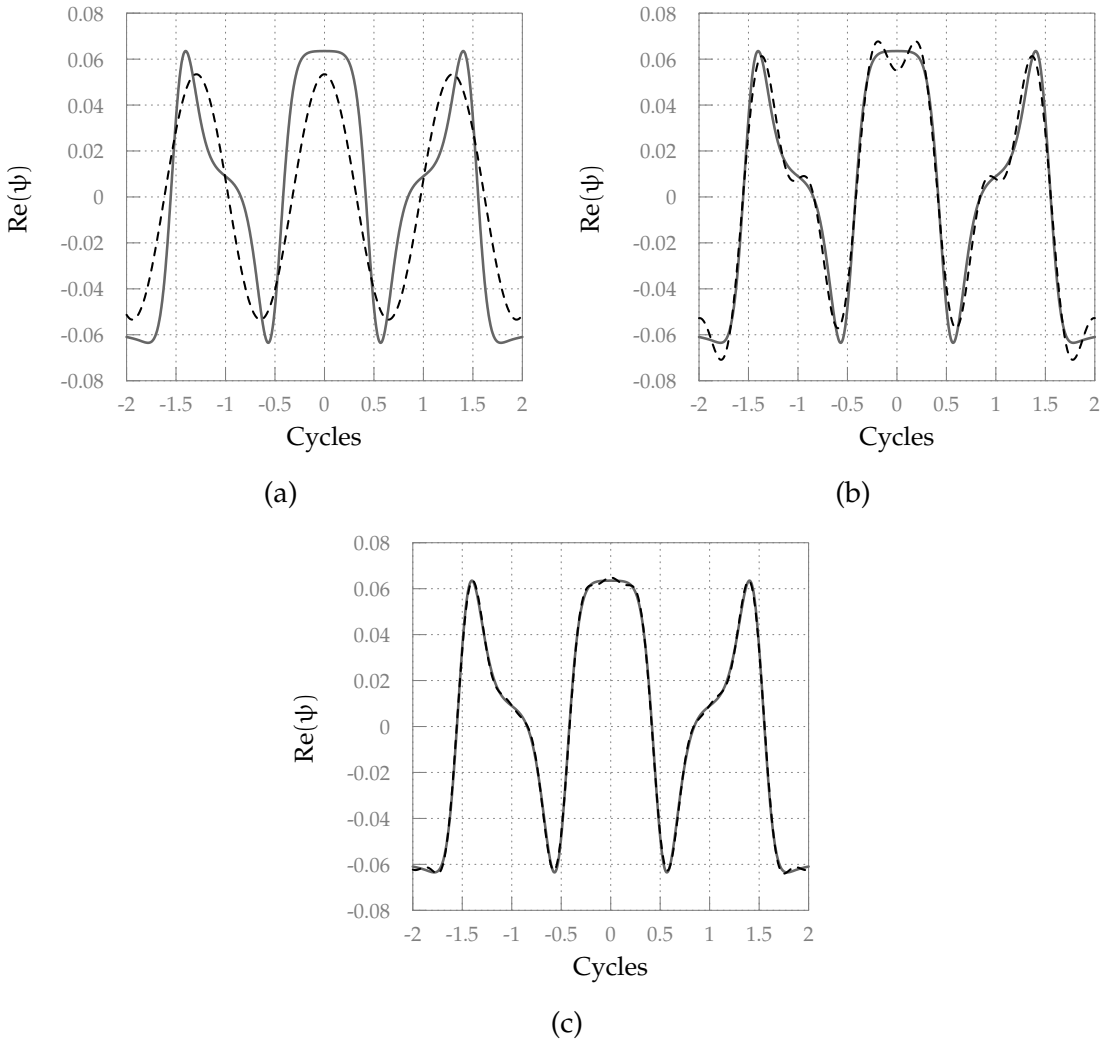

Figure 2-1: Calculation of $\mathrm{Re}(\psi_{\mathbf{p}}^{V\nu})$ using the Volkov wave solution (solid grey), and also the series expansion (dashed black) with (a) only the zeroth order term included, (b) the $-1 \leqslant n \leqslant 1$ terms included, and (c) the $-2 \leqslant n \leqslant 2$ terms included. The calculation was performed using a central wavelength of 800 nm, a peak electric field strength of 5 GeV/m, and an average electron energy of $p^2/2m = 1$ eV.

2.2.1 General Solution

To determine the probability amplitude, $M_{\mathbf{p}}$, of an electron transition to a final state $\left|\psi_{\mathbf{p}}(t)\right\rangle$ from an unexcited state, $|\psi_0(t_0)\rangle$, one can propagate the unexcited state to time t and then project it onto the final state. This is expressed mathematically as

$$M_{\mathbf{p}} = \left\langle \psi_{\mathbf{p}}(t) \right| U(t, t_0) \left| \psi_0(t_0) \right\rangle , \tag{2.11}$$

where $U(t, t_0)$ is the time propagator for the full system. In most cases, and in the following examples, only the initial state of the most weakly bound electron is considered since it contributes the most to the final transition probability. This is often referred to as the single active electron (SAE) approximation.

For the case of a system with a binding potential described by V exposed to a uniform, oscillating electric field potential $V_F(t) = q\mathbf{r} \cdot \mathbf{F}(t)$, we have the total Hamiltonian, in the length gauge, as being

$$H_T(t) = K + V + V_F(t), \tag{2.12}$$

where $K = \frac{-\hbar^2}{2m}\nabla^2$. The choice of gauge is important as an approximation to the full solution of the Schrödinger equation will be made shortly, thus breaking gauge invariance. It has been shown elsewhere that the length gauge best encapsulates the physics of ionization and acceleration in a strong field [35, 37]. If we treat the laser as the interaction Hamiltonian, the time evolution operator of the system, $U(t, t_0)$, can be written as,

$$U(t, t_0) = U_V(t, t_0) - \frac{i}{\hbar}\int_{t_0}^{t} U_V(t, t_0)V_F(\tau)U(\tau, t_0)d\tau \tag{2.13}$$

where $U_V(t, t_0)$ is the time evolution operator of the ground state system without the laser field. However, we can also write an equivalent expression, only this time treating the binding potential as the perturbation,

$$U(t, t_0) = U_F(t, t_0) - \frac{i}{\hbar}\int_{t_0}^{t} U_F(t, t_0)V_F(\tau)U(\tau, t_0)d\tau, \tag{2.14}$$

where

$$U_F(t, t_0) = \frac{1}{\hbar}\int d^3\mathbf{p} \left|\psi_{\mathbf{p}}^{V_v}(t)\right\rangle \left\langle\psi_{\mathbf{p}}^{V_v}(t_0)\right| \tag{2.15}$$

is the time evolution operator of the laser field alone. While equations (2.13) and (2.14) are complete, they are not trivial to solve. The method often employed is to use both expressions to generate a Dyson series of nested integrals that can be

truncated. Performing this up to a second order approximation yields

$$\begin{aligned} U^{(2)}(t,t_0) &= U_V(t,t_0) - \frac{i}{\hbar}\int_{t_0}^{t} d\tau U_F(t,\tau)V_F(\tau)U_V(\tau,t_0) \\ &\quad -\frac{1}{\hbar^2}\int_{t_0}^{t} d\tau \int_{\tau}^{t} d\tau' U_F(t,\tau')VU_F(\tau',\tau)V_F(\tau)U_V(\tau,t_0). \end{aligned} \tag{2.16}$$

From here, the final state $\left|\psi_{\mathbf{p}}(t)\right\rangle$ is taken to be a Gordon-Volkov wave in the length gauge, $\left|\psi_{\mathbf{p}}^{Vl}(t)\right\rangle$, and the approximation in equation (2.16) is combined with equations (2.11) and (2.15) to yield the following second order approximation to $M_{\mathbf{p}}$ for a linearly polarized electric field $\mathbf{F}(t) = (F(t), 0, 0)$,

$$M_{\mathbf{p}} = M_{\mathbf{p}}^{(1)} + M_{\mathbf{p}}^{(2)} \tag{2.17}$$

$$M_{\mathbf{p}}^{(1)} = -\frac{i}{\hbar}\int_{-\infty}^{\infty} d\tau \exp\{i(S_{\mathbf{p}}(\tau) + W_0\tau)/\hbar\} q F(\tau) d_{(\mathbf{p}+q\mathbf{A}(\tau))} \tag{2.18}$$

$$\begin{aligned} M_{\mathbf{p}}^{(2)} = &-\frac{1}{\hbar^2}\int_{-\infty}^{\infty} d\tau q F(\tau) e^{iW_0\tau/\hbar} \int_{\tau}^{\infty} d\tau' \exp\{iS_{\mathbf{p}}(\tau')/\hbar\} \\ &\times \frac{1}{\hbar^3}\int_{-\infty}^{\infty} d^3\mathbf{k} \left\langle \mathbf{p} + q\mathbf{A}(\tau')\right| V \left|\mathbf{k} + q\mathbf{A}(\tau')\right\rangle \\ &\times \exp\left\{\frac{i}{\hbar}\left[S_{\mathbf{k}}(\tau) - S_{\mathbf{k}}(\tau')\right]\right\} d_{(\mathbf{k}+q\mathbf{A}(\tau))}. \end{aligned} \tag{2.19}$$

The term $d_{\mathbf{p}} = \langle p|\, x\, |\psi_0\rangle$ is the dipole transition matrix element from the ground state to an excited state with final momentum $\mathbf{p}$ after the field vanishes, and W_0 is the ground state energy of the system.

While the expression seems complicated, it has a simple physical explanation. For the first order term, an electron is born at time τ after which it is accelerated by the laser field in the continuum, achieving a final momentum $\mathbf{p}$. The total probability is then given by integrating over all possible birth times τ. Electrons emitted in this manner are refered to as "direct" electrons since they do not interact with the coulomb potential. For the second order term, an electron is born at time τ to a state that would have a final momentum $\mathbf{k}$ if it were not to interact with the coulomb potential. However, an interaction with the coulomb potential, V, at time τ' occurs, after which the electron transitions to a new state with final momentum

$\mathbf{p}$. The total probability is then given by integrating over all possible birth times τ, initial state momentum values $\mathbf{k}$, and interaction times τ'. One can of course continue the perturbation theory expansion to even higher terms, each describing yet another interaction with the coulomb potential.

The computational expense of calculating $M_{\mathbf{p}}$ as written in equations (2.17)-(2.19) is reduced significantly for few-cycle optical pulses as the integral only needs to be calculated over a very narrow region of time. For pulses with a large number of cycles, it suffices to approximate the pulse as a CW field where one can quantize the absorption/emission process using the generalized Bessel function expansion demonstrated in equation (2.10), thus reducing the integration bounds to only one temporal cycle of the electric field.

2.2.2 The Saddle Point Approximation

The saddle point approximation is often employed in the calculation of the integrals in equations (2.18) and (2.19). The results of this approach demonstrate the deep relationship between the quantum and classical physics during the ionization and subsequent acceleration of an electron wave packet driven by a strong electric field. The saddle point approximation, often referred to as the stationary phase approximation in optics, simply takes advantage of the fact that the dominant contributions to an integral of a function with an oscillating phase are from regions when the phase is stationary with respect to the variable being integrated. Likewise, regions where the phase varies rapidly make negligible contributinos to the total integral.

For example, consider a function of the form

$$\Gamma = \int_{-\infty}^{\infty} f(x)\, e^{ig(x)}\, dx. \tag{2.20}$$

If $f(x)$ varies slowly with respect to $e^{ig(x)}$, we can isolate a location x_0 where $g(x)$

is stationary by using the condition

$$\left.\frac{\partial g(x)}{\partial x}\right|_{x_0} = 0. \tag{2.21}$$

Expanding $g(x)$ around x_0 yields

$$g(x) \approx g(x_0) + \left.\frac{\partial^2 g(x)}{\partial x^2}\right|_{x_0} \frac{(x-x_0)^2}{2} \tag{2.22}$$

and we can place this back into the integral. Since $f(x)$ varies slowly with respect to the phase, we can assume $f(x) \approx f(x_0)$ near x_0, requiring that

$$\int_{-\infty}^{\infty} \exp\left\{ i \left.\frac{\partial^2 g(x)}{\partial x^2}\right|_{x_0} \frac{(x-x_0)^2}{2} \right\} dx = \sqrt{\frac{2\pi i}{\left.\frac{\partial^2 g(x)}{\partial x^2}\right|_{x_0}}} \tag{2.23}$$

converges rapidly around x_0. Thus, if the above mentioned conditions all hold, we have the following approximation to Γ if there is only one stationary point, x_0

$$\Gamma \approx f(x_0)\, e^{i g(x_0)} \sqrt{\frac{2\pi i}{\left.\frac{\partial^2 g(x)}{\partial x^2}\right|_{x_0}}}. \tag{2.24}$$

If there are multiple stationary points in $g(x)$, then the approximation to Γ becomes a sum of this result for each stationary point in $g(x)$.

For a strong enough electric field strength such that the Keldysh parameter [30], $\gamma = \sqrt{W_0/(2U_p)}$, is less than unity [20, 27, 30], it is natural to employ the saddle point method to approximate $M_{\mathbf{p}}$ [20, 27, 28]. For instance, the stationary phase points of $M_{\mathbf{p}}^{(2)}$ require the following conditions:

$$\frac{[\mathbf{k} + q\mathbf{A}(\tau)]^2}{2m} = -W_0, \tag{2.25}$$

$$\int_{\tau'}^{\tau} dt' \frac{[\mathbf{k} + q\mathbf{A}(t')]}{m} = 0, \tag{2.26}$$

$$\frac{[\mathbf{p} + q\mathbf{A}(\tau')]^2}{2m} = \frac{[\mathbf{k} + q\mathbf{A}(\tau')]^2}{2m}. \tag{2.27}$$

Solving this system yields saddle points at τ_0, τ_0' and $\mathbf{k}_0$. The first condition requires energy conservation at the time of emission. The second requires that after emission, the total excursion distance is 0, i.e. the electron returns to its "birth" location. The third requires that the interaction with the parent system is an elastic scattering, as the incoming kinetic energy is equal to the outgoing kinetic energy. Thus, the dominant contributions describe a particle having some probability of being injected into the continuum at a distinct time τ_0, following the classical trajectory in the laser field, returning to the parent system at some time τ_0' with momentum $\mathbf{k}_0$, elastically scattering from the parent system and then following the classical trajectory again away from the parent system. The same method can be used to approximate $M_{\mathbf{p}}^{(1)}$, which yields saddle points fulfilling the condition in equation (2.25), and simply describes an emission event at some distinct time τ_0 followed by the classical trajectory in the laser field.

The saddle point approximation yields an emission probability that matches well with a time-averaged quasi-static tunneling model [30, 38]. This provides the motivation behind semi-classical models such as the Simpleman approach [13–15, 27] where, aside from the initial tunneling emission, the electron is treated as a classical particle during the laser acceleration and rescattering process. Quantum interferences can be accounted for by including the appropriate action phase contribution for every classical trajectory [15]. Thus, for the case of the Simpleman model, the portion of the electron spectrum due to rescattered electrons, $P_{scat}(W)$, can be expressed mathematically as

$$P_{scat}(W) = \left| \sum_j \left\{ \sqrt{J(\tau_0^{(j)})} R(\tau'^{(j)}_0) \exp\left(i\theta(\tau_0^{(j)}, \tau'^{(j)}_0) \right) \right\} \right|^2 \tag{2.28}$$

where W is the final kinetic energy, $J(t)$ is the tunneling rate for the laser field at time t, $R(t)$ is the reflection probability (which can be complex, and a function of time/energy), and $\theta(t_0, t_1)$ is the phase accumulated in the laser field from time t_0 to time t_1. The summation is over all all classical trajectories that lead to a final kinetic energy W. A similar term can be created to describe the portion of the

spectrum due to the direct electrons that do not rescatter. If the phase information is ignored (i.e. $\theta = 0$), the calculation is purely classical aside from the tunneling event, and $P_{scat}(W)$ then describes the envelope of the spectrum when θ is included.

2.2.3 The Coulomb-Volkov State

As we have truncated our expansion to just the first or second order, it is of course an incomplete description of the ionization process. This is especially true for low energy electrons that interact more with the system potential during ionization and subsequent acceleration. An example of this is near threshold emission from atomic systems [39]. A technique often employed in the calculation of $M_{\mathbf{p}}$ such that more information about the atomic potential is included, especially for low-energy electrons, is to replace the spatial component of the outgoing Gordon-Volkov state with that of the continuum eigenstate of the atom. This new "Coulomb-Volkov" wave is expressed as

$$\psi_{\mathbf{p}}^{CVl}(\mathbf{r}, t) = \psi^{C}_{\mathbf{p}+q\mathbf{A}(t)}(\mathbf{r})\, e^{-iS_{\mathbf{p}}(t)}, \tag{2.29}$$

where $\psi_{\mathbf{p}}^{CVl}$ is the Coulomb-Volkov wave in the length gauge, and $\psi_{\mathbf{p}}^{C}(\mathbf{r})$ is the spatial component of the atomic continuum eigenstate. This has the desired condition that in the limit of no electric field, it simply describes the atomic continuum eigenstate. However, if the coulomb field is turned off, it simply describes the Gordon-Volkov solution in the length gauge.

Others have shown substantial improvement in describing near threshold ionization and streaking by substituting $\psi_{\mathbf{p}}^{CVl}$ in place of the pure Gordon-Volkov solution when solving for SF driven processes, such as those used to calculate $M_{\mathbf{p}}$ above [36, 39, 40]. This approximation will be used extensively in Chapter 4 to improve the characterization of attosecond pulses in the low energy regime, where it is crucial to accurately account for the atomic phase shifts induced onto the electron wave packet when transitioning from the ground state to the continuum.

Chapter 3

Methods for Attosecond Pulse Characterization

Since the advent of HHG in the early 1990s, it was clear that sub-cycle pulses of EUV light were likely being generated. However, experimental techniques able to verify the temporal profile of the attosecond pulses were not available until the early 2000s. At this time, techniques were developed which were able to use a portion of the laser which generated the EUV pulses to provide a timing reference. In analogy with the streak camera approach for measuring electron bunches from photocathodes, the EUV pulses could ionize an atom to generate an electron packet in the presence of the long-wavelength pulse. Depending on the time at which the electron is then injected into the long-wavelength pulse, it will experience spectral broadening and/or a ponderomotive shift [41]. The spectral broadening is sensitive to the duration and chirp of the attosecond pusle, and can thus be used to measure it. Such a technique was used as the first verification of the sub-cycle nature of an isolated attosecond pulse generated with HHG [9].

For weaker streak fields, one can describe the change in spectrum by including the absorption of the EUV pulse and subsequent absorption/emission of a photon of the long-wavelength pulse. In this regime, a technique was developed for the characterization of attosecond pulse trains exhibiting odd harmonics entitled RABITT (reconstruction of attosecond beating by interference of two- photon transi-

tions) [2]. This set the stage for the next breakthrough in attosecond pulse retrieval: FROG-CRAB.

It was just over a decade ago that Mairesse and Quéré [21, 23] demonstrated how the physical process of emission by an attosecond EUV pulse and subsequent streaking by a long-wavelength pulse could be combined with frequency resolved optical gating (FROG), under certain constraints, to retrieve a general EUV pulse envelope. This technique is generally referred to as FROG-CRAB (frequency resolved optical gating for the complete retrieval of attosecond bursts). While RABITT and the attosecond streak camera could be used for the specific cases of pulse trains exhibiting odd harmonics and isolated pulses respectively, FROG-CRAB demonstrated that the amount of information contained within an electron streaking spectrogram was enough to simultaneously solve for both an arbitrary streaking waveform and attosecond pulse envelope. The method was far from perfect, being bandwidth limited and not allowing for the inclusion of the dipole transition matrix element describing the transition from the photon pulse to an electron wavepacket. Nonetheless, it paved the way for the future development of techniques able to reconstruct general EUV pulse forms.

In this chapter, the basics of attosecond pulse retrieval will be reviewed. This includes both theoretical and experimental approaches. In Section 3.1 the physics of attosecond pulse generation using HHG in gases is discussed. In Section 3.2, the physics of streaking and concepts such as the electron spectrogram are introduced. Section 3.3 then continues this discussion to give a basic review of reconstruction methods, with an emphasis on the FROG-CRAB approach. Finally, the chapter is concluded with Section 3.4 which discusses experimental approaches to building an attosecond streaking apparatus, including a detailed description of the streaking apparatus developed at MIT.

3.1 High Harmonic Generation in Gases

Before discussing the measurement of an attosecond pulse, it is necessary to spend some time discussing how such pulses are generated. While we discussed SF perturbation theory in the context of electron emission in Section 2.2, its relation to high haromonic generation is transparent. For instance, starting with the expression in Equation (2.18) but changing the upper integration bound in time to t, it would describe the amplitude of $|\psi_{\mathbf{p}}^{V_l}\rangle$ at time t of an electron packet where the ground state potential has been neglected after emission to time t. This amplitude can then be used to calculate an approximation of the emitted wave packet at time t by integrating over all outgoing momenta $\mathbf{p}$, and projecting it again onto the ground state to determine the recombination amplitude. For a more formal derivation of this procedure, see Lewenstein et al. [20]. By applying a saddle point approximation, one sees a similar physical description as used to describe electron emission and rescattering. An electron is emitted at some time τ with a probability amplitude given by the dipole transition matrix element. It then propagates in the field where it is accelerated, but does not interact with the atomic potential. Then at time t, the electron returns to the parent ion, and recombines with a probability described by the recombination amplitude, when it emits an outgoing photon.

Energy conservation demands that the emitted photon has the energy

$$\hbar\omega = \frac{(\mathbf{p} + \mathbf{A}(t))^2}{2m} + I_p, \tag{3.1}$$

where I_p is the ionization potential of the atom. It has been discussed in Section 2.2.2 how, at high field strengths when the Keldysh parameter $\gamma \ll 1$, the ionization is well described by quasistatic tunneling [30]. This means that the ionization is restricted to a narrow region of time near the peak of the electric field. Furthermore, the saddle point approximation tells us that the greatest contribution to the final recombination amplitude occurs for those electrons described by classical trajectories that return to the parent ion. By combining these observations, classical trajectories that return to and recombine with the parent ion are isolated

and weighted with their corresponding tunneling probability. This describes the emission of a chirped outgoing photon generated over a sub-cycle period of time after the ionization event. For long drive pulses, this happens at each half-cycle of the electric field, and, for a linear driving pulse, there is a π phase shift for each emitted pulse due to the inversion symmetry of the process. Thus, only odd harmonics are generated by longer drive pulses which are well described by a slowly varying envelope and monochromatic carrier wave.

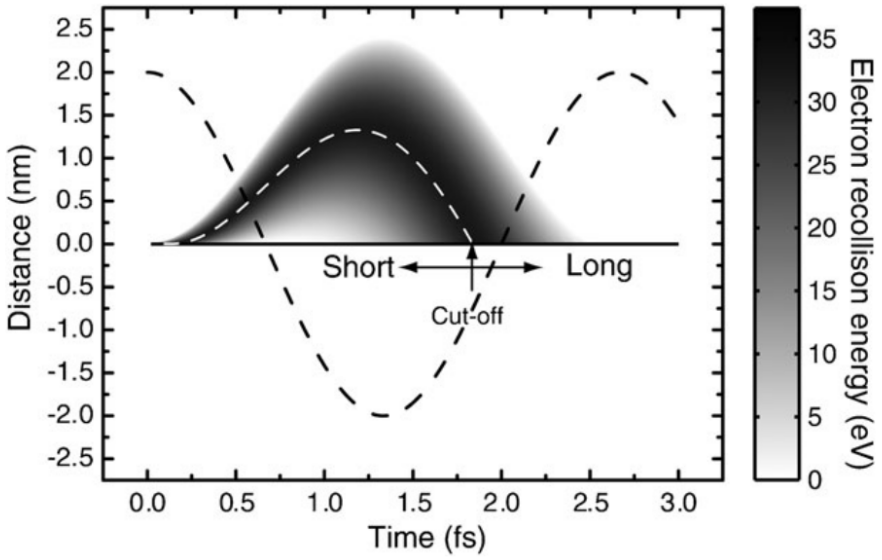

Figure 3-1: Demonstration of HHG trajectories that lead to recombination in the semi-classical description. Note that all of the trajectories originate over a very narrow window near the electric field peak. After laser acceleration, there is a spread of recombination times a little more than a half-cycle later over a sub-cycle window in time. The recombination energy is described by the shade of the trajectory. Note that for short trajectories, the energetic electrons (outgoing photons) recombine (are emitted) at later times, and the less energetic electrons (outgoing photons) recombine (are emitted) at later times. In reality, the short trajectories dominate in experimental observations as they have a much smaller divergence angle compared to the long trajectories. Image taken from [42].

The half-cycle anti-symmetry of the EUV pulses can be broken by the inclusion of a pulse centered at the second harmonic of the drive pulse. At low intensities, the second harmonic pulse changes the action phase accumulated during the electron excursion before recombination. More importantly, the change in phase is different for each consecutive half-cycle, breaking the strict π phase offset between adjacent harmonics. For a uniform pulse train (i.e. each half-cycle has the same

pulse envelope, only differeng by a phase offset), if this phase offset is reduced to $\pi/2$, odd and even harmonics are generated in equal strength. However, as the second harmonic field is increased significantly, and the delay chosen appropriately, every other half cycle of the fundamental pulse will be enhanced while the others are reduced in strength due to the difference in ionization probability. If the second harmonic is strong enough, pulses are only generated once per cycle.

Since electron recombination requires that the emitted electron return to the parent ion, the HHG emission probability is quite sensitive to the drive pulse's ellipticity. For instance, an ellipticity of just 20% is sufficient to reduce the HHG yield by up to an order of magnitude at typical driving field strengths in Ar [43]. Thus, it is possible to develop a pulse that has an ellipticity over a certain threshold, ξ, for the majority of its duration, and below this threshold over a brief window. This window is referred to as the gate width as it is the only region of the pulse where HHG has a high probability of being generated. If the gate window is sufficiently shorter than half of a cycle, $T_0/2$, it is possible to generate an isolated attosecond pulse. This can be combined with the addition of a strong second harmonic pulse to relax the maximum gate window to one cycle [44].

Polarization gating (PG) is typically implemented using a combination of custom and commercial waveplates in order to achieve the appropriate polarization profile for gating. In a PG setup's simplest form, a multi-order (MO) quarter-wave plate is used separate an input pulse into two linearly polarized pulses, one polarized along the ordinary axis, the other along the extraordinary axis, with a central region where the two overlap having a circular polarization. This is then sent through a zero order or achromatic quarter-wave plate at the correct orientation such that the outside linear portions of the waveform are transformed to a circular polarization, and the central portion is transformed back to a linear polarization. The dispersion of each wave plate must also be compensated to ensure the minimum pulse duration at the output.

Consider a simple polarization gating setup as shown in Figure 3-2. For a Gaussian drive pulse at 800 nm with a duration of 8 fs FWHM, a custom multi-order

quartz quarter wave plate 337 μm thick (3.75λ) is used to separate the input pulse into two orthoganally polarized pulses with a central region that is circularly polarized. Then, a zero-order quarter-wave plate (based off of design specifications from Thorlabs Inc.) is used to convert the circular portion to linear polarization, and the linear portions to circular polarization. Another zero-order or achromatic waveplate could then be used afterward for complete control of the outgoing polarization direction.

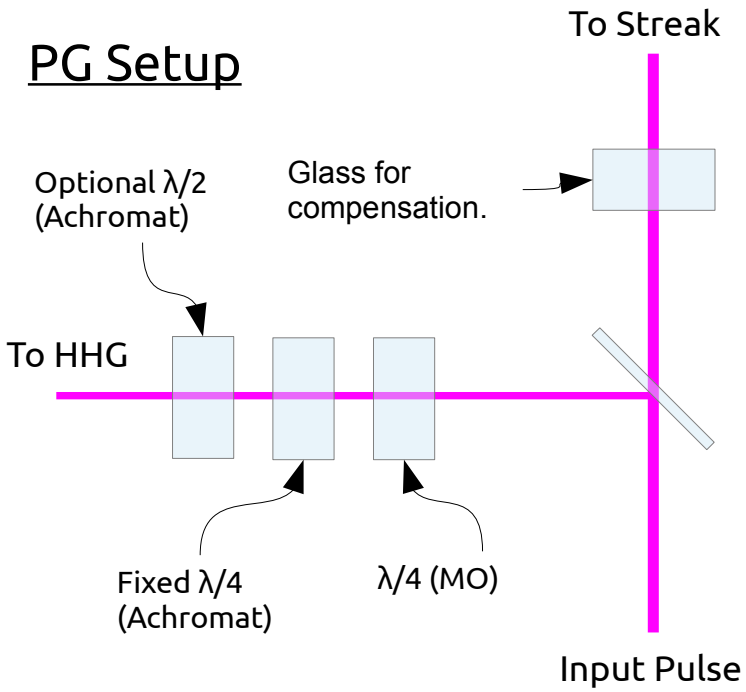

Figure 3-2: A simple PG setup. The second quarter-wave plate and final half-wave plate can be either achromatic or zeroth order depending on how short the input pulse is.

In the conventional configuration, for an input pulse that is linearly polarized along the x-axis, the first quarter-wave plate's fast axis is oriented at an angle of 45°, while the second quarter-wave plate is oriented at an angle of 90° (relative to the x-axis). This results in the ellipticity and field profile as shown in Figure 3-3.

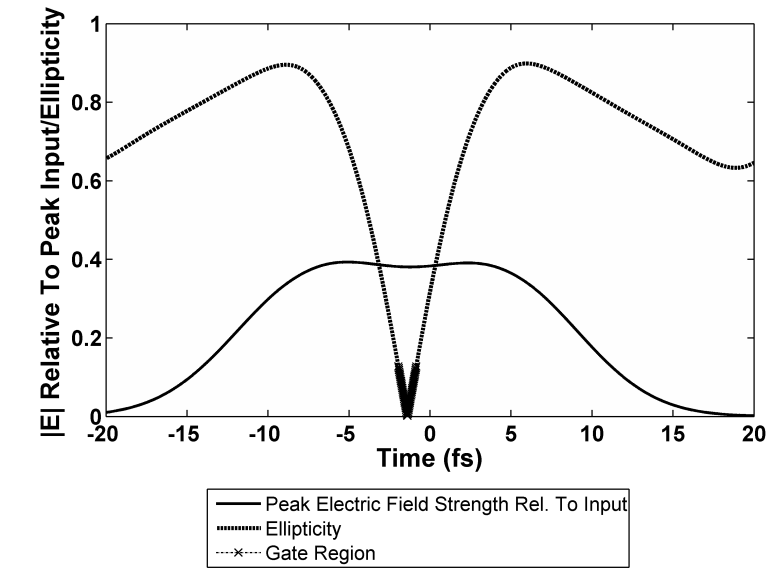

(a)

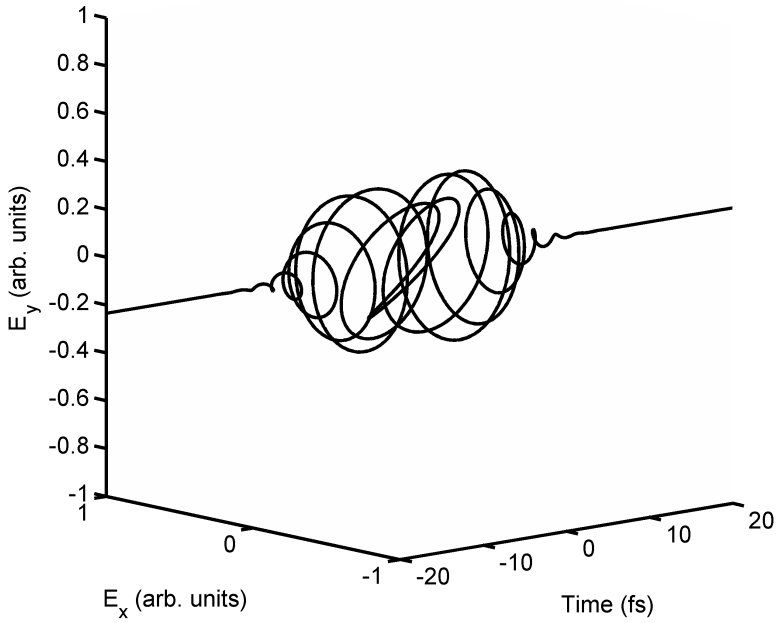

(b)

Figure 3-3: Output ellipticity (a) and field profile (b) of a conventional PG setup with input Gaussian pulse width of 8 fs. The dispersion of all the quartz wave plate elements has been compensated up to the second order. An ellipticity threshold of $\xi = .15$ is used leading to a gate window of 1.1 fs.

Alternate configurations may be desired, especially for longer input pulses. This is due to the fact that it is necessary to have a large separation between the two linearly polarized pulses from the initial MO wave plate in order to reduce the gate window. The drawback to this is that the linearly polarized region is preceeded by an intense circularly polarized pulse that creates an ionized plasma. This leads to two undesired scenarios: the plasma is dense enough to break the pulse up before the linear portion can produce HHG, or the ground state is completely depleted before the linear portion reaches the gas. Generalized double optical gating tackles this issue, allowing polarization gating techniques to be used for pulses up to 28 fs in duration. However, even the simple setup in Figure 3-2 can be tweaked to achieve a similar result. For instance, by detuning the first waveplate to 30° and the second to 80°, it is possible to reduce the field strength of the leading edge of the pulse allowing a more adiabatic increase in field strength, while maintaining an adequate gate window of just 1.14 fs. These results are shown in Figure 3-4.

3.2 Streaking

The techniques used to generate both isolated attosecond pulses and attosecond pulse trains discussed in Section 3.1 would be of no value if there were no way to validate them experimentally. As of the writing of this thesis, the only experimentally viable method of measuring an attosecond EUV pulse is via electron streaking. While various reconstruction methods exist, many of which will be discussed in the next section, the streaking process itself remains essentially the same. In fact, any pulse retrieval method requires the following fundamental elements.

1. A reference pulse
2. An interaction medium
3. A stable and accurate delay line
4. A detector

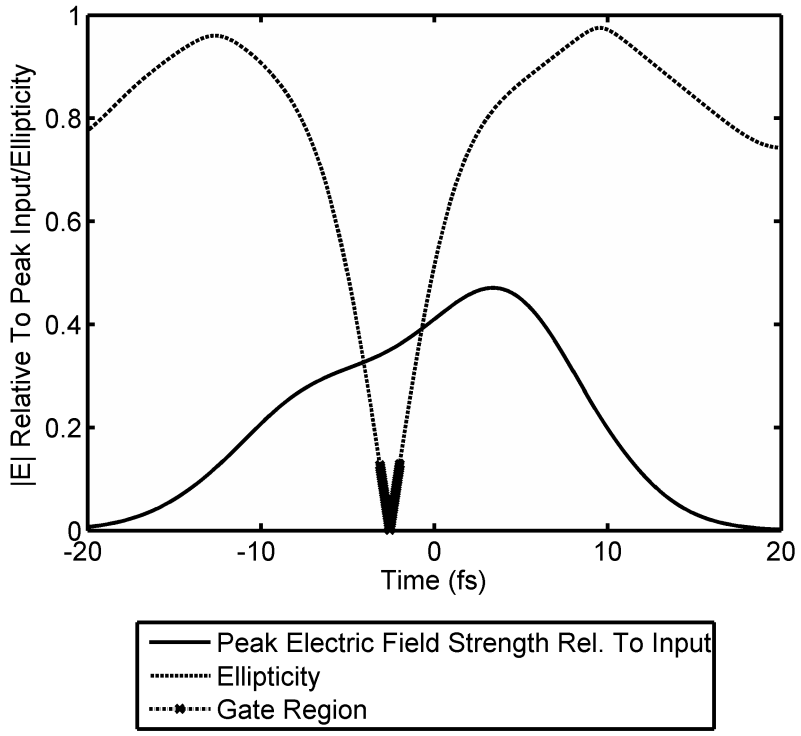

(a)

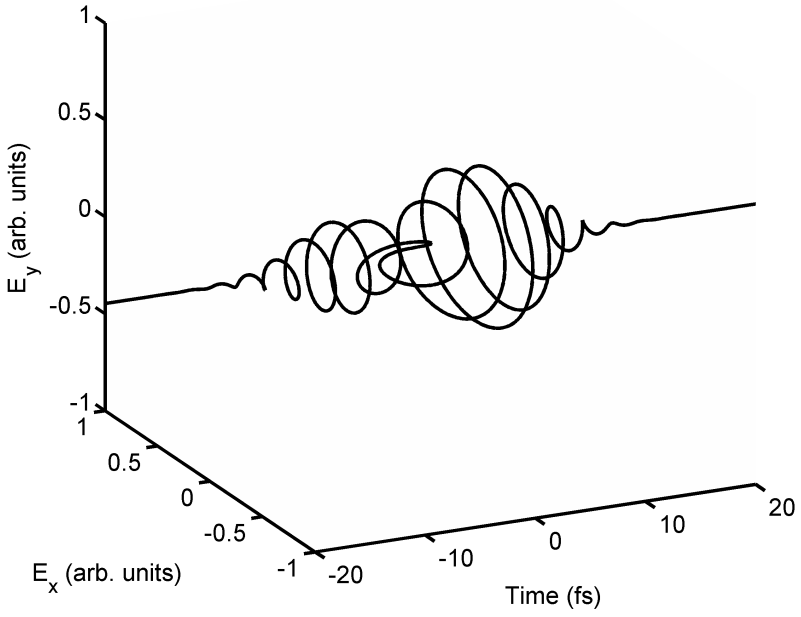

(b)

Figure 3-4: Output ellipticity (a) and field profile (b) of a detuned PG setup with input Gaussian pulse width of 8 fs. The dispersion of all the quartz wave plate elements has been compensated up to the second order. An ellipticity threshold of $\xi_* = .15$ is used leading to a gate window of 1.14 fs.

For instance, in the optical implementation of second harmonic generation (SHG) FROG, the reference pulse is a copy of the pulse to be measured, the interaction medium is a crystal where the second harmonic is produced, and the detector is a spectrometer which measures the second harmonic spectrum as a function of delay. It would be convenient to just use a nonlinear medium to implement an all optical FROG in the EUV domain, or even just an interferometric autocorrelator for that matter, but the absorption in crystals and low intensity of the EUV pulses prohibit the use of such techniques.

However, the EUV spectrum can be mapped onto an electron via single photon absorption and readily measured with an electron spectrometer. A copy of the long-wavelength drive pulse can then be used as a reference, and the interaction occurs between the electron and electric field of the long-wavelength laser. By recording electron spectra as a function of delay, adjacent energies in the electron spectra are coupled via the long-wavelength field, and their interference provides the necessary phase information to reconstruct the attosecond pulse. To see how this is achieved, it is helpful to first set up a model for the physical process.

The expression for the probability amplitude describing the transition of an electron from an initial state to a continuum Gordon-Volkov state was given in Equation (2.18). For the case of streaking, there are optical pulses which describe the electric field $F(t)$

$$F(t) = F_X(t-\tau) + F_L(t), \tag{3.2}$$

where $F_X(t)$ is the EUV pulse, and $F_L(t)$ is the long wavelength streaking pulse, and τ is the controllable delay. For the sake of simplicity, we are dropping vector notation here and assuming that we are working with all field polarizations and electron momenta in the z-axis. This is justified as later we will be detecting only those electrons that are emitted along the polarization of the streaking field. Also, from this point forward, atomic units will be used explicitly, thus factors such as q, m and $\hbar$ will be dropped from the equations for simplicity.

Upon substitution into Equation (2.18), two observations are apparent.

1. The ponderomotive energy of the EUV pulse is negligible in comparison with that of the IR pulse. Thus, it is not included in the calculation of $S_{\mathbf{p}}(t)$.

2. The two separate pulses lead to two separate integrals: the first describing ionization due to the EUV pulse, the second describing ionization due to the long wavelength pulse. Since the emission probability due to the long wavelength pulse is kept low (i.e. the field strength is kept well below the ionization threshold), the second integral is neglected.

This leads to the following expression describing EUV ionization and the subsequent streaking of the electron in the long wavelength laser field

$$M_k(\tau) = -i\int_{-\infty}^{\infty} dt d_{k+A(t)}\tilde{F}_X(t-\tau) \times \exp\left\{i\left(I_p t + k^2 t/2 - \int_t^{\infty} dt'\left[kA_L(t') + A_L^2(t')/2\right]\right)\right\}, \tag{3.3}$$

where I_p is the first ionization potential of the atom used for streaking, the tilde in $\tilde{F}_X(t)$ indicates the complex description of the EUV field is used (i.e. only momentum components in the direction of the detector matter). A spectrogram is then formed by measuring $|M_k(\tau)|^2$ for a range of delay values.

As long as the ionizing EUV field has sufficient energy, the emitted electron will escape the atom at a high enough velocity that, despite the force of the streaking field, it will never return to the atom. This justifies the inclusion of just the lowest order term from the SF perturbation theory expansion. If $F_L(t)$ is a long pulse, the outgoing state is well approximated using the generalized Bessel function expansion as in Equation (2.10). If only the $-1 \leqslant n \leqslant 1$ terms in the expansion are kept, the amplitude for a transition to any final momentum k at any delay τ has three contributions. Of course, higher order terms can also be included, but the calculation is restricted to three terms here for simplicity. The first is from a single photon absorption of the EUV to the final state. The second is from a single photon absorption of the EUV to a final state with energy $k^2/2 - \omega_L$, where ω_L is the angular frquency of the long wavelength field, followed by a single photon absorption

of ω_L. The third is from a single photon absorption of the EUV to a final state of energy $k^2/2 + \omega_L$ followed by a single photon emission of ω_L. Thus, the inclusion of the long wavelength pulse results in the interference of different portions of the electron energy spectrum leading to a reshaped output spectrum.

By shifting the delay and retaking the spectrum, the relative phases of each transition are shifted. By then noting how the spectrum has changed in intensity at each output energy value as a function of delay, one can determine the relative phase shift between each outgoing energy component of the electron spectrum. Since there is a direct correspondence between the electron energy spectrum phase and the input EUV spectrum phase, all information necessary to reconstruct the initual EUV pulse is present within the spectrogram.

3.3 Reconstruction Methods

The landscape of attosecond pulse retrieval techniques can be broken down into two basic appraoches: generalized projections algorithms (GPA, FROG-CRAB [22, 23]), and frequency domain interferometric methods (e.g.RABITT [2], PROOF [25], or iPROOF [24]). FROG-CRAB utilizes the fact that $P(k,\tau) = |M_k(\tau)|^2$ can, upon a few basic approximations, be recast as a FROG spectrogram

$$S(\omega,\tau) = \left| \int_{-\infty}^{\infty} dt \tilde{E}_P(t-\tau)\tilde{E}_G(t)e^{i\omega t} \right|^2, \tag{3.4}$$

where $\tilde{E}_P$ and $\tilde{E}_G$ are complex pulse and gate functions respectively. To do this requires that the non-separable functions of momentum and time be removed from the integral. This is achievable when the DTME is not dispersive with energy, and the bandwidth of the EUV pulse is narrow enough to approximate the $kA_L(t)$ term as $k_c A_L(t)$, where k_c is the central momentum. If both of these approximations are satisfied, it is relatively straightforward to use a standard FROG retrieval approach, such as PCGPA (Principle Components Generalized Projections Algorithm) [45], or a more customized approach, such as LSGPA (Least Squares Gen-

eralized Projections Algorithm) [22], which better accounts for specific issues with FROG-CRAB spectrograms (such as not requiring the spectrogram to be periodic in delay, and allowing a relaxed energy/time sampling constraint).

On the other hand, frequency domain interferometric techniques work directly from the principle described at the end of Section 3.2. After reducing the streak pulse intensity to the limit that each final energy component only has contributions from three transitions, changes in the spectrum at each energy level are monitored as a function of delay. The relative phase between each final energy component in the electron, and thus EUV, spectrum, is then calculated based on this analysis. For instance, RABITT utilizes the fact that typical attosecond pulse trains have no even harmonic contributions in the final spectrum. Thus, the even beat notes that arise in the spectrogram come from transitions to an odd harmonic, and then either a $\pm\omega_L$ transition to an adjacent even harmonic. This reduces the complexity of the problem, and gives a direct way to visualize the relative phases of the original odd harmonics. Figure 3-5 demonstrates the basics of this technique.

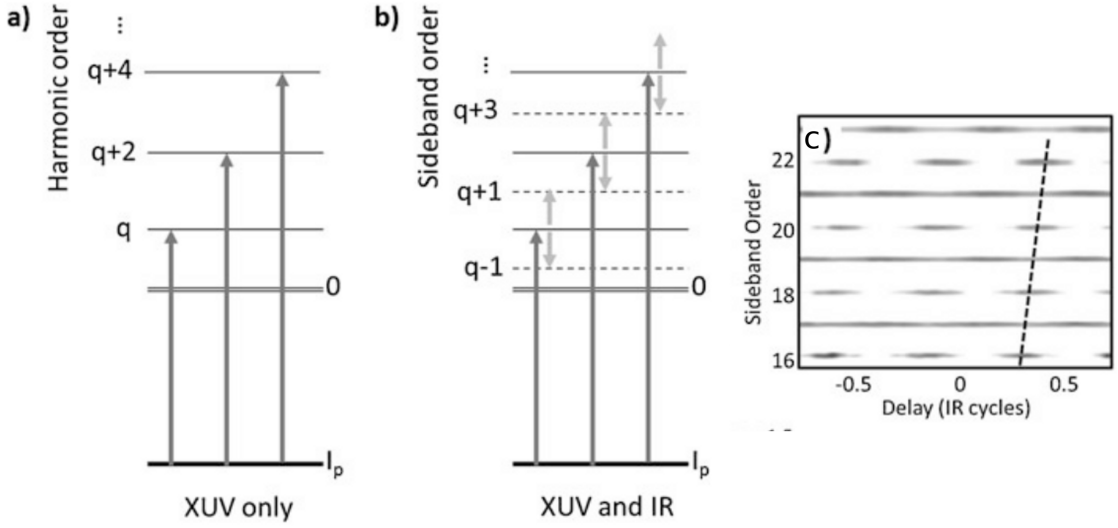

Figure 3-5: Demonstration of the RABITT technique. (a) The electron transitions without IR and (b) with IR present. In (c) an example spectrogram of odd harmonics is shown. Note the phase shift between the spectral peaks in each band as a function of harmonic order. This is used to determine the phase shift between adjacent harmonics. Adapted from [46].

The intensity of the n^{th} even sideband in Figure 3-5c is simply described by a cosine in τ of the form

$$A_f = 2\cos(2\omega_L\tau + \phi_{n-1} + \phi_{n+1} + \Delta\phi^f_{atomic}), \tag{3.5}$$

where ϕ_n is the phase of the n^{th} EUV harmonic, and $\Delta\phi^f_{atomic}$ is the phase due to the transition in the presence of the atomic potential, and is well known from prior measurements. This provides a relatively straightforward procedure for determining all ϕ_n in the original EUV spectrum.

The PROOF method [25] extends the RABITT technique for use with continuous spectra by including all three possible transitions contributing to each final energy level. As a modification to PROOF, the iPROOF [24] method completes a full generalization of the RABITT technique for an arbitrary spectrum (i.e. continuum or pulse train) by also incorporating physics of the photionization process. The benefit of frequency domain interferometric techniques is that they offer a very direct means of fitting the relative phase of the EUV spectrum without the need of a blind minimization algorithm to compute both the long-wavelength and EUV pulses. However, they limit the types of long-wavelength pulses that can be used.

To ensure a single ω_L transition after EUV absorption, the long-wavelength pulse must be weak and have a well defined photon energy. This is prohibitive if one wishes to simultaneously characterize a broadband, complex waveform along with the EUV pulse (for example [47, 48]). For this reason, an extended FROG-CRAB algorithm, entitled the VTGPA ("Volkov" Transform Generalized Projections Algorithm) was developed by the author and is discussed in detail in Chapter 4. The VTGPA seeks to maintain the general nature of FROG-CRAB, such as allowing more intense and complex streaking fields, while alleviating drawbacks, such as the central momentum approximation and inclusion of the DTME.

3.4 Experimental Methods

This section focuses on experimental techniques used for characterizing attosecond pulses, with an emphasis on the experimental apparatus built in the Ultrafast Optics and X-Rays Group at MIT. Section 3.4.1 gives a broad overview of the apparatus layout in the laboratory. Section 3.4.2 discusses the design of a custom delay locking and control system. Section 3.4.3 then discusses key aspects of a time of flight electron spectrometer for attosecond pulse characterization.

3.4.1 Overall Apparatus Layout

As discussed earlier in the text, the typical EUV energies produced from HHG are readily absorbed in air, necessitating that from the generation point forward, the optical path is housed inside of a vacuum chamber unit. While the streak arm does not need to be routed through the vacuum, housing both paths inside of the vacuum apparatus reduces pointing and delay fluctuations due to air currents and acoustic sources. As stability was of prime concern for accurate pulse retrieval, the entirety of the delay line is housed in vacuum in the MIT apparatus, shown in Figure 3-6.

The input window is a 3 mm thick CaF_2 window which ensures minimal dispersion and broadband transmission for the incoming drive pulse. After this point, the drive pulse is split using a partially transmissive Au mirror. A partially transmissive metalic film is advantageous as very broad spectral ranges can be achieved. For instance, a 30 nm thick gold film on fused silica has a relatively flat reflectivity and transmission from 800 nm to beyond 2 μm, which is ideal for the range of sources typically used for generating HHG. The dispersion is also minimal, and confirmed to be dominated by the substrate used. This can be compensated for in the drive arm if a sufficiently short pulse is used.

From this point on, only Ag mirrors are used to minimmize dispersion and maintain flexibility in choosing the drive source wavelength. A curved Ag mirror is used to focus the drive pulse into a gas cell. The gas cell is simply a hollow

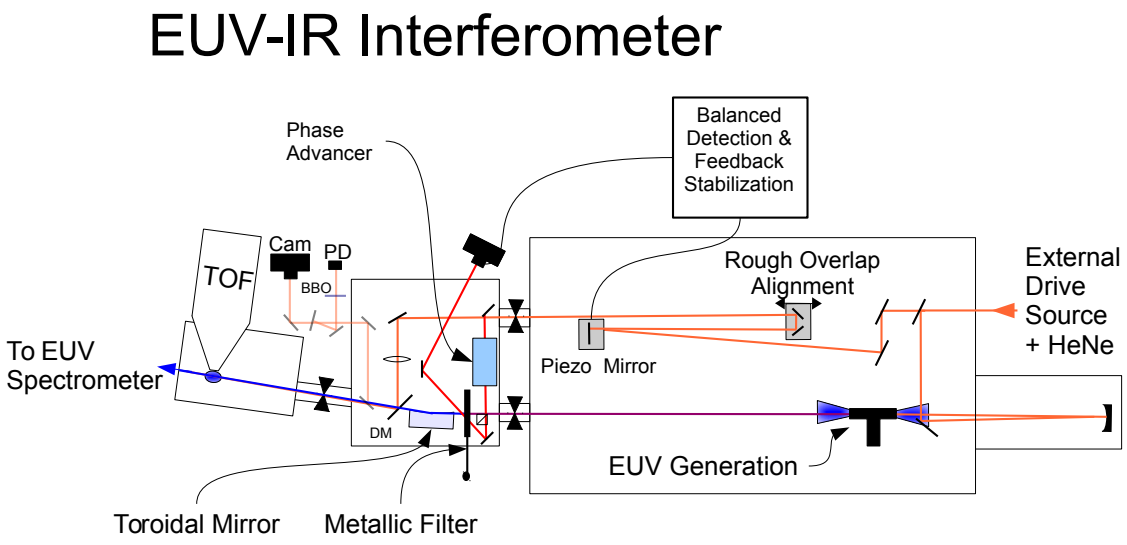

Figure 3-6: Schematic of the streaking apparatus at MIT. DM - drilled mirror, PD - photodiode, Cam - camera.

capillary filled with a fixed pressure of a particular gas species. In order to allow the HHG to escape from the glass, the capillary is drilled by the drive beam itself by turning up the intensity beyond its damage threshold. It was found that the choice of glass is key, as the damage threshold should be higher than the intensity used to generate harmonics so that the hole is not enlarged during EUV generation, but less than the peak intensity available from the laser. Alternatively, the glass capillary could be replaced by different geometries for improved HHG conversion efficiency or increased gas pressure.

From this point, the EUV pulses co-propagate through the chamber with the drive pulse, until it reaches an assembly for holding suspended metallic filters. These filters are made from suspended thin films of various metals, such as Sn, Al or Zr, that absorb/reflect the drive pulse while transmitting the EUV pulse. To pre-

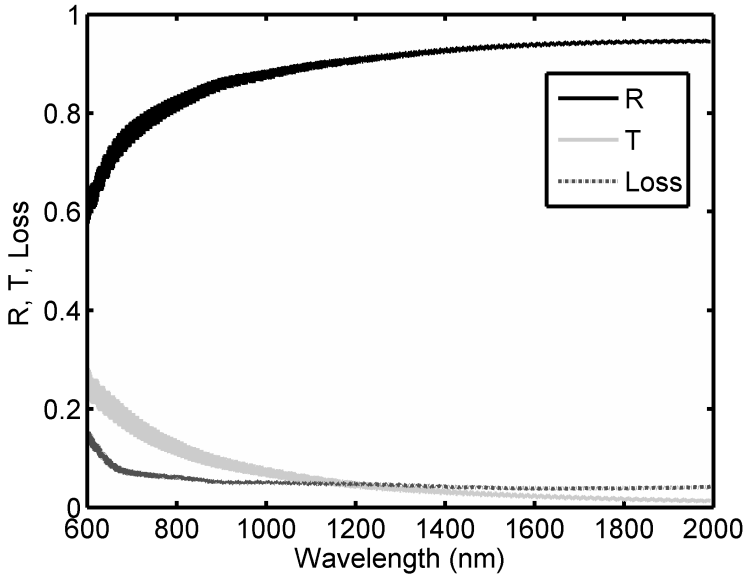

Figure 3-7: Power reflected (R), transmitted (T) and lost from a 30 nm thick film of Au on a 1 mm fused silica substrate at 45°. The reflection and transmission are quite flat from 800 nm to beyond 2 μm.

vent a complete absorption of the HHG, they are just hundreds of nm thick. However, for most films, the minimum practical thickness is on the order of 100 nm to prevent thermal damage and tearing. By careful selection of filter thickness and type, the EUV spectrum can also be reshaped.

To focus the EUV, a Au coated toroidal mirror (TM) is used. Since the EUV absorption from bulk Au is quite high at low angles of incidence, the Au surface must be used at a grazing angle. This requires that a curved mirror have two radii of curvature to prevent astigmatism. For instance, in the saggital plane $f = R_S/(2\cos(\theta))$, and in the tangential plane $f = R_T\cos(\theta)/2$ where f is the focal length of the optic, θ the incident angle, and R_S and R_T the saggital and tangential radii of curvature respectively. This adds complication to the alignment as there is only one angle at which the two planes come to a focus at the same focal length. To enable all degrees of freedom for alignment, the TM stage has the possibility to translate in z, tip, and tilt. A goniometer is used to adjust the pitch. The radii of curvature were chosen such that the focus in the HHG gas cell is imaged to the location just in front of the electron spectrometer interaction region with an

incident angle of 84° on the TM.

For alignment purposes, a pick-off mirror is used to divert the beam to a location outside of the chamber (translucent optics/beams in Figure 3-6) where a camera is positioned the same distance from the electron spectrometer focus. The optimal beam profile achieved is shown in Figure 3-8. The beam has side-lobes in the x direction as it is clipped on the TM. This, however, is not an issue for the HHG as the drive beam was measured to be roughly 3 times larger than the HHG beam at the entrance of the TM (~ 1 cm vs. ~ 3 mm). When using an aperture to reduce the size of the 800 nm beam such that it fits withing the clear aperture of the TM, it was confirmed that the side lobes disappear and the beam is well approximated by a Gaussian profile at focus.

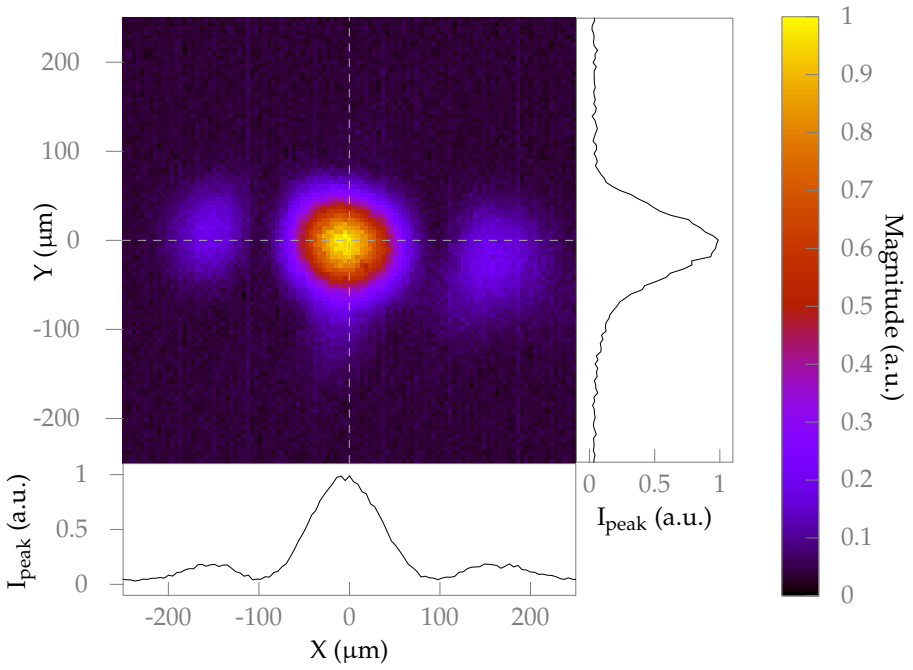

Figure 3-8: Image of the drive beam (800 nm) at focus (without the DM in place). The FWHM is roughly 90 μm in x and 83 μm in y.

For the streak path, a delay stage housing a gold coated corner cube retroreflector is used for coarse delay control, while a piezo with a maximum displacement of 40 μm is used for fine delay control. The outside portion of the beam which reflects off of the DM is then focused onto the interaction region of the electron spectrometer using a CaF_2 lens. This is aligned to the same spot as the drive beam using

the same camera. A typical streak beam focus at 800 nm is shown in Figure 3-9. Since only the annular portion of the beam is focused, it produces a mixture of a Gaussian and Bessel beam. If the streaking beam is clipped before the DM, higher order rings from the Bessel function start to appear as the Gaussian envelope expands. However, the central lobe stays relatively fixed in width as it is dominated by width of the main Bessel lobe, which is in turn dictated by the DM hole size.

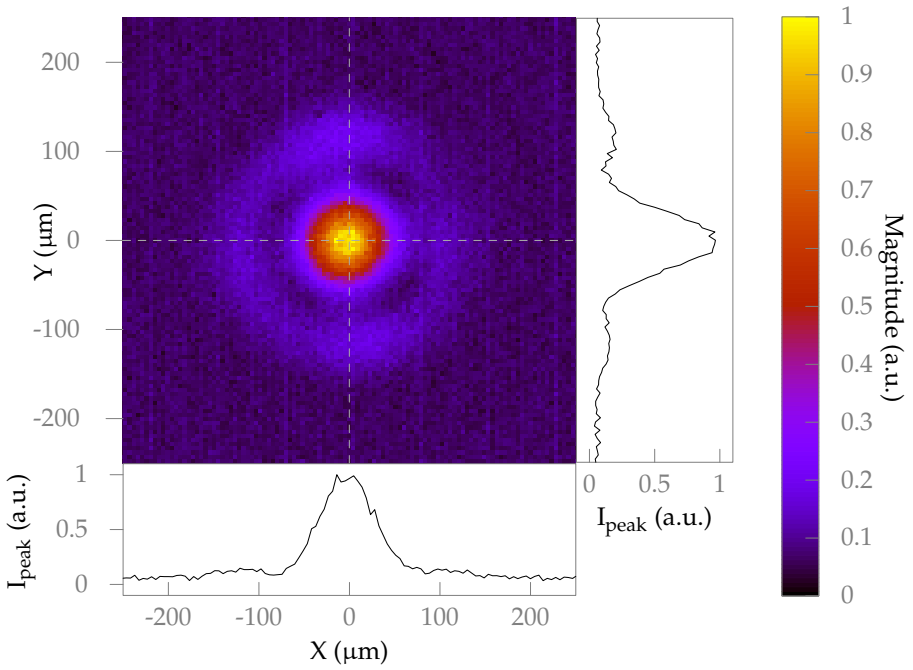

Figure 3-9: Image of the streak beam (800 nm) at focus (reflected from the DM). The FWHM is roughly 75 μm in x and y.

To assist in finding the temporal overlap between the streak and EUV beam, part of the alignment beam is diverted to a beta barium borate (BBO) crystal, followed by a photodiode with a bandpass filter that passes only the second harmonic of the drive pulse. By pulling the EUV filter assembly out, the drive beam and streak beam are both allowed to pass through the BBO, and a spike in second harmonic efficiency is observed when they are temporally overlapped. From there, the delay can be finely tuned by watching the two beams linearly interfere on the camera. This is also helpful for checking that the two beams are collinear, as the interference fringes appear to move left, right up or down if there were any difference in angle between the two beams.

3.4.2 Delay Locking and Control

Typical measurement times for compiling a spectrogram are between 10 min to 1 hour. Also, a typical delay step size used is on the order of 1/10 of the long-wavelength cycle. To minimize drift and improve the delay precision of the system, a custom "optical screw" was developed.

The idea behind such a system was inspired by the work of Wehner et al. [49], where they utilized the fact that, for equal intensity orthogonally polarized continuous wave (CW) beams with a variable delay, a quarter waveplate positioned at 45° will convert the output to linear polarization, with the angle of polarization dependent on the relative delay between the two arms. Thus, by setting a desired output polarization angle, you are in essence setting the delay. Furthermore, if that polarization angle is continuously rotated, the delay moves continuously in one direction, making, in essence, an optical screw.

While beautiful in its conception, there are some practical issues with this simple design. First of all, the intensity of each arm has to be identical. If this is not satisfied, the output is no longer linearly polarized, and this hurts the temporal resolution of the device. Secondly, it does not incorporate any form of balanced detection in the original scheme, making the delay sensitive to intensity fluctuations of the CW laser source.

To fix both of these issues, the entire design of the system reconfigured as shown in Figure 3-10. The major design change is the phase advancer element which is comprised of two quarter-wave plates at $\pm 45^\circ$ sandwiching a half-wave plate which can be arbitrarily rotated to angle θ. The Jones matrix of this system is found to be

$$J(\theta) = \begin{pmatrix} 0 & e^{-j2\theta} \\ e^{j2\theta} & 0 \end{pmatrix}. \tag{3.6}$$

Thus, for an x-polarized linear input beam, the output is y-polarized with a positive delay shift of 2θ.

After the phase advancer, the two paths are recombined with a polarizing beam splitter. This is important as it removes any components at an undesired polariza-

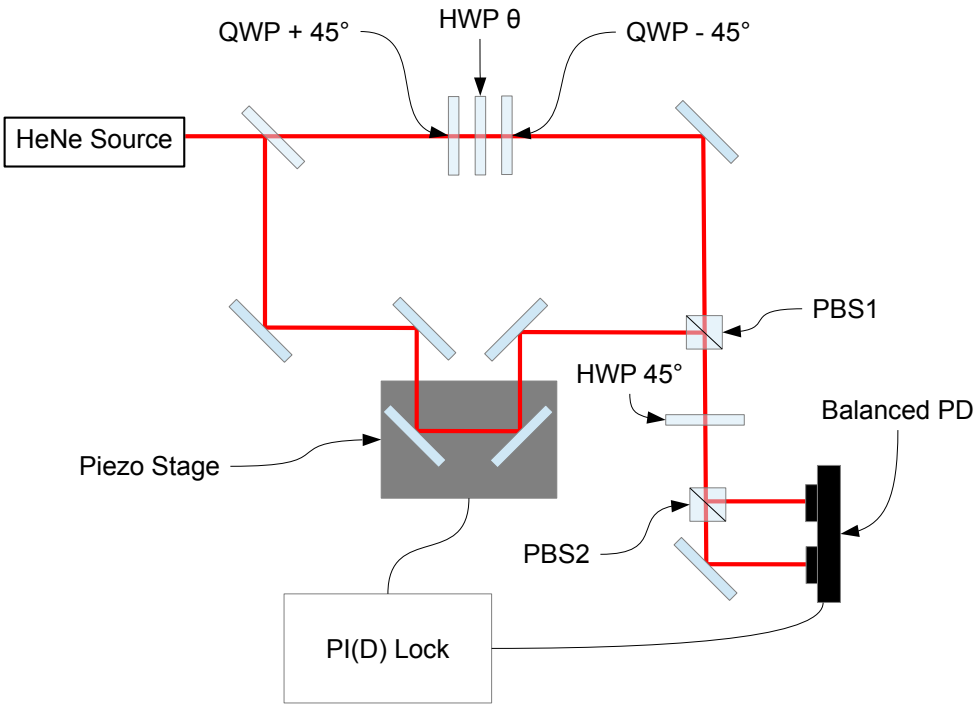

Figure 3-10: Schematic of the improved optical screw design.

tion from both arms, and ensures that they are both orthogonal at the output. From there, the two beams are rotated by 45° and split into two arms using a polarizing beam splitter. These two arms are then input to a set of balanced photodiodes, referred to as PD1 and PD2 respectively.

Given that the CW beam that travels through the top path has a field amplitude F_T, and that going through the bottom path amplitude F_B, the signal in PD1 and PD2, V_1 and V_2, can be written as

$$V_1 = G\left(\frac{F_T^2}{2} + \frac{F_B^2}{2} + F_T F_B \cos(\delta)\right) \tag{3.7}$$

$$V_2 = G\left(\frac{F_T^2}{2} + \frac{F_B^2}{2} - F_T F_B \cos(\delta)\right), \tag{3.8}$$

where G is a constant factor, and $\delta = 2\pi\Delta L/\lambda_{CW} + 2\theta$ is the combined phase of the

delay and phase advancer, with λ_{CW} the wavelength of the CW beam. Thus, the output of the subtraction of the two diode signals, which is used for feedback, is given as

$$V_{diff} = 2GF_T F_B \cos(\delta). \tag{3.9}$$

If a proportional-integral-differential (PID) feedback system is used to lock V_{diff} to zero, the delay line is stabilized. The delay jitter is insensitive to fluctuations in the CW beam intensity as the zero crossing only depends on the cosine term. For high resolution control of the beam delay, the user can set the half-wave plate to a new θ value. As the half-wave plate is rotated, the piezo is dragged with it to cancel out any induced phase difference between the two arms. If the wave-plate is continuously rotated, this phase accumulates and drags the piezo in one direction, limited only by the range of the piezo stack. Thus, the CW wave is used as a ruler, preventing errors in delay due to hysteresis or a mis-calibrated piezo.

The system is also flexible as the output signal has the same cosine dependence on delay no matter how different the intensity is in each arm. Even if polarization altering optics, such as the polarization gating setup shown in Figure 3-2, are placed into the drive path (i.e. the path not containing the phase advancer) the system still works as the polarizing beam splitter only selects the "correct" polarization when recombining the two arms.

Since the piezo has to control a relatively large mirror to support a $\sim$ 1 cm FWHM streaking beam, the upper limit of the feedback frequency is just a few tens of Hz due to the lowered resonance frequency of the piezo mount. Therefore, the locking system is primarily to prevent low-frequency drift, while good engineering practice was used to reduce jitter on the order of the repetition frequency of the laser. All of the rough vacuum pumps were fitted with vibration isolating supports, and the vacuum lines were routed through a heavy concrete block to dampen any residual vibrational noise. For the large turbo pump on the main HHG chamber, a flexible bellows with a rubber sheath was used to dampen any high frequency noise from its magnetic bearing.

As expected, the HeNe signal from the balanced PD exhibited the same noise floor when locked and unlocked, indicating that the residual high-frequency noise is out of the range of the feedback system. A measurement of this noise indicates that the fast mechanical vibrations were limited to less than 65 as RMS for day to day operation.

To characterize the long term drift of the entire system, an out of loop measurement was performed with the optical screw both locked and unlocked. The out of loop signal was provided by the second harmonic generation from the BBO crystal, which is periodic with one cycle of the drive beam, which was 800 nm in this measurement. The results of the delay drift for each case are shown in Figure 3-11.

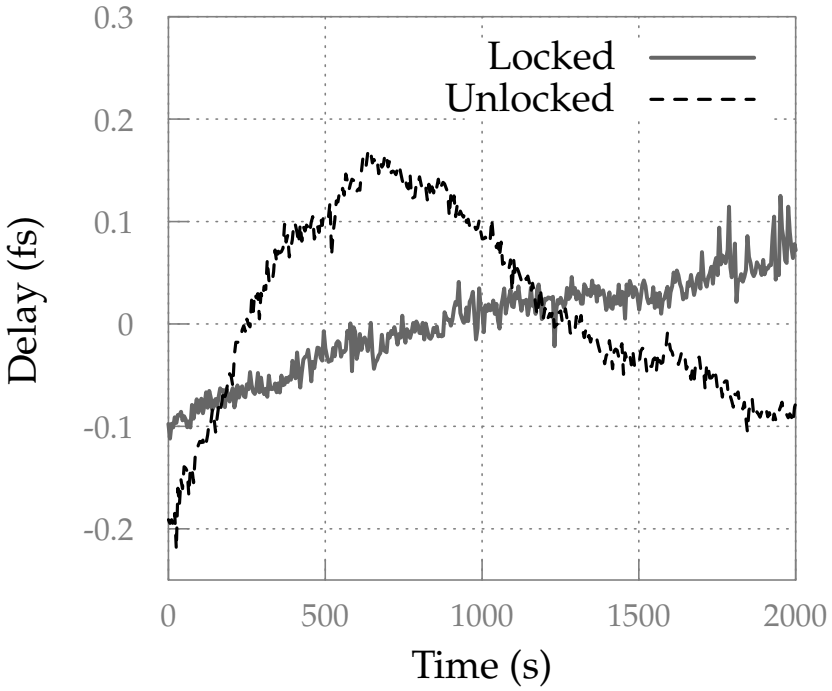

Figure 3-11: Out of loop drift of the system over a period of roughly 30 min.

Due to the well engineered, in-vacuum design, even the unlocked performance is quite stable, having a peak to peak drift of just 350 as. However, if monitoring this signal for several hours, it was observed that peaks such as that observed for the unlocked signal in Figure 3-11 occur at roughly a 30 min period. This was then correlated to the heating and cooling system in the laboratory indicating a

temperature dependent oscillation. When locking the optical screw these spikes were completely removed, leaving only a very slow drift, likely from the remaining unlocked section of the delay line. In the future, if better performance is desired, the HeNe path could be extended to cover this unlocked portion. However, this would require further engineering to allow the HeNe to circumvent the metallic filter assembly and toroidal mirror, and places strict alignment constraints on the CW interferometer relative to the main delay line. Thus, the best compromise would be to extend the current arrangement such that more path is covered, and the remaining path difference as similar as possible.

One final issue that can arise when using the optical screw is due to misalignment of any of the polarization optics. Due to the rotational symmetry of the half-wave plate in the phase advancer, any error has to be periodic with a $\theta = \theta_0 + 2\pi$ rotation. Typically, the only residual error remaining is well described by the inclusion of a first order sinusoidal correction. For instance, the time delay induced by a rotation of the half-wave plate should be linear with respect to θ, but if there is a non-negligible misalignment, it is better described by

$$\Delta t_{delay} = \frac{\theta T_{CW}}{\pi} + B\cos(\theta + \beta), \tag{3.10}$$

where Δt_{delay} is the time delay induced by the waveplate rotation after locking, and T_{CW} is the duration of one period of the HeNe source.

Again, the SHG signal from the drive and streak beam can be used as a reference standard. By measuring the interference signal as function of θ and plotting the result in the frequency domain, distinct side lobes appear at the modulation frequency $1/(2\pi)$. Thus, B and β can be calibrated by determining the appropriate values to remove the side lobes (see Figure 3-12).

3.4.3 Time of Flight Electron Spectroscopy

There exist many techniques for measuring the photoemitted electron spectrum for performing an attosecond streaking measurement, the most commonly used being

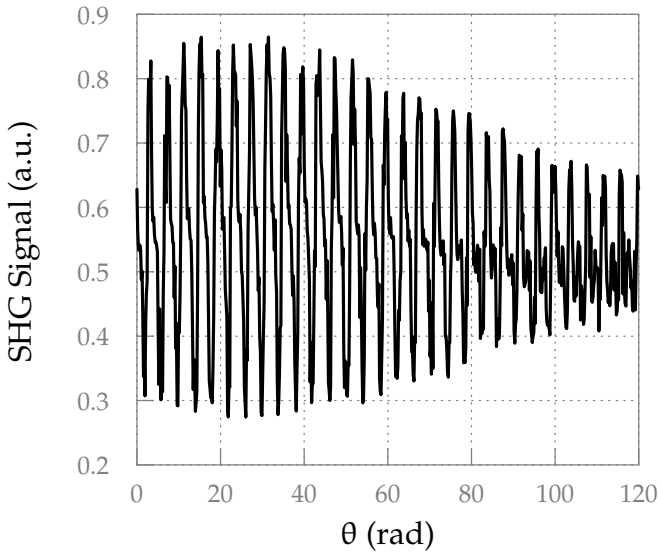

(a)

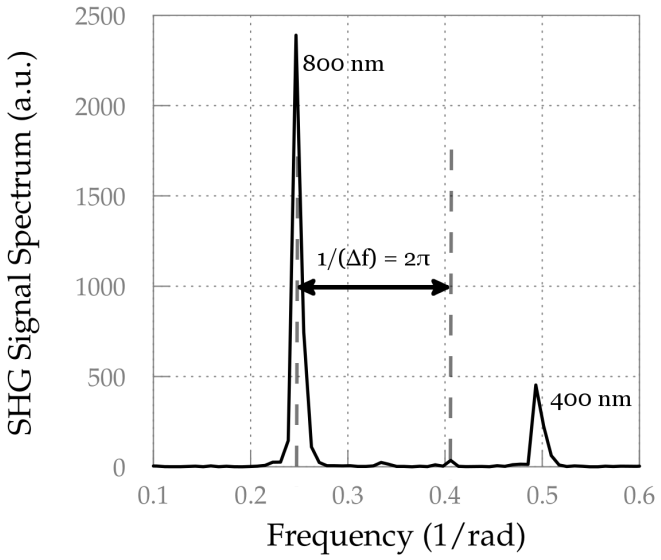

(b)

Figure 3-12: Signal used for calibrating the optical screw. (a) The direct SHG signal as a function of the waveplate angle θ (relative to some constant offset). (b) The frequency response of this signal. There are clear harmonics related to the fundamental interference at 800 nm and its second harmonic at 400 nm. The small sidelobes are at a frequency related to the waveplate rotation of $\theta = 2\pi$. These can be removed by fitting B and β in Equation (3.10).

velocity map imaging (VMI), and time of flight (TOF) electron spectroscopy. While the VMI is used in such a way as to give information of both the initial kinetic energy and the angular distribution of emitted electrons, attosecond reconstruction

methods typically only use those electrons emitted along the axis of the EUV polarization. Thus, a TOF electron spectrometer with a reduced acceptance angle can be used for improved energy resolution.

The basic principles behind TOF spectroscopy are simple. An electron is emitted at time $t_0 + \delta$ relative to an incident ionizing pulse. It then travels through a tube, which is often magnetically shielded to reduce interference from external magnetic fields, where it freely travels to a detector and creates an electronic impulse at some arrival time t_f. If this travel is purely kinetic (i.e. there are no external electromagnetic fields) then the initial velocity along the direction of the detector is given simply as

$$v = \frac{D}{t_f - (t_0 + \delta)}, \tag{3.11}$$

where D is the distance from the ionization region to the detector. If the incident pulse duration is much shorter than the mean time of flight $t_f - t_0$, then δ can be ignored, and we have the following expression for the initial kinetic energy of the electron

$$W = \frac{1}{2} m v^2 = \frac{m D^2}{2(t_f - t_0)^2}. \tag{3.12}$$

In practice, the exact time of flight to energy relationship is more complicated than this, as the effects of magnetic fields can never be completely neglected (especially for low kinetic energies), and electrostatic lenses and acceleration stages needed for electron detection affect the total flight time for a given input energy. However, despite these effects, the time-energy curve can be well approximated with a polynomial fit between $1/W$ and the time of flight. Thus, one can easily calibrate the time-energy relationship using an array of spectral peaks with known energy separation (or, ideally, known absolute energy). For the case of high harmonic generation, such a comb is easily formed by using a relatively long drive pulse (in our case 35 fs) to create well defined odd harmonics of the driver frequency. The raw time of flight spectrum and calibrated energy spectrum are shown in Figure 3-13. Note, in calibrating the spectrum, care has been taken to ensure the proper normalization such that the total amount of collected charge is conserved

between the time of flight and energy form, i.e.

$$Q = \int_0^\infty P(W)dW = \int_0^\infty I(t)dt, \tag{3.13}$$

which implies

$$P(W) = -I(t(W))\frac{dt(W)}{dW}. \tag{3.14}$$

In the above expressions, Q is the total collected charge in one spectrum, P is the spectrum intensity, $I(t)$ is the detector current at time of flight t, and $t(W)$ expresses the functional relationship between time of flight and energy.

The next calibration issue concerns the amplitude of the measured electron spectrum. A reference optical spectrum and the photoionization cross section can be used to account for the TOF spectrometer transfer function. To show this, imagine an ionizing EUV field polarized along the TOF axis with the streaking field turned off. The probability of a single-photon absorption as a function of momentum is then expressed by

$$|M_{\mathbf{p}}|^2 = |\hat{F}_X(p^2/2 + I_p)|^2|d_{\mathbf{p}}|^2, \tag{3.15}$$

where the hat notation represents the Fourier transform of a function. We then assume that the time of flight spectrometer is sampling over a small enough solid angle such that it can be approximated by the diffential cross section, $\frac{dJ}{d\Omega}$, in the direction of the TOF spectrometer

$$\frac{dJ}{d\Omega} = p^2|\hat{F}_X(p^2/2 + I_p)|^2|d_{\mathbf{p}}|^2. \tag{3.16}$$

This is of course still momentum normalized, however the spectrum we have calibrated thus far, $P(W)$, is in the energy domain. To switch normalizations requires a change of variable, and thus adds a factor of $\sqrt{2W}$ to the expression, yielding the energy normalized differential cross section

$$\frac{dJ}{d\Omega} = |\hat{F}_X(W + I_p)|^2|d_{\mathbf{p}(\mathbf{W})}|^2\sqrt{2W}. \tag{3.17}$$

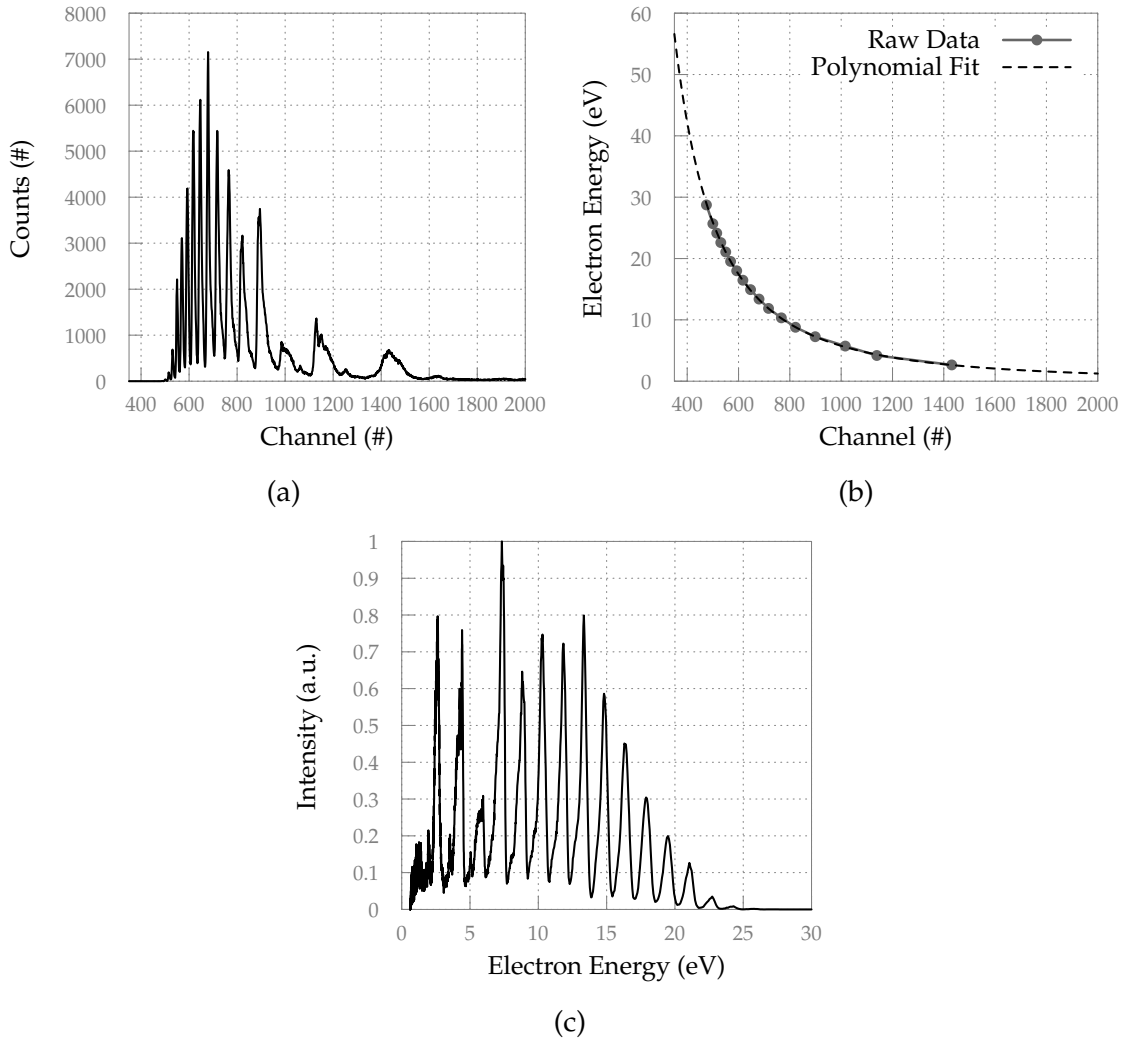

Figure 3-13: (a) The raw TOF spectrum plotting number of counts in each channel of the discriminator card. The second harmonic was superimposed onto the fundamental achieving both odd and even harmonics. The channel width was 250 ps. (b) The channel position of each peak plotted against its corresponding electron energy (calculated by using the harmonic number times the fundamental photon energy and subtracting the ionization potential of Ar, 15.7596 eV. The dashed line is obtained by finding a second-order polynomial fit to $1/W$, which provides the calibration curve. (c) The converted electron energy spectrum. Note how the harmonics are now evenly spaced and have similar bandwidth as one would expect.

This is the emitted spectrum that, for the case of an ideal spectrometer, would be directly measured to within a constant multiplicative factor. However, in any realistic scenario we must account for the possibility of an energy dependent collection

efficiency, $T(W)$, thus making the measured spectrum

$$P(W) \propto \frac{dJ}{d\Omega} T(W). \tag{3.18}$$

There is of course a constant multiplicative factor, depending on the density of atoms in the interaction region and solid angle of collection, that we are dropping as only the spectral shape is important for all of the applications discussed. We can easily calibrate $T(W)$ using the EUV optical spectrometer to measure $|\hat{F}_X(W + I_p)|^2$, and taking a calculated, or experimentally measured, DTME magnitude. One has to be careful to ensure that the cross section is not already in the differential form, otherwise the factor of p^2 will be twice accounted for. Figure 3-14 plots a measurement of $T(W)$ for the TOF spectrometer installed in the apparatus at MIT. The lens voltage settings were optimized to center the acceptance bandwidth of the spectrometer around the peak of the electron spectrum. The DTME used was calculated according to the method discussed in [37].

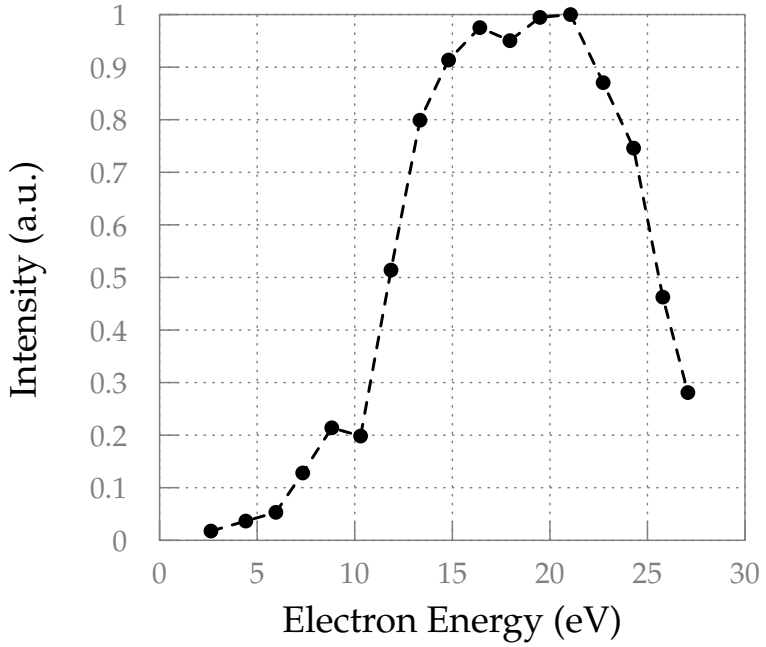

Figure 3-14: Measured TOF transfer function, $T(W)$, for spectrum shown in Figure 3-13. The measured points correspond to the harmonic peaks.

To this point, all aspects of creating a stable attosecond metrology setup have

been covered: HHG generation, creating a stable EUV/IR interferometer and electron spectroscopy methods with an emphasis on TOF spectroscopy. Experimental results will be shown in Chapter 4 after the VTGPA is introduced.

Chapter 4

The "Volkov-Transform" Generalized Projections Algorithm

4.1 Why Another Algorithm

The future of attosecond science depends on improvements in the control and characterization of the attosecond pulse itself. Many experiments have explored how attosecond pulses can be use to seed or probe electron dynamics on the attosecond time scale [50–53]. To gain more understanding in the analysis of such experiments, it is of vital importance to continue in the development of both flexible and accurate techniques for characterizing the attosecond pulse itself, the backbone of all such measurements.

As stated in Section 3.3, the FROG-CRAB technique, while able to fit both a complex streaking pulse along with an attosecond EUV pulse, has the limitation that the central momentum approximation must be satisfied. The root cause of the central momentum approximation in the FROG-CRAB technique is its reliance on the use of Fourier transforms. This Chapter introduces a generalized projections algorithm based on a least-squares minimization approach can be used in such a way that there is no use of Fourier transforms in the retrieval process. This allows one to fit the full form of the SFA without the need for the central momentum

approximation, and provides a straightforward way to incorporate the dipole transition matrix element into the fitting procedure. Furthermore, it does not require that the data be interpolated in the energy domain in order to satisfy constraints of a fast Fourier transform (FFT).

Unlike PROOF and iPROOF, this approach does not assume that the photon energy of the IR streaking pulse is well defined, nor that the field strength is sufficiently weak such that two-photon absorption of IR does not occur, making it suitable for simultaneously retrieving both the broadband attosecond pulse along with complex IR waveforms. An in situ characterization of both pulses proves advantageous when analyzing experiments that depend equally on both pulse forms, such as in [53–55]. Furthermore, with modification such an approach should prove to be generally applicable to problems in strong-field physics beyond attosecond pulse reconstruction, such as the reconstruction of attosecond processes in atoms and molecules in the presence of strong fields.

As near-single-cycle field transients are becoming available [3, 47, 48], it will clearly be advantageous to use one measurement to simultaneously characterize both a complex IR pulse, that might not satisfy the above approximations, along with a broadband EUV pulse.

4.2 Algorithm Design

In order to solve for the attosecond pulse without the need of a Fourier Transform, a least squares (LS) minimization is performed directly in the frequency domain. A figure of merit, M, is defined as

$$M = \sum_{l=0}^{N_W-1} \Delta W[l] \sum_{m=0}^{N_\tau-1} \Delta\tau \left| \tilde{a}[l,m] - \tilde{a}'[l,m] \right|^2. \tag{4.1}$$

The bracket notation indicates a sampled form of the corresponding continuous function. The matrix $\tilde{a}[l, m]$ is calculated by numerically integrating equation (3.3)

$$\tilde{a}[l, m] = -i\Delta t \sum_{n=0}^{N_E-1} \tilde{d}_{(k[l]+A[n+Lm])} \tilde{E}_X[n] \exp\left\{i\left(I_p + k[l]^2/2\right) n\Delta t\right\} \times \exp\left\{-i\Delta t \sum_{b=n+Lm}^{N_A-1} \Phi[l, b]\right\}, \quad (4.2)$$

where N_E is the number of points comprising $E_X[n]$, and the action induced energy shift, $\Phi[l, n]$, is given as

$$\Phi[l, n] = k[l]A[n] + A[n]^2/2. \quad (4.3)$$

As with the least squares generalized projection algorithm (LSGPA) [22], the time resolution of $\tilde{E}_x[n]$ and $A[n]$ is set to be $\Delta t = \Delta\tau/L$, and the reader is referred to [22] for a more detailed explanation of how the delay step is implemented. While here we assume a uniform L as a function of delay for simplicity, non-uniform delay steps could easily be accounted for by making L a function of delay [22]. Also, as with LSGPA, using such a delay approach assumes no periodicity in delay of the spectrogram. The matrix $\tilde{a}'$ is formed by taking the current $\tilde{E}_X[n]$ and $A[n]$, calculating $\tilde{a}[l, m]$, and then the projecting the measured amplitude onto it. This is expressed as

$$\tilde{a}'[l, m] = \sqrt{P[l, m]} \exp\left\{i \arg(\tilde{a}[l, m])\right\}. \quad (4.4)$$

The initial squared error in equation (4.1) is then simply due to any difference between the square root of the measured spectrogram, $\sqrt{P[l, m]}$, and $|\tilde{a}[l, m]|$ calculated using the current $E_X[n]$ and $A[n]$. The error is summed across all N_τ delay points and N_W energy points. The calculation in equation (4.2) is more related to a discrete Fourier transform of a non-periodic function in time as opposed to a fast Fourier transform (FFT). This removes the strict relationship between the energy and time sampling of an FFT, and removes the need to interpolate the measured spectrogram. To accommodate for a nonlinear energy spacing in the figure of merit

calculation, the energy resolution at each l, $\Delta W[l]$, is included. The discrete integral in equation (4.2) is however different from a discrete Fourier transform as the outgoing state is described by a Volkov wave [33] rather than a plane wave. Thus, since we are preserving the Volkov wave basis set in this algorithm, it is called the "Volkov transform" generalized projection algorithm (VTGPA). At this point, all of the components are in place to set up a minimization routine for determining the next update of $\tilde{E}_X$. We perform a LS minimization using the figure of merit by writing $\tilde{E}_x[n] = \alpha_n e^{i\phi_n}$, and solving for each term α_n, ϕ_n such that

$$\frac{\partial M}{\partial \alpha_n} = 0 \tag{4.5}$$

$$\frac{\partial M}{\partial \phi_n} = 0. \tag{4.6}$$

The solutions of this system of equations are then combined to yield

$$\tilde{E}_X[n] = \frac{-\left(\tilde{\Gamma}[n] + \tilde{\beta}[n]\right)^*}{\sum_{l=0}^{N_W-1} \Delta W[l] \sum_{m=0}^{N_\tau-1} \Delta\tau \left|\tilde{d}_{k[l]+A[n+Lm]}\right|^2}, \tag{4.7}$$

where

$$\begin{aligned}\tilde{\Gamma}[c] = \sum_{l=0}^{N_W-1} \Delta W[l] \sum_{m=0}^{N_\tau-1} \Delta\tau \sum_{\{n\in\mathbb{Z}|0\leqslant n<N_E, n\neq c\}} & \Delta t^2 \tilde{d}_{k[l]+A[c+Lm]} \tilde{d}^*_{k[l]+A[n+Lm]} \tilde{E}^*_X[n] \\ & \times \exp\left\{i(I_p + k[l]^2/2)\Delta t(c-n)\right\} \\ & \times \exp\left\{i\Delta t \sum_{b=n+Lm}^{N_A-1} \Phi[l,b]\right\} \\ & \times \exp\left\{-i\Delta t \sum_{b=c+Lm}^{N_A-1} \Phi[l,b]\right\}, \end{aligned} \tag{4.8}$$

and

$$\tilde{\beta}[c] = i \sum_{l=0}^{N_W-1} \Delta W[l] \sum_{m=0}^{N_\tau-1} \Delta\tau\Delta t \tilde{d}_{k[l]+A[c+Lm]} \exp\left\{i(I_p + k[l]^2/2)c\Delta t\right\} \times \exp\left\{ -i\Delta t \sum_{b=c+Lm}^{N_A-1} \Phi[l,b] \right\} \tilde{a}'^*[l,m]. \quad (4.9)$$

At each iteration step, the current $\tilde{E}_x$ and A vectors are used to form $\tilde{a}'$, and the updated value of $\tilde{E}_X[n]$ is calculated using equation (4.7). This term is then loaded into the $\tilde{E}_X$ vector, and the process repeated with the next term. The algorithm worked best when moving sequentially from term 0 to term $N_E - 1$, and then moving backwards from term $N_E - 1$ down to term 0 to achieve a balance in how the first and last half of the vector are calculated. For instance, when moving strictly from term 0 to term $N_E - 1$, an asymmetry forms between the left and right half of the retrieved EUV pulse creating an instability that grows as the algorithm progresses.

While $E_X[n]$ can be solved using a LS approach, solving for $A[n]$ in this manner is not as straightforward. However, a more direct solution exists as much more experimental information is typically known about $A[n]$. For streak pulses, the precise central wavelength, bandwidth, peak intensity, and, often, pulse duration are known to within reasonable bounds, making a bounded minimization routine possible. Rather than letting each sample in $A[n]$ be fit independently as in other routines, the vector potential can be broken down into a few key terms describing the envelope and carrier portions of the wave. The envelope, $A[n]$, can be described as a cubic spline between J points, and the carrier wave using K coefficients as $\cos(\alpha_0 + \alpha_1 t + ... + \alpha_{K-1} t^{K-1})$. Thus, only $J + K$ terms are used to describe $A[n]$. As an example, for a pulse with a central wavelength of 800 nm and duration of 10 fs, typically only one to two points per cycle are necessary to describe the envelope. Even if one uses up to six α terms to describe the chirp, this gives just 14 terms to fit. It is straightforward in this case to directly minimize the figure

of merit for each term, given by

$$M_A = \sum_{l=0}^{N_W-1} \Delta W[l] \sum_{m=0}^{N_\tau-1} \Delta\tau \left| \left|\tilde{a}[l,m]\right| - \sqrt{P[l,m]} \right|^2. \tag{4.10}$$

To minimize each term, Brent's method was used [56,57]. In order to speed up the minimization, the bounds on each term were adaptively reduced as the algorithm converged. This can be further extended to synthesized pulses, where one could create $A[n]$ by summing multiple pulses, each having its own envelope and carrier components. An example demonstration of an $A[n]$ calculation is shown in figure 4-1a, and the entire algorithm is outlined in figure 4-1b (a similar flowchart of other FROG-CRAB algorithms can be found in [22] for comparison). An added benefit of reducing the amount of terms used to fit $A[n]$ is that less data is necessary to fit the both the IR and XUV pulses. In fact, in most cases using spectrogram data from just on cycle of the streak pulse was more than enough to get a full fit of the EUV pulse. Thus, for a full experimental trace, multiple retrievals of the EUV pulse could be performed to obtain statistics. It was found in practice that the fit for $A[n]$ converges much faster than the fit of $\tilde{E}_X$, meaning that the algorithm could be sped up further by minimizing $A[n]$ less and less often as the algorithm progresses, rather than every cycle as performed here.

4.3 Results

4.3.1 Modeling

The VTGPA was tested and compared to LSGPA using a simulated spectrogram. The spectrogram was created using an attosecond pulse having a cosine squared profile in the energy domain with a bandwidth of 120 eV and a group delay dispersion of -2.17×10^{-3} fs^2. To this pulse, a small side-lobe was added having the same profile, but with a bandwidth of 100 eV, the same chirp, a time separation of 100 as, and roughly 1/4 peak electric field magnitude. The IR streaking pulse

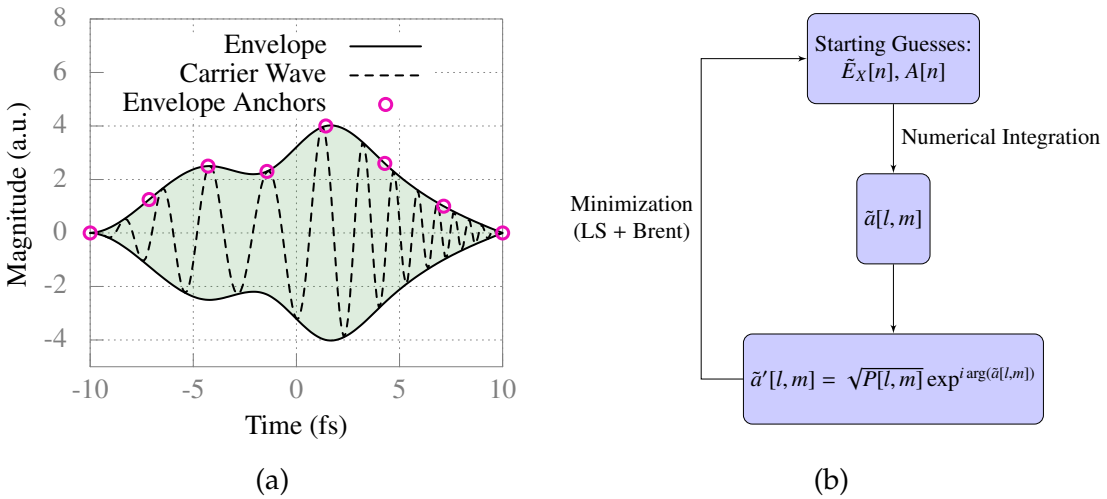

(a) (b)

Figure 4-1: (a) Plot demonstrating how A is formed from a carrier and envelope function. The circles represent the amplitude handles used to create a spline-fit. In this plot, a fourth order polynomial was used to represent the carrier wave underneath, making for a total of 13 terms. To fit the same function with a time resolution of 50 as using LSGPA or PCGPA would require 400 terms. (b) A flowchart of the modified algorithm. The flowchart has fewer elements than other GPA approaches, but more computation is being performed in the minimization step. The key is that no FFTs are used, and the minimization is performed directly in the frequency domain.

had a center wavelength of 800 nm, an envelope duration of 10 fs full width at half maximum (FWHM), a linear chirp of 25.5×10^{-3} fs^{-2}, and a peak intensity of 1×10^{12} W/cm^2. Argon was used as a target gas in the simulation. The dipole transition matrix element used for simulating the spectrogram was calculated using the method described in [37]. The resulting spectrogram is shown in figure 4-2.

Each algorithm was configured to stop after reaching a convergence criterion, which was set to be when the percent difference between the current figure of merit value, as defined by M_A, and previous figure of merit, M'_A, is less than 1×10^{-5}, i.e.

$$\frac{2(M_A - M'_A)}{M_A + M'_A} < 1 \times 10^{-5}. \tag{4.11}$$

Comparisons of the results are shown in figure 4-3.

While the VTGPA result retrieves the exact pulse envelope and phase, LSGPA suffers significant error. In fact, it appears as if the LSGPA simply retrieves a near transform-limited pulse with a duration roughly half that of the actual pulse. To

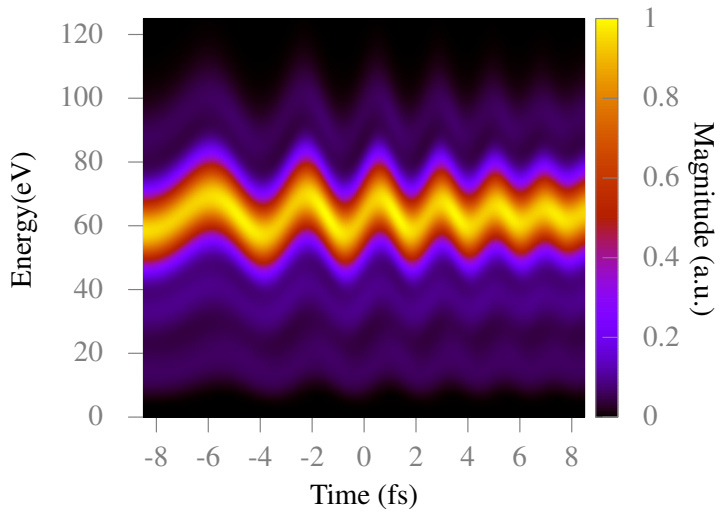

Figure 4-2: Simulated spectrogram used for testing the reconstruction.

verify the fundamental source of the error, the retrieval was performed on a spectrogram using the same input pulses, only this time assuming a flat DTME. The retrieved pulse in this case had an almost identical error, indicating that the central momentum approximation in the action term was the dominant source of discrepancy. For the streaking pulse, the LSGPA algorithm underestimates the peak field amplitude, and has the addition of extra, unphysical noise due to the differentiation step when converting from $\Phi(t)$. This is not an issue in VTGPA as the peak amplitude is fitted correctly, and there is no additional noise as it is constrained to a smooth function. With regard to the streak intensity, it has been shown that algorithms such as the principle components generalized projection algorithm (PCGPA) and LSGPA are even less effective if the streaking energy is reduced below 1×10^{13} W/cm^2 for EUV pulses of such large bandwidth [25]. However, using the same EUV input pulse as above, VTGPA was tested down to a streak intensity of 1×10^{11} W/cm^2 without any loss in accuracy. Furthermore, for pulse trains, VTGPA successfully retrieved pulses with streaking intensities as low as 1×10^{9} W/cm^2. This is advantageous for avoiding such phenomena as Stark shifts and background electron contamination from ATI during measurement.

Any actual measurement will of course have noise, and to give a proper comparison of each algorithm's performance under more realistic conditions, Poisson

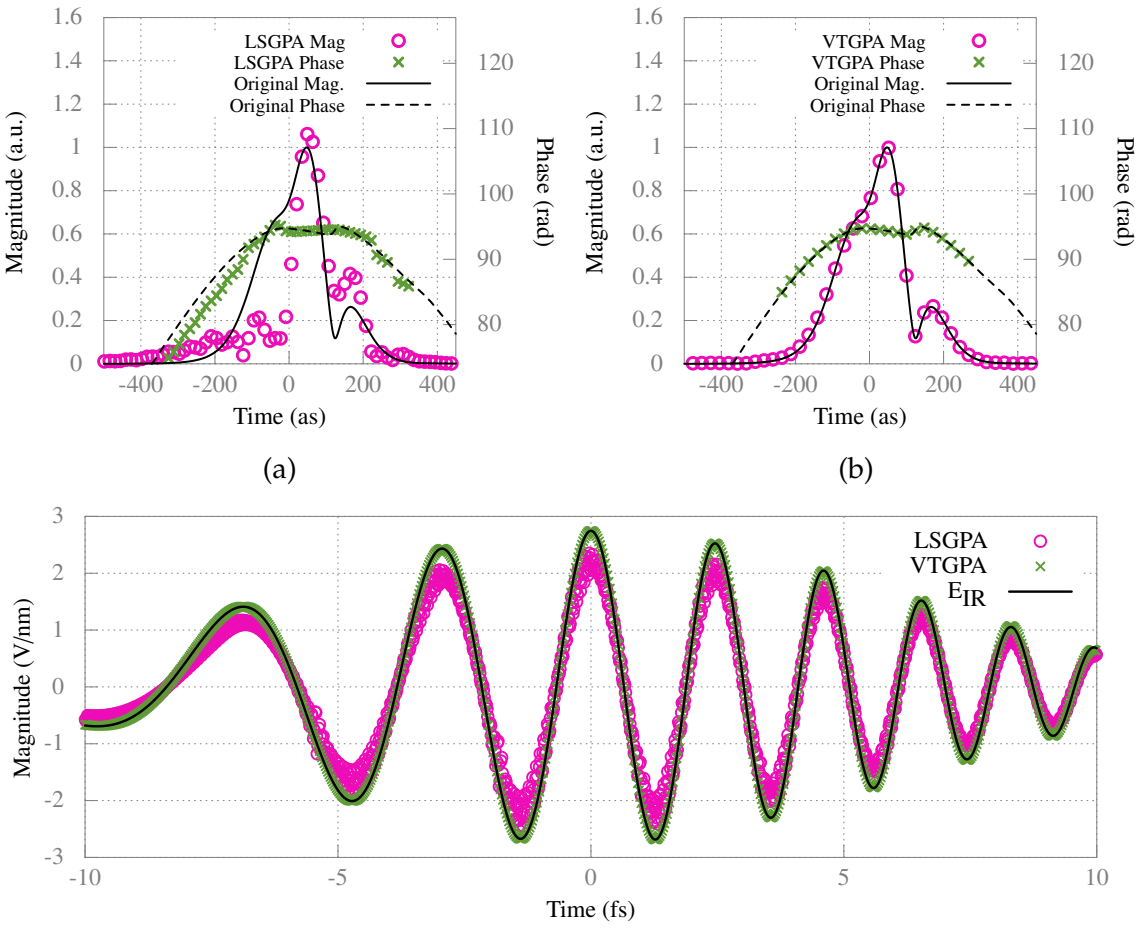

Figure 4-3: (a) LSGPA retrieval of $\tilde{E}_X$. As others have observed [25], the algorithm retrieves a pulse much shorter than the actual value, in this case roughly 50% of the actual FWHM. While the sidelobe location is correct, the sidelobe intensity is incorrectly retrieved. (b) VTGPA retrieval of $\tilde{E}_X$. (c) Comparison of the IR field retrieval using both algorithms. While LSGPA correctly retrives the shape of the IR field, the peak field strength is underestimated, as noted in [22]. Also, since it retrieves a fit to $\int_t^\infty \Phi(t')dt'$, not $E_{IR}(t)$ directly, it also increases the noise of the fit due to differentiation. On the other hand, the VTGPA routine forces $A(t)$, and thus $E_{IR}(t)$, to be described by a smooth function which does not introduce extra noise into the fit, and the field magnitude is correctly retrieved.

noise was added to the spectrogram in figure 4-2. The magnitude of the noise resulted in the spectrogram having a signal to noise ratio of SNR ≈ 7.7, where SNR is defined as

$$\mathrm{SNR} = \frac{\sqrt{\sum_{l,m} P[l,m]^2}}{\sqrt{\sum_{l,m} N[l,m]^2}}, \tag{4.12}$$

and $N[l, m]$ is the noise amplitude at each pixel location. The resultant spectrogram after adding noise is shown in figure 4-4, and the results of the two retrieval algorithms are shown in figure 4-5.

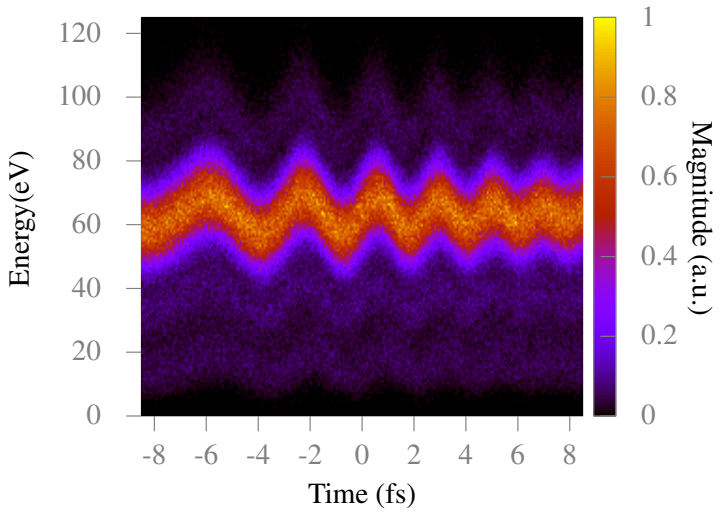

Figure 4-4: The spectrogram after the addition of Poisson noise.

The LSGPA algorithm fared significantly worse in the presence of noise, again retrieving a main pulse shorter than the actual duration, with an added pedestal at earlier times that extends out to roughly twice the width of the actual pulse. Furthermore, while it does retrieve a side lobe after the main pulse, the side lobe's intensity and location are retrieved incorrectly. On the other hand, the VTGPA algorithm retrieved a pulse that matches much better to the original pulse shape, having a duration that is slightly shorter. More importantly, the side lobe location and intensity are both accurately retrieved. For the VTGPA retrieval shown in figure 4-3b, only a single cycle of the streak pulse near the center of the spectrogram was necessary to fit the EUV pulse, while in the presence of noise this was extended to roughly four cycles to make the system more overdetermined and improve the fit. However, in all cases, the LSGPA was performed using the entire delay range of the spectrogram.

The streaking pulse retrieval results shown in figue 4-5c demonstrate how the noise in the LSGPA result gets further magnified due to the differentiation step necessary for converting the streaking phase result into the streaking electric field

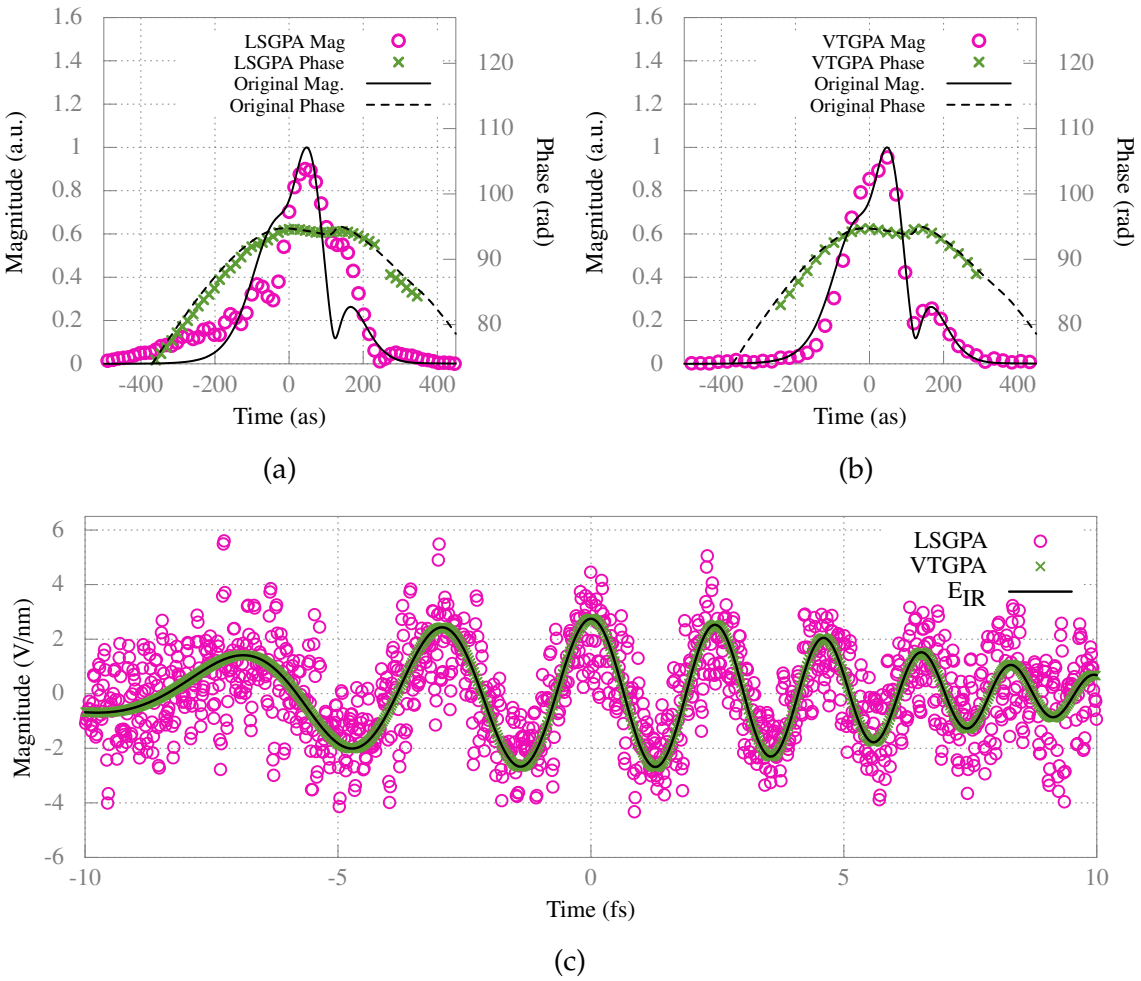

Figure 4-5: (a) The LSGPA results after the addition of Poisson noise to the spectrogram. Again the pulse width is underestimated, but now there is the development of a long pedestal, and neither the sidelobe location and intensity are retrieved accurately. (b) The VTGPA results. While there is a slight amount of error introduced, the overall pulse shape, width and sidelobe are all quite accurately retrieved. (c) Comparison of retrieval results for the IR streaking pulse using both algorithms. There is no loss of accuracy for the VTGPA routine, while the LSGPA results suffers considerably due to the differentiation step.

waveform. Again, the VTGPA algorithm does not suffer this issue as it is fitting a smooth envelope and carrier function that is not allowed to have unphysical jumps in electric field from one time sample to the next.

4.3.2 Experimental

To put the VTGPA algorithm to practice, it was used to reconstruct an experimentally collected spectrogram. The spectrogram was collected over a range of photon

energies (roughly 18-40 eV) where the DTME of the target gas, in this case Ar, is highly dispersive [37]. While the LSGPA or PCGPA could be used to retrieve a pulse in this range, their inability to fully account for the DTME means that the result could not be trusted.

The HHG was generated using a commercial, regeneratively amplified 800 nm pulsed laser system with a pulse duration of 35 fs. The pulse was split into two arms, one for driving the HHG process, the other for streaking the photoelectrons. In the drive arm, the beam was focused into a glass capillary filled with Ar gas using a curved mirror with a focal distance of 25 cm, achieving peak intensities on the order of 1×10^{14} to 1×10^{15} W/cm^2. In order to add complexity to the HHG pulse, a 200 μm thick beta barium borate (BBO) crystal was placed before the curved mirror to generate the second harmonic of the 800 nm light, resulting in the generation of both odd and even harmonics. Furthermore, a half-waveplate was used before the BBO to slightly detune the polarization of the input pulse relative to the BBO crystal. Input pulse energy, beam aperture size and the half-waveplate angle were tuned for optimum even-harmonic flux. After the capillary, the IR pulse was removed, and the EUV pulse was spectrally filtered using a 500 nm thick, suspended Al foil. The EUV pulse was then focused at the target region in front of the spectrometer using a Au coated toroidal mirror.

The streaking pulse was sent through a piezo-controlled delay line, followed by an iris and a focusing lens. The EUV and streak beams were then recombined using a drilled mirror having a roughly 2 mm aperture. The intensity of the streak beam was controlled by adjusting the opening size of the iris in the streak arm. In this case, a relatively weak streak intensity was used, having a peak intensity of just 1.6×10^9 W/cm^2 according to the VTGPA fit. The electron spectra were collected using a time-of-flight electron spectrometer. In order to calibrate the electron spectra, a Rowland circle EUV spectrometer was used to simultaneously measure the EUV spectrum. The measured streaking spectrogram and fit results are combined in figure 4-6.

The spectrogram retrieved by the VTGPA matches very well with the measured

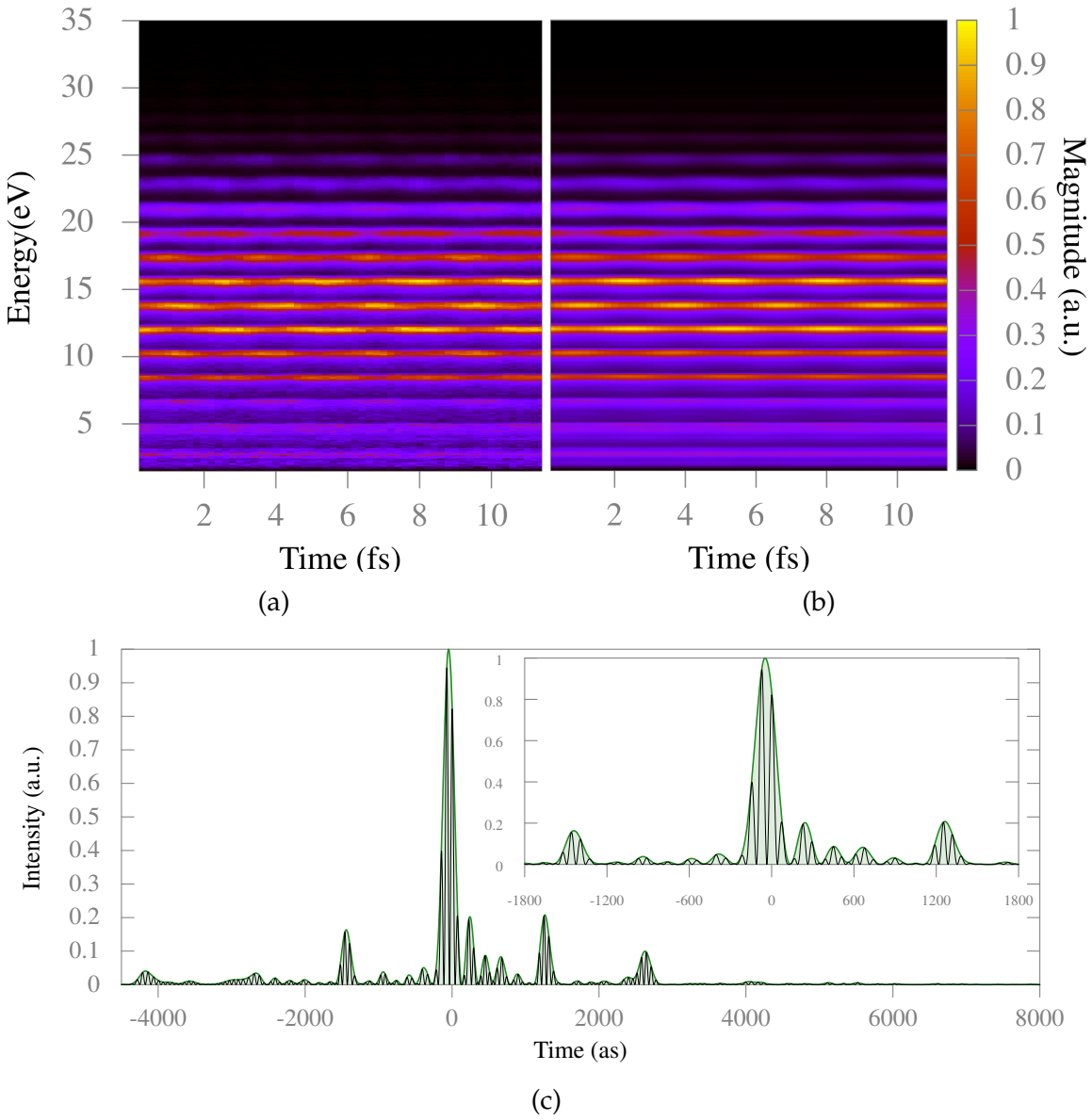

Figure 4-6: (a) The experimentally measured spectrogram. (b) The fitted spectrogram using VTGPA, accounting here for both the dipole transition matrix element and the transfer function of the TOF spectrometer to properly match the measured spectrogram in (a). (c) Retrieved XUV pulse intensity profile showing both the instantaneous field intensity, $(\mathrm{Re}(\tilde{E}_X))^2$, and envelope intensty, $|\tilde{E}_X|^2$. The inset shows a zoom around the largest peak and first two side-lobes. Note that an arbitrary carrier envelope phase has been chosen, as the algorithm can only resolve the pulse down to a constant phase factor.

spectrogram. As with the results reported in [24], the attosecond pulse train has contributions from each half-cycle. The even harmonics thus arise mostly due to a non-π phase shift between each EUV pulse in time, which breaks the anti-symmetry necessary for the generation of only odd harmonics. The fact that the

phase shift between consecutive harmonics in the plateau region is close to $\pi/2$ also explains why the beat notes generated there form the observed checkerboard-like pattern (i.e. the beat note maximum of each harmonic is lined up with the beat note minimum of an adjacent harmonic). As discussed briefly in [58], an infinite pulse train with identical pulse envelopes, but an alternating phase of Θ will have harmonics having complex amplitudes given by

$$\tilde{d}_N = \tilde{F}_N\{1 + (-1)^N e^{i\Theta}\}, \tag{4.13}$$

where $\tilde{F}_N$ is a complex constant depending on the harmonic number N, and the phase offset from one half-cycle to the next is given by Θ. For example, single-color HHG yields odd harmonics since $\Theta = \pi$. However, even a very mild second harmonic breaks this relationship, whether aligned purely parallel, orthogonal, or a mixture of both, as in our experimental arrangement. It is worth noting that a phase shift of $\Theta \approx \pi/2$ in the action phase alone is achievable with a perpendicular second harmonic component of just 0.25% of a fundamental intensity of 4×10^{14} W/cm^2 according to the semiclassical three-step model. While our experimental conditions are not this simple, with both a stronger parallel and slight perpendicular components to the second harmonic and a non-infinite series of non-identical EUV pulses, it is clear that such phases are easily attainable with second harmonic fields that would not strongly influence the ionization rate and recombination energy of harmonics in subsequent half-cycles. The experimentally retrieved phase shifts between harmonics in both the time and frequency domain are shown in figure 4-7 for comparison.

4.4 Conclusion

A new algorithm, entitled VTGPA or "Volkov Transform" gernalized projections algorithm, has been introduced. This method fully accounts for the complex action phase and DTME of the ionization process as dictated by the SFA without any

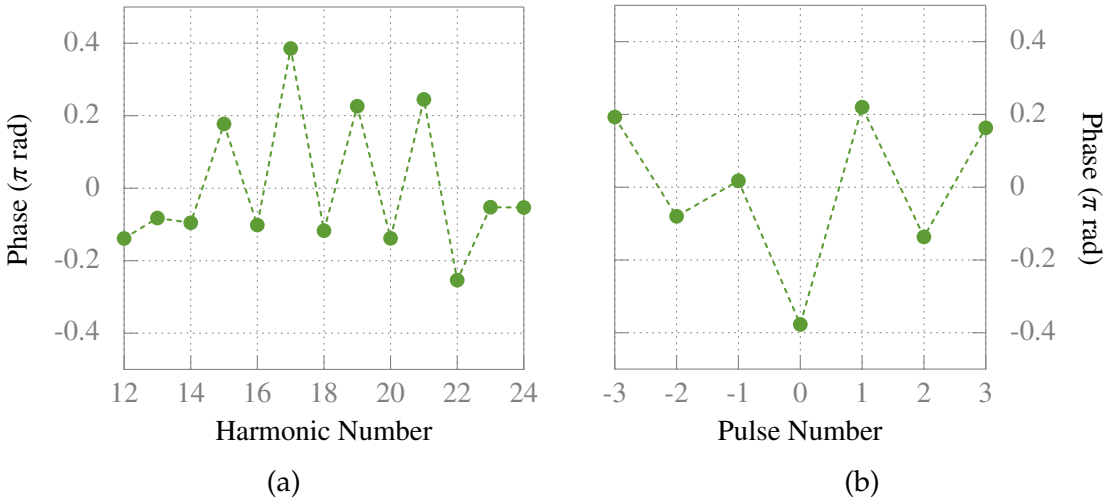

Figure 4-7: (a) The absolute phase retrieved for each harmonic throughout the HHG plateau. (b) The absolute phase retrieved at the center of each pulse in the time domain.

further approximations. Furthermore, it has been compared with the current state-of-the-art algorithm for FROG-CRAB, the least squares generalized projections algorithm, clearly demonstrating how it is not susceptible to errors introduced by the central momentum approximation and incorporation of the target atom's DTME. Furthermore, due to the nature of how the minimization routine is set up, there is no need to interpolate the experimental data as a nonlinearly sampled energy axis in the spectrogram is allowed. In all other respects, it has the advantage of any FROG-CRAB algorithm in that it also does not place any strong limitations on the IR streaking field, making it useful as an in-situ characterization tool for both a complex IR field and an attosecond pulse.

Since VTGPA is able to accurately retrieve attosecond EUV pulses with very low peak streaking intensities, tested down to 1×10^{11} W/cm^2 for an isolated pulse with $\sim$ 100 eV bandwidth and 1×10^{9} W/cm^2 for a pulse train with $\sim$ 30 eV bandwidth, interfering processes such as ATI and Stark shifting can be avoided. Also, at these intensities it will provide a tool for investigating and comparing results with methods such as iPROOF, which is based on perturbation theory not the strong-field approximation, to gain a better understanding of both approximations and improve theoretical methods for approximating the complex DTMEs used in the

SFA.

With future work, the minimization steps could be further improved and optimized for speed, perhaps using techniques that have already been employed in FFT algorithms for efficiency improvements in the computation of discrete Fourier transforms. While the VTGPA was presented here in the context of attosecond pulse retrieval, it is felt that the overall approach should find further application in other strong-field physics studies after slight modifications.

Chapter 5

Strong-Field Emission From Nanostructures

5.1 Why Nanostructures?

Strong-field (SF) emission from nanostructures has gained much interest in recent years as it is an enabling technology for the generation of structured, ultrafast electron bunches. Such electron arrays have potential applications in diffractive electron imaging [59] and novel, compact free-electron X-ray sources [60]. State of the art ultrafast cathodes are typically planar cathodes that utilize highly reactive low work function materials in conjunction with an ultrafast (tens to hundreds of fs in duration), ultraviolet (UV) pulse that emits electrons via one-photon absorption. There are two major issues with such a cathode design. First, there is no clear means of providing spatial structure with high resolution. Second, the materials used to achieve low work functions for high efficiency are difficult to fabricate, suffer from poor lifetime, and necessitate ultra-high vacuum ($\sim 10^{-10}$ mbar or better). Utilizing near-field enhancement and a multiphoton emission process, nanostrucuted cathodes driven by ultrafast, long-wavelength (i.e. near-IR or longer) drive sources present a solution to all of these issues.

Since nanostructures can interact with incident light to produce very high peak

intensities ($> 1 \times 10^{12}$ W/cm^2) over a very small volume, spatial structuring of the emitted electron beam is a natural consequence. For instance, since the electron affinity of Si is 4.05 eV, the absorption of three photons at 800 nm is required to liberate an electron. This implies a charge scaling of I^3, where I is the peak intensity of the laser pulse on the surface of Si. If the local field enhancement is 20 for a nanostructure as opposed to 2 for a planar surface, then the probability of emission near the localized region of field enhancement is a factor of 1×10^6 greater than the planar region. Furthermore, the SF, or tunneling, regime of emission can be achieved before the onset of material damage. As discussed earlier in the text in the context of attosecond pulse generation and characterization, in the SF regime electron emission occurs over durations shorter than just one half-cycle of the drive laser. At 800 nm this implies the formation of a train of electron pulses less than 1.33 fs in duration spaced by 2.66 fs when driven fully into the tunneling regime. Thus, nanostructured cathodes hold the potential of creating high-brightness electron sources with unprecedented spatial and temporal resolution. Due to the advancements in the field of nanofabrication, they can also be created from abundant, robust materials with relatively high damage thresholds (for instance Si, or Au) that do not require ultra-high vacuum during operation.

Hallmarks of such emission have recently been observed for single-tip emitters of Au and W [15,16]. In this chapter the author will discuss his observations of the SF emission process from large arrays of Si tips [11,26]. Fundamental concepts of SF electron emission from solids will be reviewed, including a discussion of both the multiphoton and tunneling regimes, as well as classical electron trajectories, rescattering and effects of electric field decay away from the tip surface. Space charge effects will also be briefly discussed. In Section 5.3, experimental results and analysis that demonstrate SF emission from arrays of silicon tips are shown. These results include intensity scaling of electron yield, space-charge and DC bias effects, electron energy spectra, polarization dependence, oxide effects and a brief study of two-color driven electron emission. These results all indicate that a SF driven multiphoton/tunneling process is the dominant emission mechanism from

the tip surface.

5.2 Fundamental Concepts

5.2.1 Emission Mechanisms

In order to discuss the dominant emission mechanisms expected from a nanstructured emitter, a simple model of the system is needed. To within a reasonable approximation, the potential well of a metal or semiconductor looks like a step potential at the surface/vacuum interface. In all cases that follow, we consider an excitation field that is polarized along the surface normal. As only metals and doped semiconductors will be considered in the analysis, it is also safe to assume from Maxwell's equations that, for reasonably long wavelengths, the electric field inside of the material is negligible when compared to the field in the vacuum half-space. With this picture in mind, we arrive at a system as sketched in Figure 5-1.

The time dependent potential of the optical pulse's oscillating electric field provides a means of perturbatively coupling the bound portion of the ground state in the vacuum half space to outgoing electron wavepackets. Since we are dealing with longer wavelength drive sources of relatively high field strength, it is important, as discussed in Chapter 2, to include the effect of the strong electric field into the calculation of the outgoing wavepacket. Only the electric field of the laser exists outside of the tip material, so representing the outgoing wavepacket as a sum of Gordon-Volkov waves is again the preferred approach.

To start, consider that the incoming wave is a CW field with period T in time that is suddenly turned on at time $t = 0$. Also assume that it is a one dimensional problem. For the case of minimal electron rescattering, Equation (2.18) can be used to calculate an approximation of M_p,

$$M_p \approx M_p^{(1)} = \frac{-i}{\hbar}\int_0^t d\tau g(\tau, p) e^{i\left(p^2/(2m)+q^2A_0^2/(4m)+W_0\right)t/\hbar}, \tag{5.1}$$

where A_0 is the magnitude of the vector potential, and W_0 is the ground state

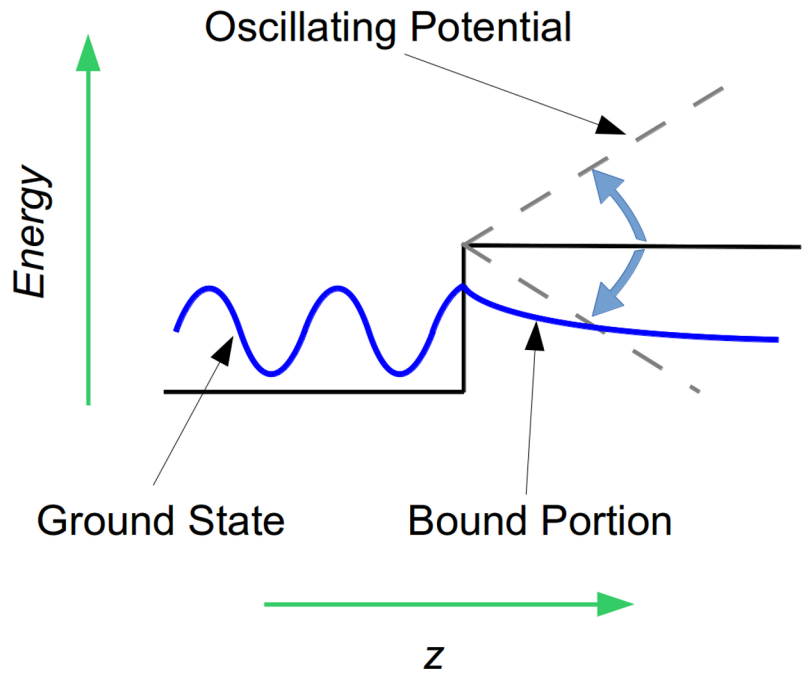

Figure 5-1: Schematic showing model system for conductive emitter. A bound electron inside of the emitter has an evanescently decaying component in the vacuum half space. This portion of the wave function is perturbatively coupled to outgoing states through the oscillating potential on the outside created by the incident optical pulse.

energy. The expression $g(t,p)$ is simply a collection of all of the pre-factor terms, and is periodic in time with period T. Due to its periodic nature, it can be rewritten as

$$g(t,p) = \sum_n f_n(p) e^{-in\omega_0 t}, \tag{5.2}$$

where $\omega_0 = 2\pi/T$ is the fundamental angular frequency, and

$$f_n = \frac{1}{T}\int_{-T/2}^{T/2} dt g(t,p) e^{in\omega_0 t}. \tag{5.3}$$

After rearranging the terms, M_p becomes

$$M_p = \frac{-it}{\hbar}\sum_n f_n(p) e^{iX(p)t/(2\hbar)}\,\mathrm{sinc}\left(\frac{X(p)t}{2\hbar}\right), \tag{5.4}$$

where $X(p) = p^2/(2m) + q^2A_0^2/(4m) + W_0 - n\hbar\omega_0$. Notice that as the exposure

time t increases, the sinc function becomes more and more peaked. Eventually, as $t \to \infty$, the sinc function approaches a δ, and only one momentum value, p_n, falls underneath the main peak for each given n such that $X(p_n) = 0$. For the calculation of total electron yield, the more relevant term is $|M_p|^2$, which becomes

$$|M_{p_n}|^2 = \frac{2\pi}{\hbar^2}|f_n(p_n)|^2 t\delta\left(\frac{X(p_n)}{\hbar}\right), \tag{5.5}$$

where we have made use of the fact that

$$\lim_{t\to\infty} t\,\mathrm{sinc}^2\left(\frac{X(p)t}{2\hbar}\right) = 2\pi\delta\left(\frac{X(p)}{\hbar}\right). \tag{5.6}$$

To then calculate the total emission for this one dimensional problem, one simply integrates

$$\Gamma \propto \int_0^\infty |M_p|^2 dp \propto \sum_{n\geqslant n_{min}} \frac{1}{p_n}|f_n(p_n)|^2, \tag{5.7}$$

where Γ is the electron emission rate, and n_{min} is the minimum photon absorption necessary to make the outgoing momentum p_n real.

This has many parallels to a more traditional approach to perturbation theory, with one major difference. First, as time goes to infinity, the outgoing momenta become peaked around discrete harmonics. These are positioned such that the electron energy spectrum forms a train of harmonics spaced by the fundamental photon energy. Thus, it is describing a multi-photon absorption process. Second, the total ougoing charge grows linearly with time, i.e. at a constant rate. However, the major difference is a result of a non-negligible ponderomotive potential, U_p, which adds to the potential barrier of the boundary. As the intensity is increased, the electrons must absorb enough photons to surpass not just the work function, but also the ponderomotive potential of the laser field. For most multiphoton absorption processes in solids, the material damage and short wavelengths prevent an observation of this effect. However, this is not the case for nanostructures with high field enhancements and driven with long wavelengths.

As the the intensity, and, consequently, U_p, is increased, there is the possibil-

ity that a previously "open" photon channel becomes "closed". Take for example a material with a work function of 5.0 eV. In this case, the step barrier an electron has to overcome would require the absorption of 4 photons given a photon energy of 1.55 eV. At low intensities, four-photon absorption dominates the emission process, and the charge yield scales as I^4. However, if U_p exceeds 0.6 eV, the four-photon channel closes, and only channels $\geqslant 5$ remain open. This leads to a kink in the charge yield as a function of input intensity, which is the hallmark of strong-field emission [16, 26] (see Figure 5-2).

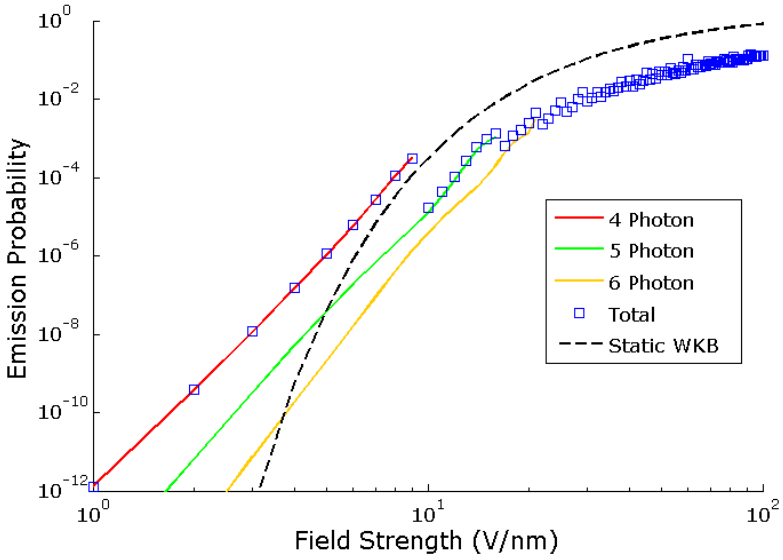

Figure 5-2: Charge yield as a function of increasing field strength for a CW drive beam. The central photon energy used was 1.55 eV. The work function of the material was taken to be $W_0 = 5.0$ eV. Each channel contribution is shown (solid curves), along with the total sum of all contributions (blue squares). For reference, the WKB tunneling rate is shown (black dashed). The minimum channel number possible is the four-photon channel. After this channel closes, a kink forms, and successive channels close afterwards creating a smoother and smoother line, which approaches the WKB rate at high intensities. This is the so-called SF or tunneling regime.

After the kink forms due to the onset of channel closing, successive channels close leading to an average rate that approaches that of the WKB approximation for tunneling. In fact, this is seen by taking the saddle point approximation of M_p as discussed in Section 2.2.2, which was performed in detail in [38]. In this regime, the physical picture is the same as for attosecond pulse generation using HHG,

only this time we are primarily concerned with electrons that escape rather than those that recombine and emit a photon. The potential barrier is bent down in the vacuum half-space creating a triangular barrier. When the complex tunneling time is then shorter than one optical cycle, the electron has a high probability of tunneling directly through the barrier. Once in the vacuum, the dominant trajectories are those described by classical mechanics, which will be discussed in the following section.

While this calculation has been described in only one dimension for CW driver, any nanostructured tip clearly exists in three dimensions, and there is more interest in using drive pulses that are just fs in duration. Methods to include the area of the tip emitter and solve for the total emission for an arbitrary pulse shape and ground state distribution of the cathode are described in detail in Appendix B. With regard to the size of the emitter, it is shown that the overall emission rate scales in direct proportion to the one dimensional calculation with a pre-factor that depends on the area of the emitter. Thus, to within a good approximation, the one dimensional calculation suffices when discussing the emission rate alone. However, it can dramatically affect the spatial momentum distribution of the outgoing electrons, primarily due to the uncertainty principle, which dictates that as the tip emitter is scaled to smaller sizes, the momentum distribution must conversely be more spread out in space. Again, the interested reader is directed to Appendix B for a more thorough discussion.

Equation (B.11) can be used for an arbitrary electric field pulse and compared against the results for a CW pulse for a given emitter. The results of such a comparison are shown in Figure 5-3. For this study, the ground state energy was chosen to be $W_0 = 4.05$ eV, which corresponds to the electron affinity of silicon. The incident photon energy was again taken to be 1.55 eV. The inclusion of a pulse envelope necessitates that the photon energy no longer be perfectly defined, which results in smoothed-over channel closings. This effect gets more dramatic as the envelope is shortened, and/or the wavelength increased. Furthermore, if the pulse energy is weakened to a great extent, the slope reduces (not shown in the figure). This is due

to the fact that, while most of the pulse energy is contained in the spectral region near the central wavelength, for a broadband pulse there do exist very high energy photons. At very low intensities, the cross section for a lower-order absorption of these photons makes up for their reduction in number, thus causing a change in the power scaling.

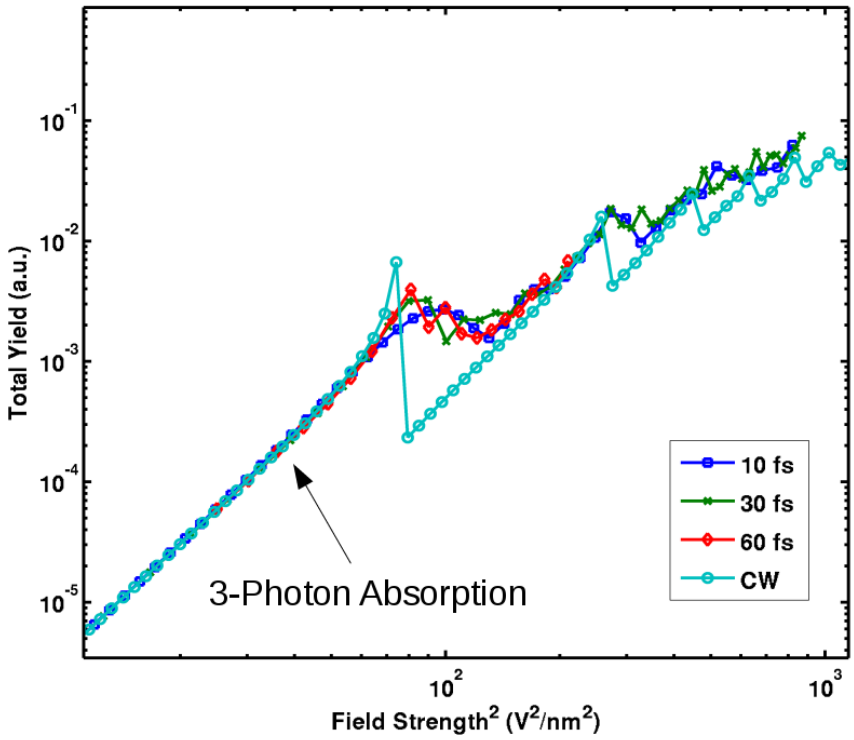

Figure 5-3: Intensity scaling of charge yield for various pulse durations for a silicon emitter ($W_0 = 4.05$ eV), with an incident photon energy of 1.55 eV. For all cases the first main channel closing is prevalent. However, while the channel closings are instantaneous for the CW input, the transitions are smoothed for short drive pulses. This is due to the fact that for a pulse, the input photon energy is less and less well defined as the pulse duration is shortened. From 60 fs down to 10 fs there is no significant difference in the overall shape of the curve.

5.2.2 Classical Trajectories and Rescattering

As stated in Section 2.2.2, when driven fully into the tunneling regime, the electrons follow mostly classical trajectories, and the emission rate is well described by the WKB approximation. This makes the Fowler-Nordheim static tunneling rate a useful tool in approximating the instantaneous tunneling probability when

considering contributions from the entire ground state distribution [38, 61]. Thus, by combining the Fowler-Nordheim emission rate with a calculation of classical trajectories, it is then easy to approximate the electron energy distribution in the tunneling regime.

For the calculation of electron emission in Section 5.2.1, it was assumed that the dipole approximation still holds, i.e. that over the excursion length of the electron, the electric field is relatively constant in magnitude. However, at the strong field strengths present in the tunneling regime, this begins to break down. While it only slightly perturbs the calculation of the emission rate, the decay of the electric field can greatly alter the electron energy distribution. It was shown in [13] that the electron excursion can become much larger than the field decay length, leading to a quenching of the electron quiver motion in the laser field. This is especially important for rescattered electrons that would otherwise gain up to 10Up inside of the field [27]. Thus, for all of the calculations of electron energy spectra, the shape of the electric field profile must be considered.

As an example of how the electron energy spectrum is calculated, take a dipolar electric field profile given by

$$F(z,t) = F_0(t)\left[(\xi-1)\left(\frac{\beta}{z+\beta}\right)^3 + \exp\left\{\frac{-2\log(2)z^2}{4w_0^2}\right\}\right], \tag{5.8}$$

where $F(z,t)$ is the electric field along the z axis away from the tip, $F_0(t)$ is the unenhanced on-axis field component, ξ is the field enhancement factor, β is the tip radius of curvature and w_0 gives the unenhanced field waist for a focused Gaussian beam. The spectrum is then formed by the following procedure. First, the emission rate is found as a function of time using the Fowler-Nordheim equation

$$J = \Theta(F_0(t))\frac{q^3|F(t)|^2}{16\pi^2\hbar\chi_{Si}}\left(\frac{m^*}{m}\right)\exp\left(\frac{4\sqrt{2m}}{3q\hbar|F(t)|}\chi_{Si}^{3/2}\right), \tag{5.9}$$

where J is the current density, Θ is the Heaviside function, $F_0(t)$ is the electric field in vacuum, m^* is the effective electron mass in Si, and χ_{Si} is the electron affinity

of Si. Only the negative half-cycles of the electric field contribute to emission, as a positive field just serves to drive the electrons back into the tip. Next, for each possible emission time, an electron at rest is assumed to suddenly appear at the tunnel exit of the triangular barrier formed at the emission time. Finally, once in the vacuum, the spatial electric field distribution is used to calculate the electron trajectory using classical mechanics. For a homogeneous field, the analytic solution can be used, however, for a general field profile, a Runge-Kutta method is used to solve for the electron trajectories. If the electron returns to the tip, it is assumed to reflect with some probability R. Using this trajectory, the final electron energy is calculated after the driving pulse has already passed. Each final electron energy is then weighted by the probability of emission at its birth time to form an electron energy spectrum. This general approach is known as the Simpleman Model [13, 27]. The model is shown schematically with example spectra in Figure 5-4.

There are always two major contributions to each spectrum. First are the electrons that directly escape the boundary, referred to as "direct" electrons. These electrons can only pick up a maximum of 2Up from the drive laser field, and form the high intensity low energy peak in the spectrum. Second are those electrons that return to and rescatter from the tip. As mentioned earlier, these electrons can pick up significantly more energy in the oscillating field (the classical limit being 10Up for an electron starting at rest from the surface in the dipole approximation) due to the sudden momentum reversal, and thus make up the extended plateau feature in each spectrum. As intensity is increased, the plateau extends outward rapidly, up to 10 eV for a relatively modest pulse energy of 600 nJ.

In order to see the effect of a rapidly decaying electric field magnitude away from the tip surface, an analysis of cutoff scaling can be performed. The cutoff is defined here as being at the energy W that satisfies the expression $P(W) = 0.1P(W/2)$, where P is the spectral intensity. In Figure 5-5 the cutoff scaling is shown for three electric field profiles: a homogeneous field, a simulated field decay from finite element modeling of a 5 nm radius of curvature Si tip (see methods of [11]), and a dipolar field with $\beta = 5$ nm. In all cases the material was taken to be

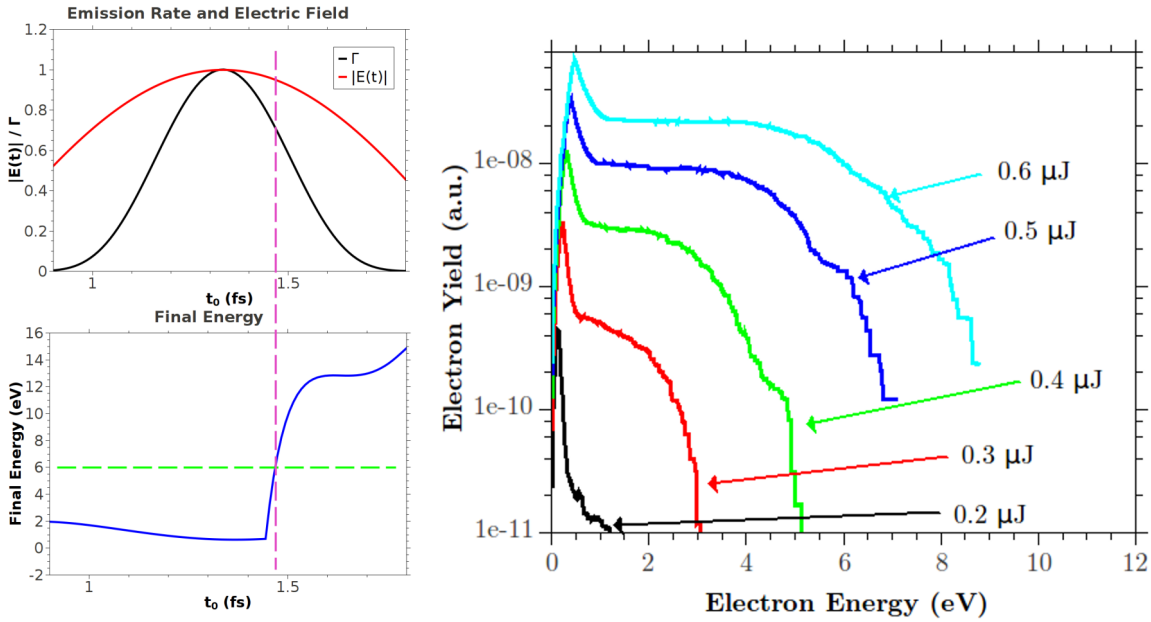

Figure 5-4: Calculation of energy spectra. The left panel shows how the simpleman procedure works. The top left plot shows the FN emission rate as a function of time (black curve) alongside the electric field (red curve). Notice that the emission window is much shorter than a full cycle in this example. The lower left plot shows the final energy values after calculating the electron trajectories in the dipolar field as a function of birth time. The dashed curves show how the weight value is found (magenta, vertical dashed line) for each final energy value (green, horizontal dashed line). For a long pulse, there would be many intersections to include for each energy value. The right plot shows compiled spectra for a Si tip ($\chi_{Si} = 4.05eV$) using a 35 fs pulse centered at 800 nm with a beam waist of 80 μm for various pulse energies. An enhancement factor of 12 was used in the calculation, and the rescattering probability was taken to be ~ 0.3. Finally, the tip radius of curvature was taken to be $\beta = 7.5$ nm.

Si, and the field enhancement to be $\xi = 10.5$. As expected, for the Homogeneous case the cutoff scaling approaches 10Up at the highest field strengths, however the modeled and dipolar field profiles are significantly less. This is explained by an increased electron excursion as field strength increases, in which case the electron escapes the field before it can gain more ponderomotive energy.

5.2.3 Comparison with Quantum Spectral Calculations

In this section the Simpleman model for the case of an homogenous electric field (i.e. fully within the dipole approximation) is compared to the second order perturbation theory calculation of the electron spectra for the case of a step potential.

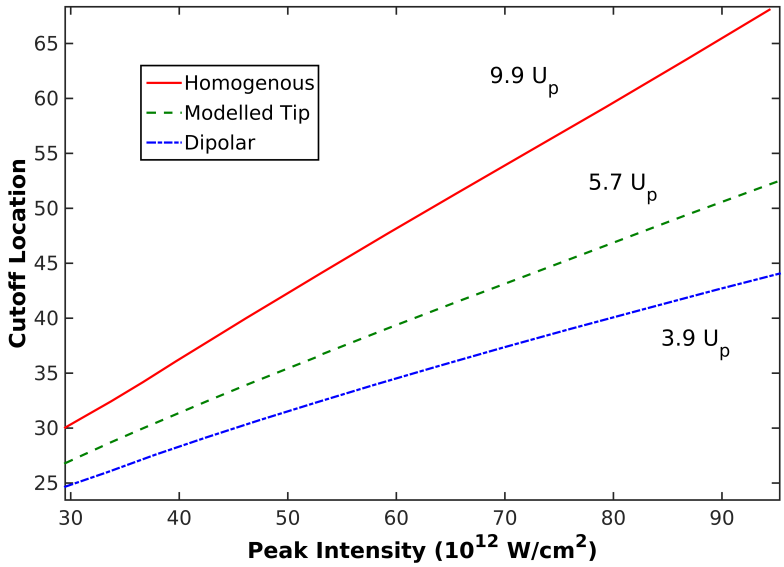

Figure 5-5: Cutoff scaling of the rescattered electrons as a function of input intensity for a homogeneous field profile (solid red curve), a modeled profile from a Si tip having a 5 nm radius of curvature (dashed green curve), and a dipolar field profile with $\beta = 5$ nm (dash-dot blue curve). In each case the Fowler-Nordheim rate and tunnel exit calculation from Si was used, and the field enhancement was taken to be $\xi = 10.5$.

This serves to demonstrate key similarities and differences between the classical model and one which incorporates more quantum effects. To start, the second order SF perturbation theory calculation must be described.

Recall that the full expresssion for the expansion of $M_{\mathbf{p}}$ up to the second order is shown in Equations (2.17-2.19). The calculation of $M_{\mathbf{p}}^{(1)}$ is rather straightforward, but the that of $M_{\mathbf{p}}^{(2)}$ would require significant computational resources, even for very short pulses. However, it can be greatly simplified with just a few approximations. First, we assume a one dimensional problem. As before, this is a direct analog to the 3D solution for the case of a large area tip (to within a constant pre-factor), where the transverse momentum is conserved from the ground state distribution (again see Appendix B for an explanation). Second, the rescattering matrix element is approximated by using a low-frequency approximation. Finally, the innermost integral over k is approximated using the saddle point method. This reduces the problem to a summation of two integrals, where the number of terms

in the summation depends on the number of saddle points.

The first and third approximations are rather straightforward, but the second requires a more in-depth discussion. We start by rearranging the integral expression of $M_{\mathbf{p}}$ as follows

$$M_p^{(2)} = \frac{-1}{\hbar^2}\int_{-\infty}^{\infty} d\tau q F(\tau) e^{iW_0\tau/\hbar}\frac{1}{\hbar}\int_{-\infty}^{\infty} dk d_{(k+qA(\tau))}\exp\{iS_k(\tau)/\hbar\} \times \int_{\tau}^{\infty} d\tau' \exp\{i[S_p(\tau') - S_k(\tau')]/\hbar\}\left\langle p + qA(\tau')\right| V \left|k + qA(\tau')\right\rangle, \tag{5.10}$$

where we have already switched to the convention of a one-dimensional calculation where k and p are simply scalars. When written this way, it is clear that the final matrix element is simply that for rescattering in the context of the first Born approximation (see [34]). The difficulty of this integral is that it requires knowledge of the state inside of the step potential. However, this is not trivial, as inside of the step boundary the laser field is weak. If the interaction takes place only near the step-down boundary, and a long-wavelength driver is being used, we can assume that the incoming wave looks sufficiently like a plane wave with instantaneous momentum $k' = k + qA(\tau')$. For a plane wave incident on the step-down boundary representing the emitter, the scattering matrix element is simply

$$\gamma = -T\left\langle p'\right| U \left|k'\right\rangle, \tag{5.11}$$

where $p' = p + qA(\tau')$, and U is the potential barrier height. The transmission coefficient T then represents the transmission through a step down potential for an incoming momentum k', which is

$$T = \begin{cases} \frac{2k'}{2k'+\Delta}, & \text{if } k' < 0 \\ 0, & \text{otherwise} \end{cases} \tag{5.12}$$

where the Δ is the extra momentum needed for energy conservation upon trans-

mission, and is found to be

$$\Delta = \left(k'^2 + 2mU\right)^{1/2} - k'. \tag{5.13}$$

Carrying this out yields

$$\begin{aligned}\gamma &= -UT\int_{-\infty}^{0} dz e^{i(k'+\Delta-p')z/\hbar} \\ &= \begin{cases} \frac{2iUk'\hbar}{(2k'+\Delta)(k-p+\Delta)}, & \text{if } k' < 0 \\ 0, & \text{otherwise} \end{cases}\end{aligned} \tag{5.14}$$

where we have made use of the fact that $k' - p' = k - p$. The integral is only taken over the negative half-space in z as the potential is identically zero elsewhere. This expression can now replace the rescattering matrix element in Equation (5.10), which yields

$$\begin{aligned}M_p^{(2)} = \frac{-1}{\hbar^2}\int_{-\infty}^{\infty} d\tau q F(\tau) e^{iW_0\tau/\hbar}\frac{1}{\hbar}\int_{-\infty}^{\infty} dk d_{(k+qA(\tau))}\exp\{iS_k(\tau)/\hbar\} \\ \times\int_{\tau}^{\infty} d\tau' \exp\{i[S_p(\tau') - S_k(\tau')]/\hbar\}\gamma(k,p,\tau').\end{aligned} \tag{5.15}$$

The saddle point approximation is only applied across the integral over k. This has already been discussed briefly in Section 2.2.2. We can then separate out only the integral over k from Equation (5.15). This yields

$$\Gamma = \int_{-\infty}^{\infty} dk d_{(k+qA(\tau))}\gamma(k,p,\tau')\exp\{i[S_k(\tau) - S_k(\tau')]/\hbar\}. \tag{5.16}$$

In the context of the saddle point approximation, the saddle points are at $k_s(\tau,\tau')$, where we have

$$k_s(\tau,\tau') = \frac{q}{\hbar(\tau-\tau')}\int_{\tau}^{\tau'} dt A(t). \tag{5.17}$$

This implies only those trajectories where a classical electron would return to the surface are included in the calculation. Trajectories that do not satisfy this constraint are not included. Furthermore, we assume that k_s must be negative (i.e.

approaching the surface) at the scattering time τ', or else we also discard it. Using this result we find that

$$\Gamma \approx \sqrt{\frac{2\pi i m}{\hbar(\tau-\tau')}}\, d_{(k_s+qA(\tau))}\gamma(k_s,p,\tau')\exp\{i[S_{k_s}(\tau)-S_{k_s}(\tau')]/\hbar\}, \tag{5.18}$$

reducing the integral over all k to a functional expression of only τ and τ'.

With this, the computational requirements have been reduced sufficiently to make the computation of $M_p^{(2)}$ possible within a reasonable amount of time. The author has found that with proper parallelized computation, the entire amplitude up to the second order can be calculated with 0.1 eV resolution up to 100 eV within minutes for input pulses being tens of fs in duration. This calculation has also been used to verify that while an accurate calculation of the spectrum requires one to determine $M_p^{(2)}$, it makes a negligible impact on the total yield calculation. This has been described at length in [28]. The bulk of the electron emission is described by the direct electrons, i.e. those represented by $M_p^{(1)}$. While some electrons may interact with the surface potential and rescatter, as described by $M_p^{(2)}$, these are few in number and are still largely emitted as detectable electrons. Thus, $M_p^{(2)}$ does not epresent "new" electrons as such, but only a "correction factor" to the direct electrons to accommodate for the few that are emitted but then scatter from the boundary. Thus, $M_p^{(2)}$ is used to model experimental studies of electron spectra, but not for experimental studies of total electron yield.

We can now compare the quantum rescattering model using the modified SF perturbation theory approach described above to the Simpleman approach. Figure 5-6 compares both models for the case of a Si structure, where we assume all of the electrons are emitted from a ground state located just near the conduction band, i.e. $W_0 = \chi_{Si} = 4.05\,\text{eV}$. The incident pulse is centered around 1000 nm with a pulse duration of 8 fs. As expected, the quantum calculation has the characteristic energy peaks having a separation of $\hbar\omega \approx 1.24$ eV, while the Simpleman approach shows a smooth spectrum as it is a purely classical calculation. Both show an intense low energy peak from electrons that are directly emitted, with

an extended plateau due to rescattering from the step boundary and subsequent ponderamotive acceleration. In both spectra the plateau extends to roughly 13 eV before beginning to fall off. However, while the classical calculation shows a very steep cutoff, the quantum calculation shows a much more gradual decay in the spectrum as there is a quantum energy spread not accounted for in the classical model.

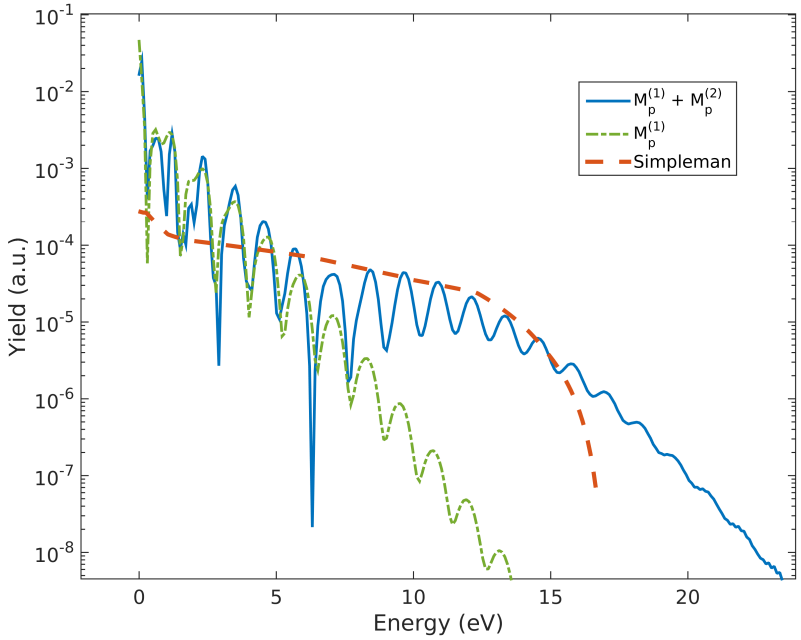

Figure 5-6: Comparison of spectra using the Simpleman model (red dashed) and second order SF perturbation theory. Notice that the cutoff of the plateau region in each spectra starts at roughly the same energy (around 15 eV). While the classical analysis predicts a steep cutoff as there is a hard energy limit, the quantum analysis shows a much more gradual decay in energy spectrum. The direct component, $M_p^{(1)}$, is also shown (green dash-dot).

With such short pulses, we can also expect a CEP dependence of the outgoing energy spectrum. The results of such an analysis are shown in Figures 5-7 and 5-8 for the Simpleman and quantum models respectively. In each plot, bounds were placed on the colorscale to highlight the behavior of the spectra just near the spectral cutoff. The modulation of the cutoff point is seen to match in phase between the two models, however the quantum model shows a more interesting interference behavior that cannot be observed in the classical calculation. As the CEP is

changed, the emission is dominated by one half cycle at certain delays, and by two at others. This leads to a characteristic change in the modulation depth of the electron spectra. Similar results have been characterized experimentally with short pulses and single-tip emitters in tungsten [15]. This behavior is better observed in the full pseudocolor plot of the quantum model results, where no bounds are used on the colorscale, as shown in Figure 5-9. Furthermore, the effect of cutoff energy modulation, as seen more clearly in the Simpleman calculation, has also been experimentally observed from a single gold tip [10].

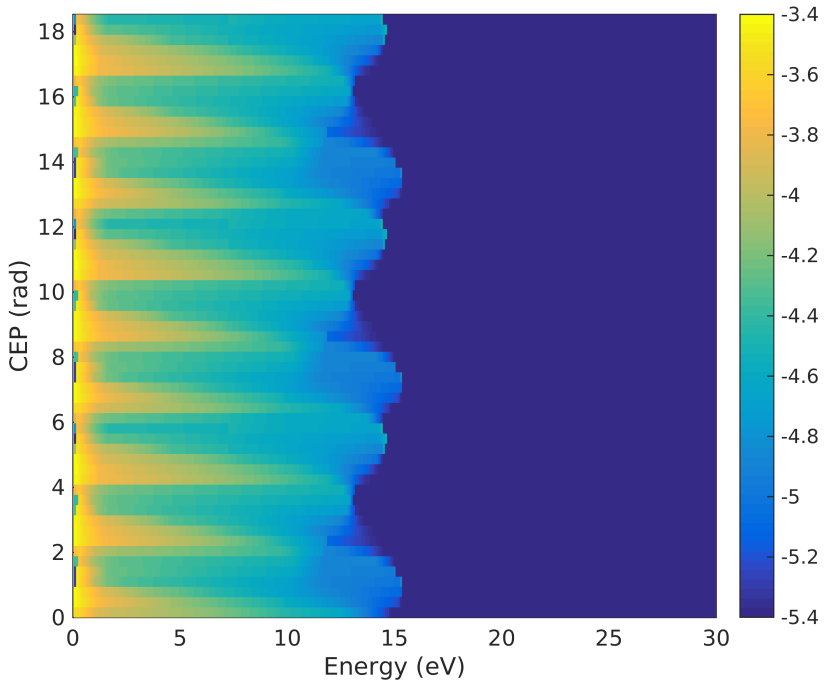

Figure 5-7: Pseudocolor plot of simulated spectra using the Simpleman model. The colorscale represents $\log_{10}$ of the yield. The simulation assumed a step function corresponding to $\chi_{Si} = 4.05\,\text{eV}$ with a ground state distribution peaked just above the conduction band. A reflection coefficient of $R = 0.3$ was used to simulate electron rescattering from the boundary. Bounds were placed on the color scale to focus on the behavior of the cutoff region of the spectrum.

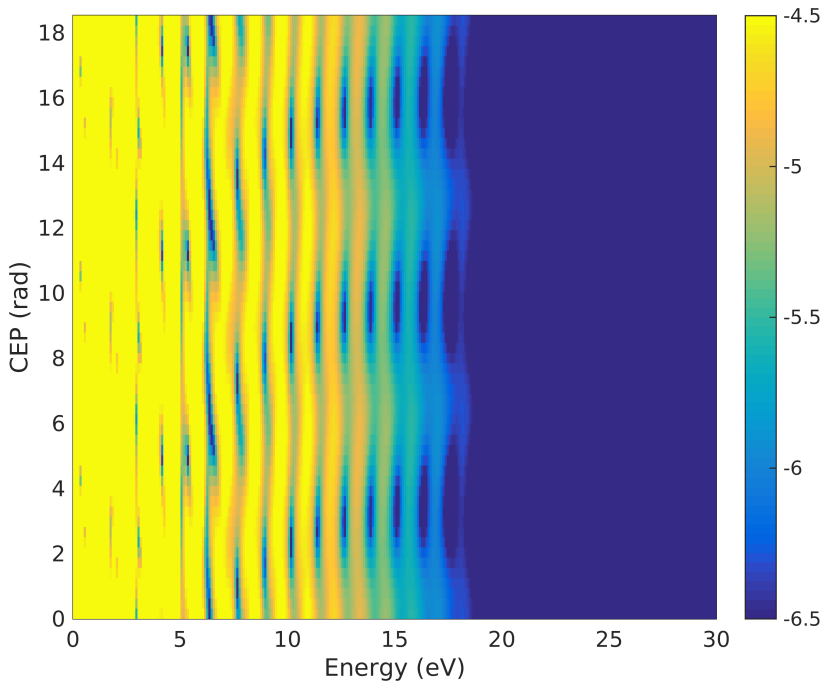

Figure 5-8: Pseudocolor plot of simulated spectra using second order perturbation theory. The colorscale represents $\log_{10}$ of the yield. The simulation assumed a step function corresponding to $\chi_{Si} = 4.05$ eV with a ground state distribution peaked just above the conduction band. Bounds were placed on the color scale to focus on the behavior of the cutoff region of the spectrum.

5.3 Experimental Results

This section highlights results obtained from nanostructured cathodes in Si. While other cathode materials, such as Au and W, have been investigated for strong-field emission [12, 15, 16], Si offers several key advantages. First, there exist well understood processes for producing repeatable, high-throughput nanostrucuted surfaces in Si thanks to the electronics industry. While W has a high melting point (3422° C), and subsequently high damage threshold, it has been observed that it can be rather sensitive to vacuum and environmental conditions, and the properties of the tip can change over time necessitating an extra anneal step [15]. By contrast, our own experimental observations have indicated that Si is rather robust in high vacuum conditions ($\approx 1 \times 10^{-7}$ Torr) readily achievable with a turbomolecular pump, with no apparent degradation of performance over tens of hours of

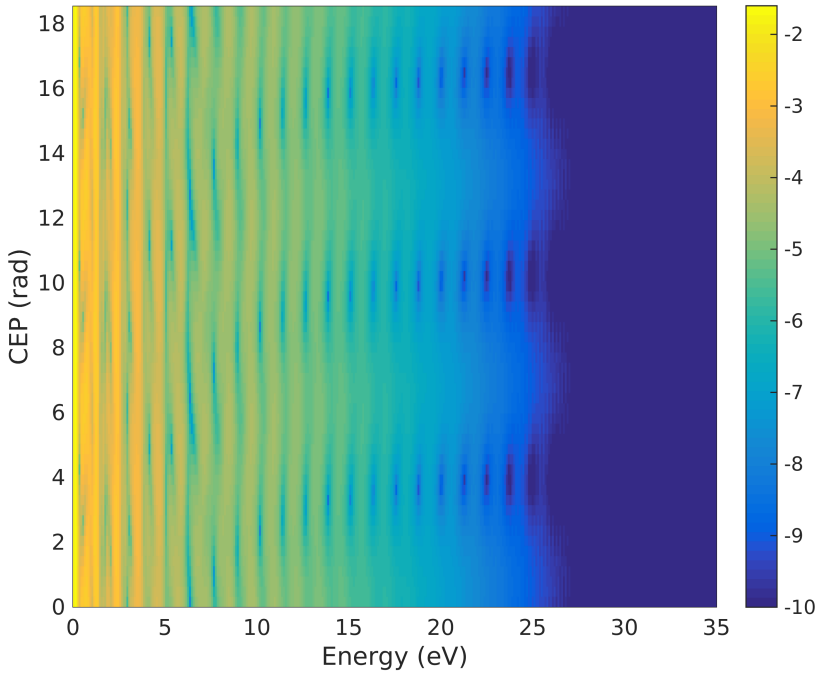

Figure 5-9: Psuedocolor plot of the full intensity range for the case of the second order perturbation theory calculation. Notice how at the highest energies, for certain CEP values the spectrom is completely smooth. This indicates only a single pulse in time contributes to this spectral region.

use. While Au is also robust to vacuum conditions, being rather non-reactive, it has a relatively low melting point (1064° C compared to 1414° C for Si), and tends to change shape and pool when irradiated with high-energy, femtosecond laser pulses [62].

In the following subsections, a complete experimental characterization of electron emission from nanostructured pillars of Si driven by long-wavelength optical sources ($\geqslant$ 800 nm) is presented. These structures were fabricated from n-Si ($\approx$ 5 Ω-cm) wafers. Concentric disks of silicon nitride and silicon dioxide were patterned on the surface using projection lithography. A dry etch process formed the tips under the oxide/nitride disks. The pillars were then formed by deep reactive-ion etching. A thermal oxidation step sharpened the tip to its final form and narrowed the pillars. Tips were formed with radii of curvatured (ROC) down to 5 nm. For a more thorough discussion of the fabrication process, the reader is

referred to [63].

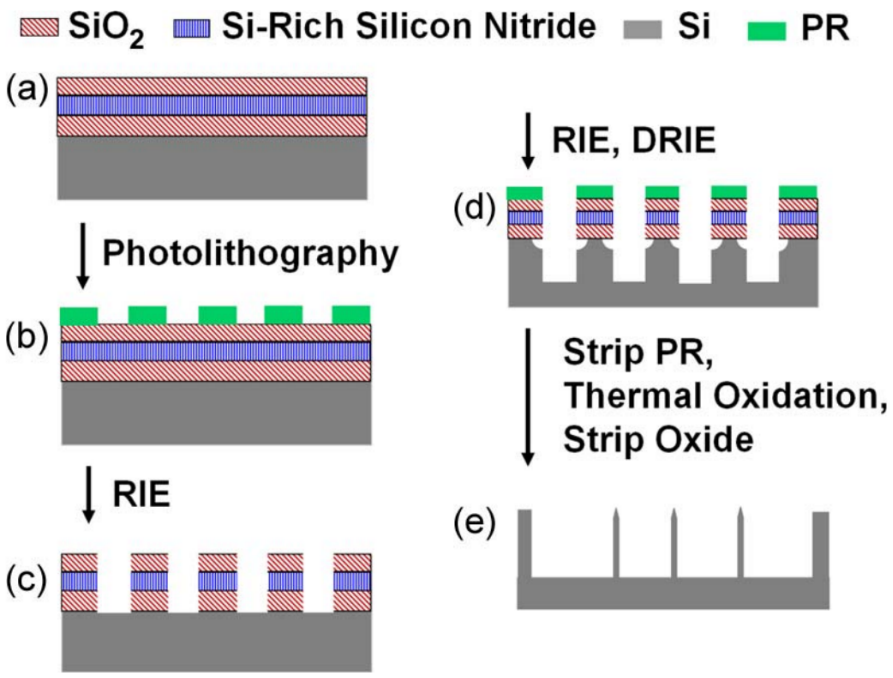

Figure 5-10: The process flow for fabricating the nanosharp silicon pillars. (a) Layers of SiO_2 are formed on the surface of n-Si. (b) Photoresist (PR) is then deposited on the surface and patterned using projection lithography. (c) An etch processes create disks of the oxide/nitride layers, and (d) a dry-etch process forms a tip structure under the disks. (e) The PR/disks are then removed, followed by thermal oxidation and subsequent oxide removal for final shaping of the tips and thinning of the pillars. Image taken from [63].

5.3.1 Enhanced Multiphoton Emission

Finite element modeling of the electric fields surrounding the tip show an approximate field enhancement of roughly $10\times$ compared to the incident field for pulses centered at 800 nm at a grazing incidence of 84° polarized along the tip axis. Unlike plasmonic resonators, the field enhancment is due to a lightning-rod effect, where charges are displaced from the tip shaft and driven into the tip apex. As such, there is no phase retardation between the incident and enhanced field on the surface, as would be typical for a resonant structure. The most profound impact of this enhancement can be observed by comparing total electron yield from a planar surface of silicon and the nanostructured surface for the same incident pulse.

With an incident pulse energy of 5 μJ centered at 800 nm having a focal spot size of 90 μm FWHM at a repetition rate of 3 kHz and a grazing incidence angle of 86°, there was a gain of three orders of magnitude from the structured cathode having tips spaced on a 5 μm pitch as opposed to a planar cathode under the same conditions (1 fC total charge yield per pulse versus 1 pC).

It is important to bear in mind that this increased efficiency is observed despite the fact that the overall active area is significantly reduced. This is because much of the space is shadowed by the high aspect ratio tips (note that each tip has a height of roughly 40 μm). Considering a tip pillar diameter of 900 nm, a rough estimate shows that the total illuminated surface area is in fact reduced by more than an order of magnitude relative to a planar cathode at a grazing incidence angle of 86°. This was experimentally confirmed by using an extreme ultraviolet (EUV) source to drive the photocathode. Since there is not a significant field enhancement at EUV wavelengths near the tip, and the emission is driven mostly by one-photon absorption inside of the bulk of the material, one expects a decrease in photoemitted electrons with a decrease in exposed surface area. It was experimentally confirmed that for an EUV source, the total current yield was reduced by more than a factor of 2 when incident on the structured portion of the cathode as opposed to a planar region. A likely reason the yield was not further decreased as our simple analysis of surface area would suggest is the incident angle on the material surfaces. The absorption coefficient increases at lower incident angles, thus increasing the absorption cross section on the sidewalls of the tip structures.

5.3.2 Intensity Scaling

While the increase in overall efficiency is a strong indicator of the enhanced field on the surface leading to an enhanced multiphoton emission from the cathode, a careful study of how the charge yield scales with incident pulse energy/intensity can yield much more information about the underlying physical process at play. Using the same pulse form and incident geometry as described above, the energy

was scaled from tens of nJ to almost 10 μJ while collecting all of the emitted current into a metal anode. Furthermore, this scaling was repeated at various bias voltages to study any potential space charge effects due to the emitted charge bunch interacting with the image charge on the cathode surface. To better understand the physical layout of the experiment, a schematic is shown in Figure 5-11, and an image of the sample-holder arrangement in front of the TOF spectrometer is shown in Figure 5-12.

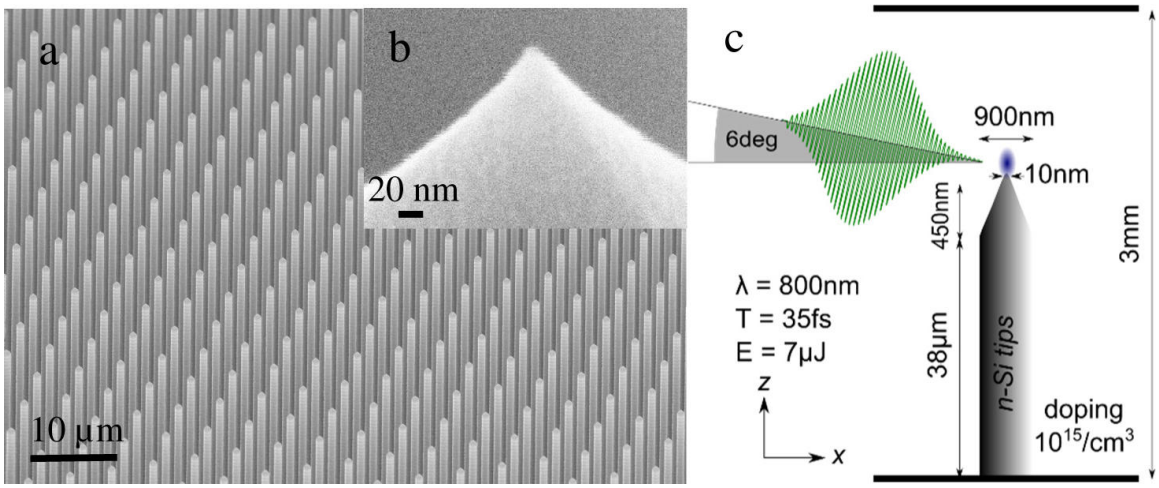

Figure 5-11: Scanning electron microscope images of the structured cathode (a) and tip apex (b). In (c), a schematic of the experimental arrangement is drawn. The incoming pulse is at a grazing incidence. The tip substrate and metal anode are separated by a gap of roughly 3 mm. A bias is applied between the cathode and anode to sweep the electrons off of the surface. By adjusting the bias, effects from any space-charge induced virtual cathode are studied. The numbers in the plot indicate typical experimental parameters for reference.

All of the data is compiled in Figure 5-13, and an inset shows the calculated quantum efficiency QE as a function of incident energy, calculated simply as the number of electrons per photon. Due to the nonlinear nature of the emission process, the QE is a function of incident intensity. While the quantum efficiency peaks at a value just less than 1×10^{-6}, remember that much of the cathode is not utilized. It is predicted that the QE could be further increased by nearly an order of magnitude by further reducing the tip spacing.

For each bias setting, the current yield has a distinct kink at the same input pulse energy. If this kink were due to a virtual cathode, one would expect it to

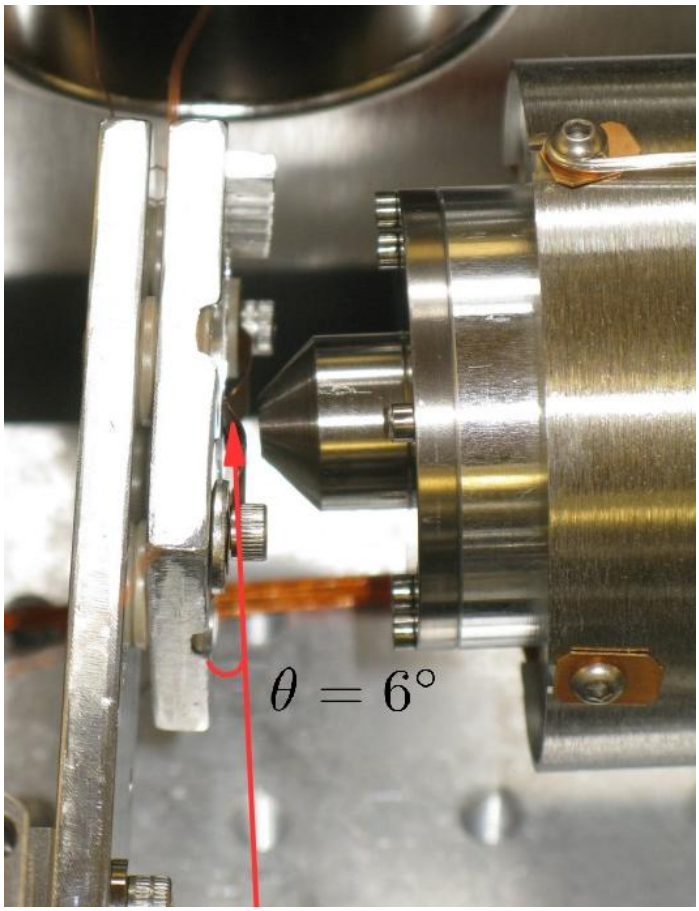

Figure 5-12: Image of sample-holder arrangement in front of the TOF spectrometer orifice. The red arrow indicates the laser path.

shift right and vertically with increased bias. This means that is not related to a space-charge saturation often observed in metallic photocathodes [29]. Thus, we can safely assume that the kink arises from a physical mechanism. Assuming that the emission is dominated by the SF emission at the tip surface, we compare the experimental intensity scaling to the SF perturbation model discussed in Section 5.2.1.

To account for the spatial profile of the incoming beam, we discretized a Gaussian intensity profile along a rectangular grid on the emitter surface, and find the total charge yield across all of the grid spaces. The pulse was taken to be Gaussian in time with a FWHM of 35 fs. Due to the spatial and temporal averaging, the steep channel closings, similar to those found in Figure 5-2, are smoothed over, leaving only a small dip near the first channel closing for the transition from 3- to

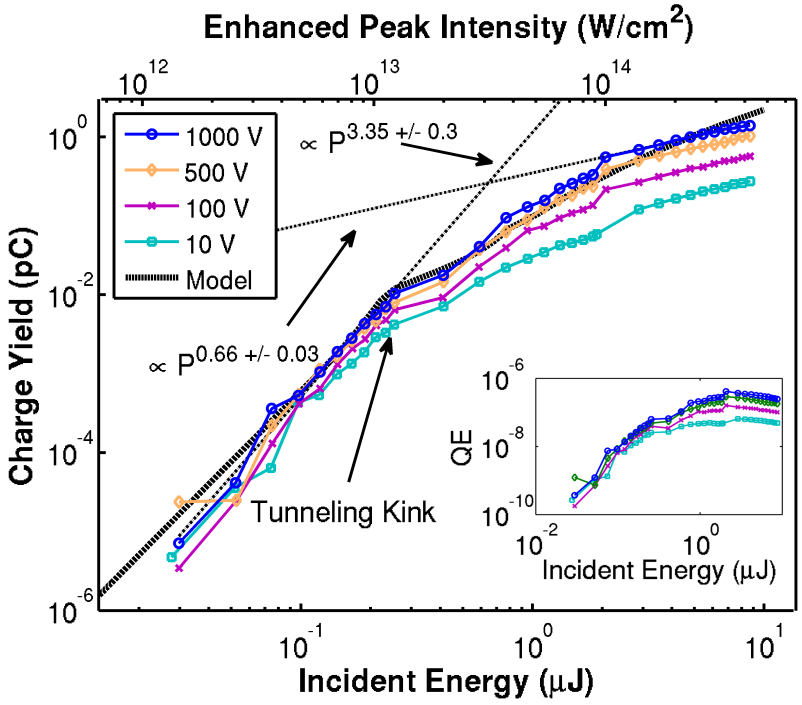

Figure 5-13: Intensity scaling of total charge yield versus incident pulse energy for bias values of 10 V, 100 V, 500 V, and 1000 V respectively. The top x-axis is labeled in terms of an enhanced peak intensity at the tip, which is calculated by matching the kink location with that expected from the SF perturbation model, which is shown in the plot as the black, dashed line. It is matched against the highest bias of 1000 V to ensure any virtual cathode effects have been reduced. The quantum efficiency calculation is shown in the inset. Due to the multiphoton process, the quantum efficiency depends on the input intensity.

4- photon emission. This leaves only a fit of the pre-factor that accounts for the tip area, and field enhancement at the tip surface, which shift the simulated curve in the vertical and horizontal direction respectively. This curve is then matched against the intensity scaling at a 1000 V bias as we want to reduce the effect of any space-charge induced virtual cathode.

The modeled curve (dashed, black line in Figure 5-13), matches almost perfectly with the experimental data. The field enhancement factor needed to achieve the best matching to the experimental data was found to be 10.5×, which agress very well with the simulated enhancement factor of 9.4× at 800 nm. To give a clearer look at how well the modeled yield fits the experimental data at a 1000 V bias, this case is isolated in Figure 5-14. Even the unique dip in yield near the first channel

closing is observed in the experimental data, giving a high degree of confidence that the structured cathode is being driven into the optical tunneling regime of photoemission.

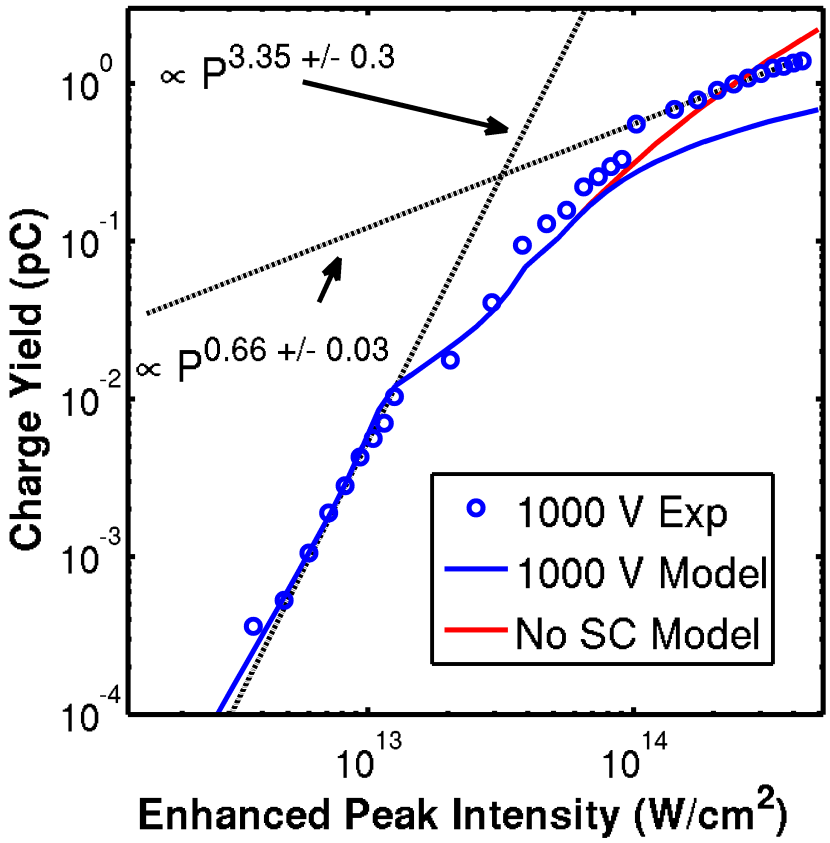

Figure 5-14: Intensity scaling of the experimental results at a 1000 V bias compared to the modeled result, including (solid, blue) and excluding (solid, red) any virtual cathode effects.

We cannot totally rule out the effect of a virtual cathode, as there is clearly some change in total yield with increasing bias at the highest incident pulse energies. A virtual cathode is essentially the formation of separated sheets of charge due to the emitted charge bunch and corresponding image charge within the cathode substrate. For thermal and DC field emitters, the electrons are emitted from the substrate continuously, leading to a long channel of charge. In this regime, the Child-Langmuir current limit describes space-charge limited emission. However, ultrafast photocathodes emit charge over a very short window of time leading to

a dense "sheet" of charge. In this limit, one can estimate that space-charge limited current should occur when the field between the sheet of emitted charge and the cathode surface is equal to that of the DC bias. In this scenario, electrons in the trailing edge of the bunch are pushed back to the cathode surface and reabsorbed rather than emitted. The amount of charge where this limit is reached is referred to as the critical charge, Q_C

$$Q_C = \frac{V A_Q \epsilon_0}{d}, \tag{5.19}$$

where V is the bias voltage, A_Q is the area of the charge sheet, ϵ_0 is the permittivity of free space, and d is the anode to cathode spacing. To account for the fact that the charge is not emitted uniformly over the cathode surface due to the spatial profile of the beam, this critical charge is calculated for each rectangular grid section used for spatial averaging by simply replacing A_Q with the grid area to find $Q_{C,\,grid}$. During the calculation of the spatial emission profile, the charge emitted from each grid area is then limited to $Q_{C,\,grid}$.

This calculation makes some basic assumptions. First, it ignores any DC field enhancement or variation around the tip structures. This is justified as field modeling shows that enhanced DC fields decay to a value expected for a planar cathode within tens of nm of the tip apex making them negligible during the electron transit to the anode. Furthermore, particle-in-cell simulations indicate that within 1 ps after emission [11] the electrons spread from the tip to a radius the size of the lattice constant. Since it takes more than 1 ns for the electrons to reach the anode, the spatial structure of the electron cloud can be safely ignored. Finally, the model does not account for further spreading of the electron cloud beyond the size of the initial beam spot. This means that the critical charge calculation underestimates what should be experimentally observed, consistent with the modeled current accounting for space-charge in Figure 5-14, as laser acceleration causes a significant transverse energy spread away from the tip apex.

Using the same parameters for fitting the model results to the 1000 V bias curve, the space-charge limited current was calculated for all bias levels using $Q_{C,grid}$,

and the results are compiled in Figure 5-15. In each case, the virtual cathode limit used provides an underestimate of the measured current for the same bias. For instance, at a bias of 1000 V, the final slope predicted with space-charge included is 0.51, however the measured slope of 0.66 falls somewhere between 0.51 and 1.2, the modeled slope with no space-charge included. This is likely a result of ignoring the transverse and longitudinal momentum spread of the bunch as discussed above. Nonetheless, the calculations clearly match the experimentally observed trend. At low yields, the intensity scaling profiles overlap, while at higher yields each saturate to different levels depending on Q_C, which increases with the applied bias voltage. Thus, when total yield is a critical issue, especially for cathodes with tighter tip spacing, an increased DC and/or low frequency bias is necessary to ensure a full collection of current from the cathode.

5.3.3 Energy Spectra

While SF perturbation theory combined with a simple virtual cathode simulation provides an explanation of the total emission yield curve, more information about the emission process and subsequent interaction with the driving laser pulse can be gathered through analysis of the emitted electron spectra. As discussed in Sections 5.2.2 and 5.2.3, the energy spectrum should consist of two main components for SF emission: the low energy, direct peak, and the high energy plateau due to rescattering from the tip surface. Classically speaking, an electron born within a laser field alone can at most be accelerated to an energy of 2Up. However, with the inclusion of a rescattering boundary, the plateau cutoff energy [27, 64] can exceed 10Up.

Using the same 800 nm pulsed source and emitter geometry for measuring the intensity scaling with a 10 V bias, the anode was replaced with a time of flight electron spectrometer, and the electron energy spectra were collected from the tips for a range of laser pulse energies. The results of this scan are shown in Figure 5-16.

The results of this scan show a sharp ($<$ 1.5 eV FWHM peak width) low-energy

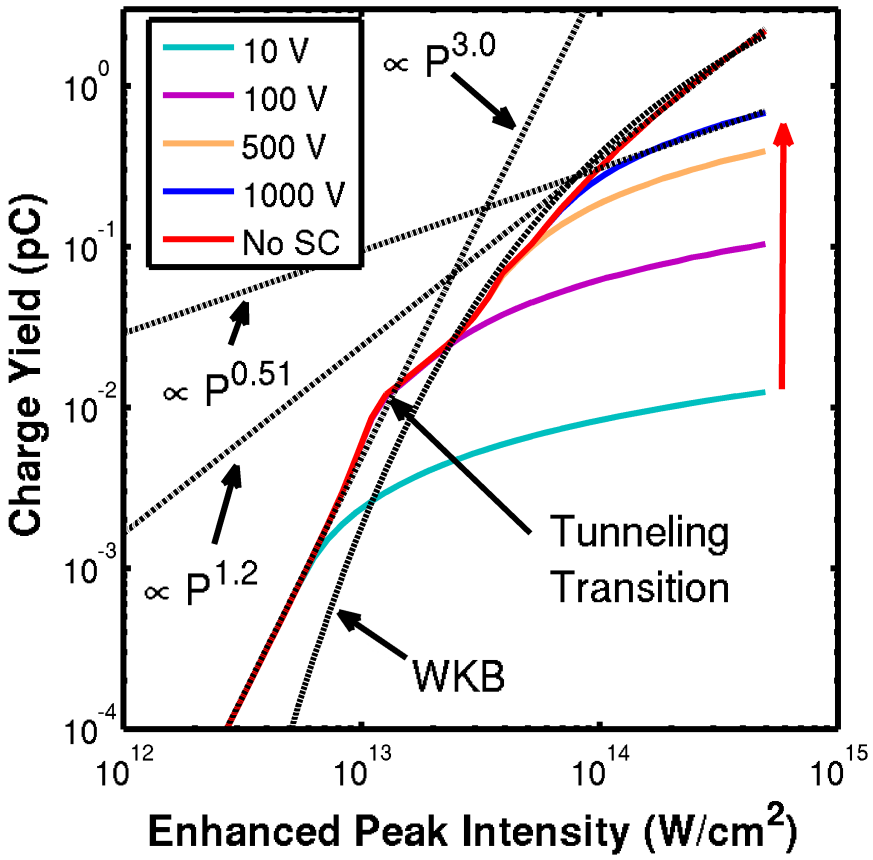

Figure 5-15: Modeled current scaling for a Gaussian pulse having a diameter of 90 μm FWHM and temporal duration of 35 fs FWHM on a Si surface accounting for virtual cathode induced saturation of the current yield. Each curve represents a different bias setting, from 10 V to 1000 V, each saturating at higher and higher charge yield levels. The topmost curve (red) represents the case of no space charge, and is the same as the black dashed curve in Figure 5-13. For visual comparison, the spatially averaged WKB tunneling rate is also shown along with key slope references, including: initial 3-photon absorption slope, final slope including space-charge with 1000 V bias, and final slope without space-charge.

peak with a high-energy plateau extending to around 12 eV beyond the low-energy peak at the highest pulse energy tested. To ensure the high-energy plateau is indeed due to laser acceleration after emission, space-charge broadening must be ruled out. Particle in cell modeling of a single Si tip [11] shows that pulse spreading indeed occurs with the inclusion of space-charge; however the high-energy plateau was still dominated by laser accelerated electrons for charge yields exceeding 1 pC, while the yield in the spectral measurements shown in Figure 5-16 did not exceed 50 fC. While this rules out such effects in the single-tip limit, the

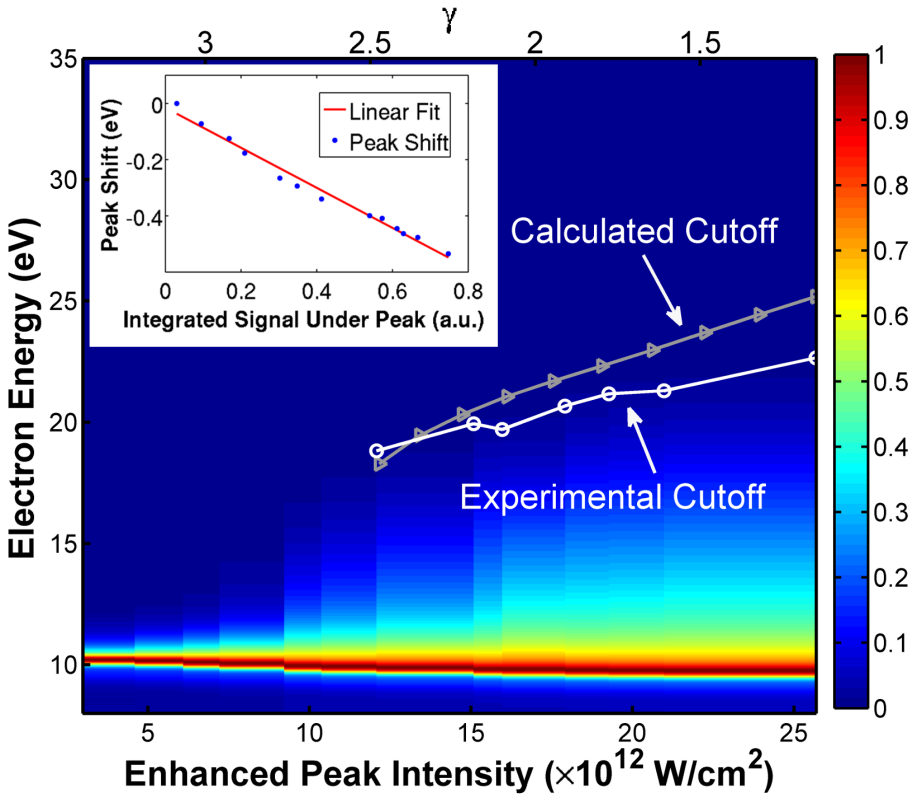

Figure 5-16: Intensity scaling study of energy spectra. The psuedocolor plot shows all collected spectra as a function of enhanced peak intensity. For reference, the top x-axis shows the calculated Keldysh parameter. The overlayed plots show the calculated (grey triangles) and experimentally measured (white circles) cutoff values. The inset show the central energy of the direct electron peak as a function of integrated electron signal in the peak alone. It demonstrates a linear dependence with the charge in the peak as one would expect for an image-charge induced deceleration of the electron bunch.

substrate and neighboring charges may also influence the spectra.

Femtosecond electron pulse spreading from a planar cathode due to electron-electron interactions has been shown both theoretically and experimentally to scale as the square root of the number of particles in the electron bunch and be inversely proportional to the electron bunch radius [65, 66]. Passlack et al. [65] experimentally demonstrated that for an electron pulse with a group velocity corresponding to 0.18 eV, the pulse broadening did not exceed 300 meV for more than 75000 electrons per pulse and an initial bunch radius of 350 μm. Accounting for the differences in initial bunch radius based on the beam profile used, even a conservative estimate does not indicate broadening the electron pulse by more than 2 eV at the

highest yield measured.

To determine the predicted plateau cutoff extension described by laser acceleration, the Simpleman model was used. The enhanced peak intensity was calibrated by matching the current scaling measured at the spectrometer to the measurements in Figure 5-13. The details of the calculation are outlined in Section 5.2.2, where we have replaced the dipolar decay function describing the electric field profile with the simulated profile from finite element based electromagnetic simulations [11]. As the Simpleman model only applies to the tunneling regime of emission, care was taken to only compare the predicted and measured cutoff values beyond the kink observed in the emission curve. For reference, the value of the Keldysh parameter, γ, is also provided in the top x-axis of Figure 5-16.

To account for the 10 V DC bias in the simulation, the Simpleman solution is shifted by 10 eV. Space charge is neglected in this calculation, following the previous discussion. The cutoff value was again defined in the same way as in Section 5.2.2, being the energy where $P(W) = 0.1P(W/2)$ is satisfied. The results are overlaid with the energy spectra in Figure 5-16 and compared to the measured cutoff values using the same condition. The calculated cutoff values are offset to slightly higher energies, with a slightly increased slope relative to the measured values. Overall, the agreement between the measured and the predicted cutoff values is reassuring given that the peak intensity was calibrated using the kink in current yield, an entirely separate measurement, rather than as a free parameter to achieve the best fit.

The absolute value of the cutoff using this method is sensitive to the exact spectral shape. Since the semiclassical model results in spectra having much steeper cutoff than those observed experimentally, it is difficult to find an absolute match between calculated and measured values. However, the difference in slope is more interesting as this points to a deviation between the modeled and actual field decay away from the tip apex. The calculations here already show a reduced slope for the modeled field decay as compared to the case of a homogeneous electric field due to the fact that the electron excursion starts to be on the order of the field decay

length, resulting in a minimum adiabaticity parameter [13] $\delta \approx 15$. While not deep into the subcycle regime where the adiabaticity parameter is much less than 1 and the cutoff scales linearly with the field [13], the overall reduction in cutoff energy can be quite severe much before this regime is reached (Figure 5-5).

Laser-induced cutoff scaling also indicates that the emission process is prompt with respect to the driving electric field, as the laser can only accelerate electrons that are present within the duration of the laser pulse itself. Preliminary cross correlation electron emission measurements using two-color pulses further demonstrate the prompt nature of the electron emission and laser-induced spectral shaping (Section 5.3.4). Such results indicate the possibility of tailoring laser waveforms to engineer emitted electron spectra.

Another feature that stands out from the electron spectra is the slight loss in energy of the main spectral peak as the intensity is increased. If the effect is solely due to changing ponderomotive potential, then the shift should vary linearly with peak intensity, which was not found to be the case. The single tip model at the beginning of the paper indicates that image charge effects from the tip alone can contribute significantly to electron deceleration and recombination with the tip surface at pC level yields across the entire array. In recent years, observations of peak shifts in photoemission due to image-charge effects have been studied in detail across a variety of emission levels [67,68]. Zhou et al. [67] show experimentally and theoretically that the image charge-related shift from a planar conductive sample is due mostly to the amount of charge in the bunch, and shifts the mean energy linearly with respect to the total number of electrons in the bunch. A simple analysis shows that the main spectral peak indeed shifts linearly to lower energies with respect to the number of charges in the peak, but not the total charge (Figure 5-16 inset). This interpretation is also consistent with the idea that the fast moving electrons quickly escape the low-energy bunch after laser acceleration, and contribute minimally to the peak shift.

While the quantum model more correctly describes a slow roll-off of the spectrum near the cutoff as compared to the Simpleman model, the predicted harmonic

peaks are missing from all of the experimentally measured spectra. This is thought to be due to dephasing effects of the emitter, as well as spectral averaging effects that result from the ground state distribution, thermal effects, and intensity averaging around the tip apex. This is consistent with many other experimental results from single tips. Only one group has consistently observed harmonic peaks from tips of tungsten [14, 15], however in their experiments only single tips are measured and the incident pulses are significantly shorter (only 6 fs FWHM) which may contribute to the increase contrast in the harmonic structure if dephasing is a critical issue. Nonetheless, the contrast they observe is still less than theory would predict.

5.3.4 Two-Color Cross-Correlation

To further ensure that the emission mechanism measured is prompt with the laser field, and that the extended energy plateau is indeed a strong-field acceleration affect and not due to space-charge accumulation, two-color measurements were performed on the tip structures. For this a 2 μm laser system based on optical parametric chirped pulse amplification of a broadband seed generated by intrapulse difference frequency generation of a titanium sapphire oscillator [69] was used to generate pulses at a 1 kHz repetition rate. The pulses are broadband, having a bandwidth extending from ~ 1800-2450 nm, compressed to within 10% of their Fourier limit of 20 fs. A portion of the available pulse energy was frequency doubled in a 0.5 mm thick BBO crystal, to generate an additional pulse extending from ~ 980-1200 nm with a Fourier limited duration of 25 fs. Both pulses were combined collinearly using a dichroic mirror, with a carefully controlled delay between them. Due to dispersion in the experimental setup and nonlinear effects in the second harmonic generation process, the pulses were slightly chirped, but care was taken to keep each pulse compressed to within a factor of 2 of their Fourier limits at the sample. Both electron spectra and current yield were monitored with varying delays between the pulses. The key results of the measurement are high-

lighted in Figure 5-17.

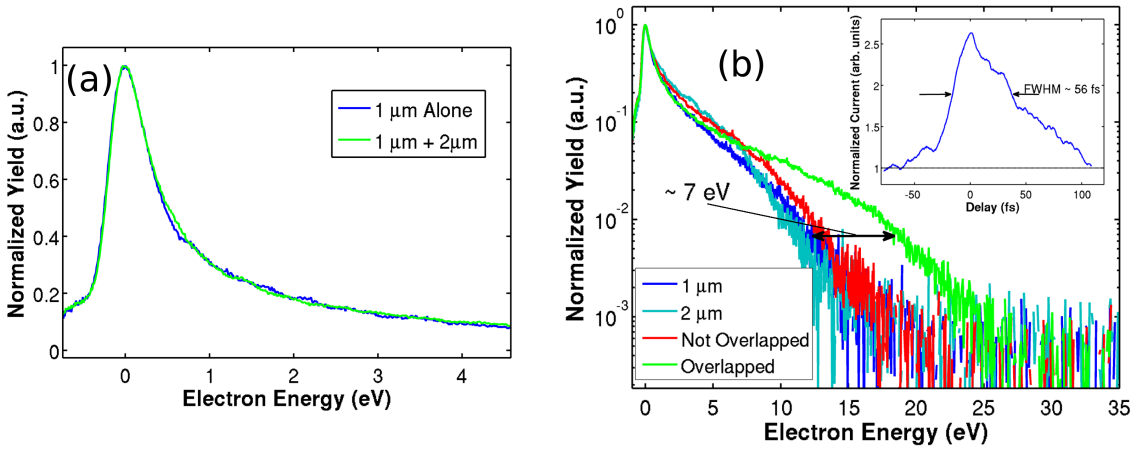

Figure 5-17: Comparison of the two-color results. (a) Spectra taken with the 1 μm pulse alone (blue), and overlapped in time with the 2 μm pulse (green) on a linear scale centered near the direct peak. (b) The spectra from 1 μm alone (blue), 2 μm alone (teal), 1 μm with 2 μm not overlapped in time (red) and overlapped in time (green) respectively. In (b), all curves are plotted on a log scale to emphasize the shift in cutoff energy of the lower yield plateau. In both (a) and (b), the spectra are all shifted such that their peaks are centered at 0 eV and are normalized to 1. The inset of (b) shows a typical cross correlation current trace where the current has been normalized to the baseline (5 pA , or 5 fC/pulse for the measurement shown).

The 2 μm pulse was focused to a spot size of ~ 170 μm FWHM, and the 1 μm pulse to a spot size of ~ 110 μm FWHM, and the incident beam angle was held at roughly 6° grazing incidence as in the text. Cross correlation current yield measurements were made at various 2 μm and 1 μm energies, and a typical trace is shown in the inset of Figure 5-17, where the current has been normalized to the baseline current (~ 5 pA corresponding to ~ 5 pC/pulse). The cross correlations show a spike in current that is prompt with the driving pulses, being just tens of femtoseconds in duration (56 fs FWHM for the case shown in inset of Figure 5-17). More importantly, no evidence of a long-lifetime tail on either side of the cross correlation profiles was observed, and the baseline current was verified to be simply the sum of the two individual input pulse responses. This demonstrates that any excited states that would contribute significantly to emission are short lived and would not contribute to effects, such as photo-field from the DC bias that would result in emission times much longer than the laser pulse. A numerical propagation

model [70] used to simulat the few-cycle pulse second harmonic generation in the interferometer produced a 1 μm pulse with an asymmetric temporal profile and structure similar to that seen in Figure 5-17 (inset), and may offer an explanation for the cross-correlation shape.

The energy spectra also indicate a prompt emission, and emphasize the importance of laser acceleration dynamics on the final energy profile of the electrons. For the measurement shown in Figure 5-17b, the 2 μm pulse was fixed at an energy of 730 nJ, and the 1 μm pulse at 200 nJ. The charge per pulse was recorded to be roughly 10 pC/pulse for the 2 μm pulse alone, 25 pC/pulse for the 1 μm pulse alone, and 50 pC/pulse when both are overlapped in time. When both are overlapped in time, the bandwidth of the main spectral peak is virtually unchanged from spectrum using the 1 μm pulse alone (Figure 5-17a). If the plateau extension were purely due to space-charge broadening of a low-energy pulse, models of single-tip emission, and the experimental results of others indicate that broadening should occur across the entire spectrum [65] (especially for the low-energy peak where there is the highest charge density). However, for the case of two-color fields, the laser acceleration dynamics are altered, and the cutoff can be extended up to $21U_p$ [64]. Fine delay structure was not observed in this measurement, however this is believed to be due to noise in the system and alignment issues that resulted in averaging (for example, a slight noncolinear alignment between the two pulses leading to spatial averaging over delay). Using a Simpleman model, a peak field strength for the 1 μm and 2 μm pulses was estimated by their respective cutoff energies to be 7.5 V/nm and 5.0 V/nm, respectively. The cutoff was then recalculated by superimposing the two pulses in the model, averaging over one cycle of delay. This showed a net increase in cutoff of around 12 eV, as compared to the measured value of 7 eV shown in Figure 5-17b. Current work is underway to resolve remaining experimental issues and verify finer delay structure due to the field driven emission and acceleration process.

5.3.5 Oxide Effects

The final consideration for a Si emitter is the effect of native oxide formation. It is well understood that Si will form a native oxide on the order of angstroms to nanometers depending on its exposure to atmospheric conditions. In DC field emission studies, it has been well documented that such oxide thicknesses are enough to dramatically alter the nature of tunneling emission [71–73]. By carefully testing Si tips where the native oxide was not removed before use, we were able to observe similar effects in optical tunneling and how the presence of the oxide alters the final electron energy spectrum.

These tests were performed on very similar tip structures as in Sections 5.3.1-5.3.4, only this time being spaced on a 10 μm square grid, with end ROC ranging from 5-10 nm. The laser source had an equivalent pulse duration and center wavelength of 800 nm, only this time at repetition rate of 1 kHz. The sample was also held at a low bias for these tests, only around 2 V coming directly from a positive drift tube voltage inside of the TOF spectrometer.

While testing electron spectra from the tips at various spots along the sample, a distinct, repeatable annealing process was observed when applying laser intensities above a certain threshold. For tips that had the oxide stripped prior to testing, this process was observed to a very small extent, and essentially not observed when care was taken to minimize opportunity for the oxide to grow before mounting and testing. This led to the conclusion that the native oxide must be responsible for the observed annealing process. To study the laser induced annealing effect, the following process was performed:

1. A fresh spot of tips was centered in front of the TOF spectrometer.

2. This spot was tested at low incident intensities ranging from 5×10^{10} W/cm^2 to 1.6×10^{11} W/cm^2.

3. The location was illuminated with an energy exceeding the annealing threshold for a fixed duration of time.

4. Steps two and three were repeated.

The results of this test are compiled in Figures 5-18-5-20.

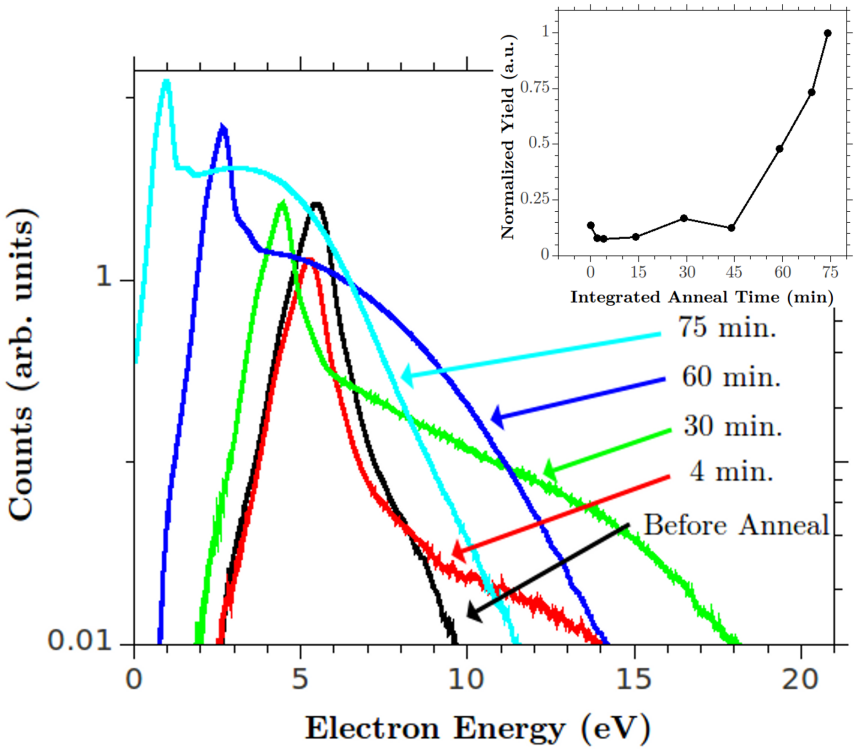

Figure 5-18: Electron spectra taken as a function of increased anneal time at an incident pulse energy of 0.6 μJ. The times given are the integrated anneal times, starting with an oxidized position on the sample at time 0. The annealing energies ranged from 1 to 2 μJ focused onto the same spot the spectra were taken from. Note the red shift of the main spectral peak. The inset shows integrated current yield as a function of anneal time. Initially there is a decrease in total electron yield before an eventual increase as anneal time is increased.

Figure 5-18 shows the effects of the anealing process on the electron spectrum and current yield. Each spectrum is taken at a peak intensity of 1.6×10^{11} W/cm^2 at the given accumulated anneal time. Three main trends are clear. First, the formation of a higher energy plateau that is not prevalent before the anneal. Secondly, there is a net red-shift of the main peak in each spectrum, from an original value of $\sim$ 5 eV before the anneal, to a value of $\sim$ 1 eV after the last anneal step. Finally, the total electron yield varies over the anneal, first slightly decreasing before finally increasing.

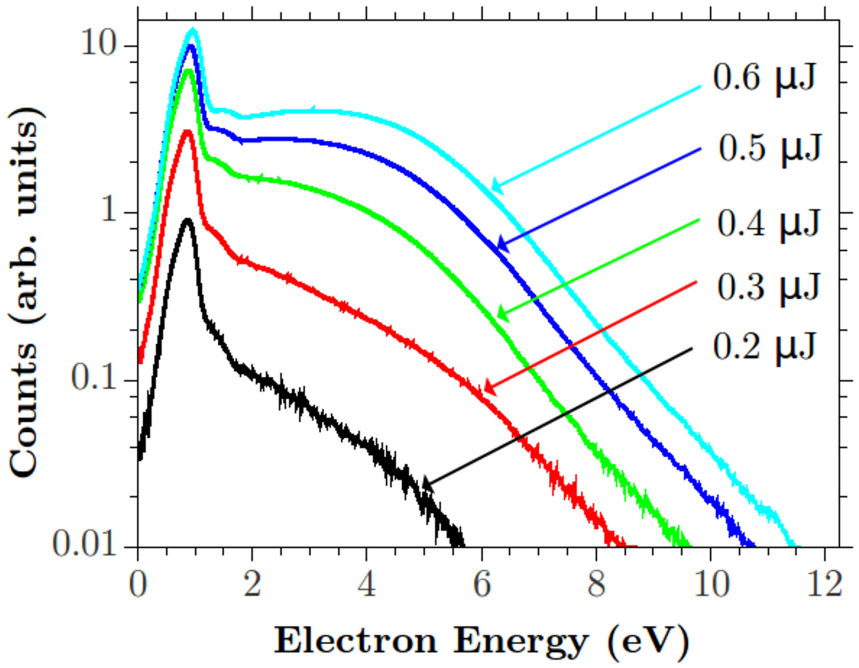

Figure 5-19: Experimental results from the power scaling study of the same spot after the final integrated anneal step has been performed. The main spectral peak shows little change with increasing pulse energy. A significant plateau forms at high pulse energies, extending outward with increased laser field strength.

Figure 3 shows a power scaling study after the total annealing process to demonstrate how the plateau scales with increased intensity, while the main spectral peak stays roughly fixed. This was true after all anneal times throughout the experiment. These features are both comparable to those already observed by others when performing energy-resolved photoemission experiments on metallic tips [13, 15, 74], and our own results discussed in Section 5.3.3. The question that needs to be addressed is if it is expected that the oxide indeed prevents a rescattering plateau for comparable peak intensities to bare Si.

Figure 5-20 shows the integrated current vs. incident pulse energy after the final annealing step. A slope change occurs near an incident pulse energy of 0.4 μJ indicating that the tip characterization is happening just near and above the transition from multiphoton to tunneling emission. An analysis of the slope transition point and the plateau feature extent, the predicted tip enhancement factors range from 10-14 giving a peak field strength range of 11-15.4 V/nm. This agrees quite

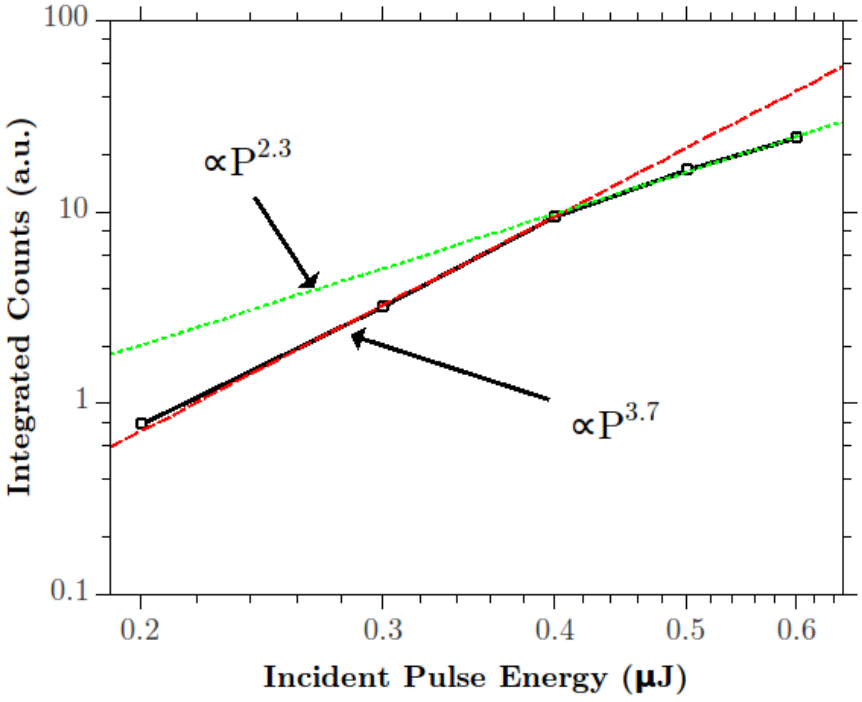

Figure 5-20: Plot of total MCP current yield with increasing incident energy. The slope transition is typical of a transition from multiphoton emission to the SF regime, occurring near $\gamma \approx 2$. The black circles indicate the measured values. The red and green trend-lines show the power law relation before and after the slope change respectively, where P is the pulse energy.

well with results from Section 5.3.2, which is expected as the Si doping factor and fabrication process is the same, and the overall geometry of the tip apex is quite similar. To compare our experimental results to theory, we turn back to the Simpleman model.

For the tunneling rates, a modified Fowler-Nordheim rate equation is used, following the procedure found in [72] in order to account for the effects of any oxide layer. Rather than the situation where a single step barrier is present (no oxide), with a thin oxide present, a double step barrier is formed. The intermediate work function W_{ox} is taken to be 3.5 eV for the Si to SiO_2 interface, while $\chi_{Si} = W_{ox} + \Delta\phi = 4.05$ eV. The schematic of the barriers and different tunneling scenarios are shown in Figure 5-21. Applying the WKB approximation to such a

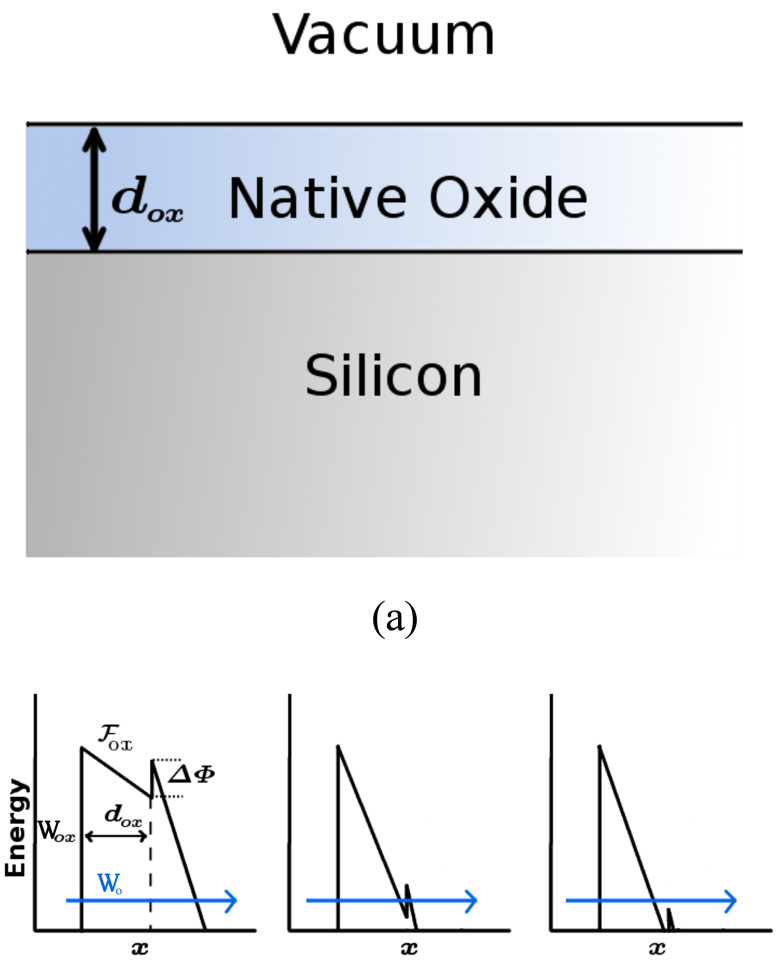

Figure 5-21: Schematic of oxide structure. In (a) the oxide layer structure in 1D is drawn. In (b) the energy levels are drawn and labeled along the axis of the layers. All three basic tunneling scenarios are also shown depending on the external field strength. At the highest field strengths, the electron tunnels over the extra barrier between the oxide and vacuum, without interacting with the intermediate quantum well formed.

barrier leads to the following rate equation.

$$J = \Theta(F_0(t))\frac{q^3|F(t)|^2}{16\pi^2\hbar\chi_{Si}B^2}\left(\frac{m^*}{m}\right)\exp\left(\frac{4\sqrt{2m}}{3q\hbar|F(t)|}\chi_{Si}^{3/2}C\right), \tag{5.20}$$

Here B and C are defined below.

$$\begin{aligned} B =& \epsilon_{ox}\sqrt{\frac{m_{ox}}{m}}\left[\left(\frac{W_{ox}}{\chi_{Si}}\right)^{1/2} - \right. \\ & \Theta(W_{ox} - q|F_{ox}(t)|d_{ox})\left(\frac{W_{ox} - q|F_{ox}(t)|d_{ox}}{\chi_{Si}}\right)^{1/2}\Bigg] \\ & + \Theta(\chi_{Si} - q|F_{ox}(t)|d_{ox})\left(1 - \frac{q|F_{ox}(t)|d_{ox}}{\chi_{Si}}\right)^{1/2} \end{aligned} \tag{5.21}$$

$$\begin{aligned} C =& \epsilon_{ox}\sqrt{\frac{m_{ox}}{m}}\left[\left(\frac{W_{ox}}{\chi_{Si}}\right)^{3/2} - \right. \\ & \Theta(W_{ox} - q|F_{ox}(t)|d_{ox})\left(\frac{W_{ox} - q|F_{ox}(t)|d_{ox}}{\chi_{Si}}\right)^{3/2}\Bigg] \\ & + \Theta(\chi_{Si} - q|F_{ox}(t)|d_{ox})\left(1 - \frac{q|F_{ox}(t)|d_{ox}}{\chi_{Si}}\right)^{3/2} \end{aligned} \tag{5.22}$$

$\Theta(t)$ is the Heaviside function, ϵ_{ox} the dielectric constant of the oxide at 800 nm, d_{ox} the oxide thickness, $F(t)$ is the enhanced electric field of the laser in vacuum just above the SiO_2 surface, and $F_{ox}(t) = F(t)/\epsilon_{ox}$ is the component of the electric field in the oxide. As in the experiment, the electric field is polarized along the direction of the tips. Here we also take m^* as the effective electron mass in Si and m_{ox} the effective mass in the oxide, m to be the mass of an electron and q the fundamental charge. Note that when d_{ox} is set to zero, or the oxide properties are set to that of the vacuum, B and C both go to 1 and the rate equation reduces to that of traditional FN theory as expected.

The electric field was modeled assuming a dipolar decay away from the tip as in Equation (5.8). Scattered electrons are modeled as elastically scattering off of the silicon surface, traveling through the SiO_2, since the scattering length of the electron within the oxide is on the order of 3nm [73], which is greater than the maximum modeled native oxide thickness. When calculating the electron trajectories, space-charge effects and multiple rescattering events are deemed negligible.

Figure 5-22 gives the results of the theoretical model of the power scaling experiment which matches quite well to the experimental spectra in Figure 5-19. The spectra were averaged over different peak field values, the average value taken to

be 12V/nm. A native oxide thickness of 0.5 nm was used, along with a roughly fitted reflection probability of $R = 0.3$. By turning off the reflectivity it can be shown that the sharp spectral peak is due purely to the electron trajectories that do not rescatter, and the plateau feature is due to those that do. While a free electron with no scattering can only pick up a maximum of $2U_p \approx 2.8$ eV from the driving laser field in our case at an incident of 0.6 μJ, only the inclusion of rescattered electrons accounts for the high energies observed experimentally.

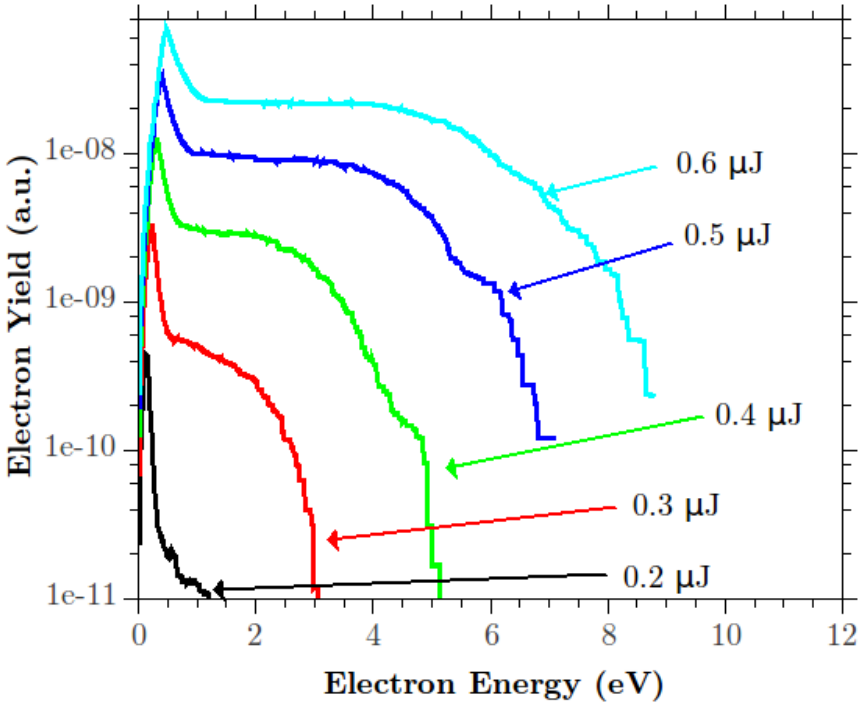

Figure 5-22: Model results when simulating the experimental incident power study. The spectral features qualitatively match those of the experiment, each spectra having a sharp low energy peak with a broad plateau. The plateau can be turned on or off in the model through the electron rescattering probability, and scales with incident energy similar to the experimental data.

To explain the red shift and increased current yield observed throughout the annealing process, a charging-, thinning-oxide model is used. Trapped charge at the surface explains the spectral offset, and the subsequent loss of charge as a function of anneal due to oxide thinning leads to the observed red-shift. Furthermore, a thinning oxide explains the net increase in current yield as a function of anneal

time. To explore this explanation, we have modeled an oxide thinning from 0.9 nm down to 0.5 nm.

For simplicity, the charge is assumed to be spread evenly throughout the oxide with a surface density around 5.5×10^{12} electrons/cm^2, which is consistent with trap densities commonly found near SiO_2-Si interfaces, especially for native oxides where the impurity concentration can be large at the surface [72]. The peak field strength of the trapped charge is taken to be 0.5 V/nm. As this field is an order of magnitude below that due to the laser, the effects of this field on emission probability is neglected. We also assumed that the changing oxide thickness does not significantly alter the field enhancement factor, α. The results of this model are shown in Figure 5-23.

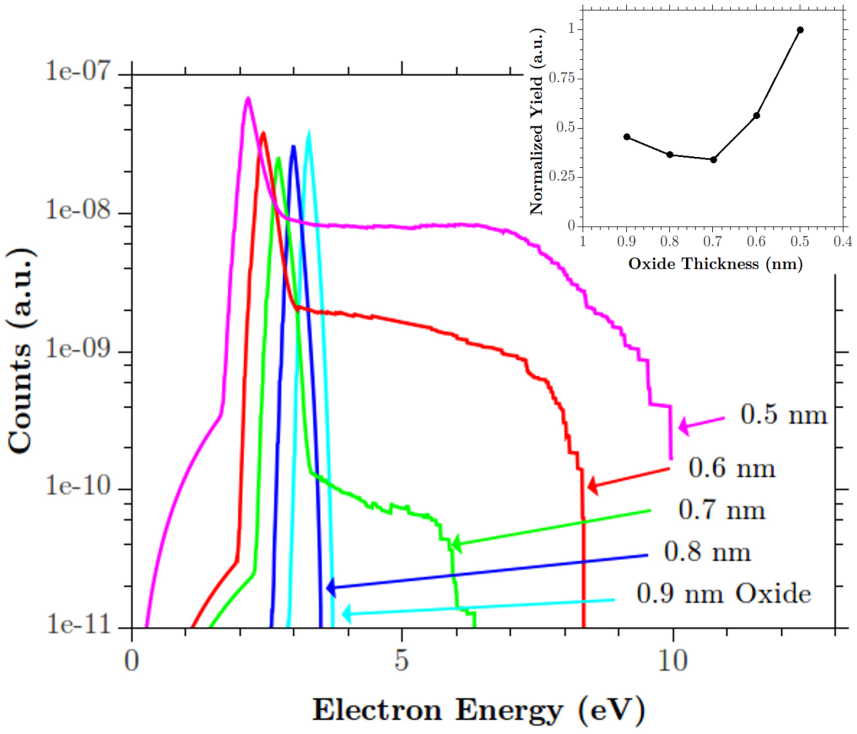

Figure 5-23: Simulation results for a tip-model including a charged, thinning oxide. Three basic trends are reproduced in the model. First the prevalent red-shift is introduced due to the reduction of surface charge. Secondly, it accurately models the plateau suppression before anneal. Thirdly, the thinning-oxide models first a reduction and then increase in net electron yield. The inset shows the modeled total electron yield as a function of decreasing oxide thickness.

Though simple, the model qualitatively reproduces all three trends as observed

experimentally. First, the initial decrease and then eventual increase in current yield as a function of thinning oxide. This is a result of the changing potential barrier profile as a function of oxide thickness which, at certain d_{ox} values, can lead to higher emission when the oxide is increased while keeping the applied field fixed. Secondly, the presence and reduction of surface charge easily explains the 4-5 eV shift of the energy spectra as observed in the experiment. However, it is clear that the effect of the oxide thinning occurs in the experimental data before a significant red-shift. This is consistent with the charge being located nearer to the interface of the Si-SiO_2. Finally, due to the extension of the tunnel exit away from the tip surface, the electron rescattering is reduced thus suppressing the high energy plateau before the anneal.

Despite explaining these features, it is clear that more work has to be done to understand all of the underlying dynamics at play during the annealing process more fully. One striking difference between the experiment and simulations is the significantly broader plateau observed for intermediate anneal times in the experimental data that is not reproduced in the simulation.

Chapter 6

Outlook

It will be interesting to see the next decade of advances in attosecond science. There are many indications that the new frontier for the field lies in creating on-chip, solid-state devices. This thesis has presented much of the groundwork necessary for creating such devices on a large scale. One area of particular interest to me is one where nanoscale tips have already seen tremendous application: microscopy. Near-field tunneling has been utilized in the scanning tunneling electron miscrope for many years. By coupling this with a pulsed laser, unprecedented timing resolution could be added, creating a time-resolved scanning tunneling electron microscope. This might be the breakthrough necessary for providing much of the rich information on chemical structure and electron dynamics that attosecond science has been quick to promise, but slow to deliver.

However, creating such a device will require yet more study of the basic processes at play in laser driven emission from nanostructures, especially in the context of coupling this emission with a near-field tunneling microscope. One particular challenge will be to develop pulse retrieval techniques for the electron packets emitted from the nanostructures, allowing for experimental measurements of their temporal resolution. It would truly be satisfying if the work on attosecond EUV pulse retrieval documented in Chapters 3 and 4 proves useful in this regard, bringing the work in this thesis full circle.

With regard to attosecond pulse retrieval, it was recently brought to my at-

tention that others have developed ways of incorporating the concept of partial coherence into FROG [75]. If it is possible to extend these ideas to the VTGPA algorithm, it would bring it one step closer to becoming the most complete retrieval approach available in attosecond science. Furthermore, as more of the field moves toward integrating attosecond science with solid state systems, where decoherence is much more critical, accounting for partial coherence will prove to be invaluable.

Appendix A

Magnetic Field Effects

To examine why the magnetic field has been neglected in all preceeding calculations, the classical motion of an electron is an electromagnetic field is considered. For the sake of simplicity, it is assumed that at time $t = 0$ and position $\mathbf{z} = (0, 0, 0)$ an electron is injected at rest into an electromagnetic field traveling in the z direction described by

$$\mathbf{F} = F_0 \cos(kz - \omega t)\hat{x} \tag{A.1}$$

$$\mathbf{B} = \frac{F_0}{c} \cos(kz - \omega t)\hat{y}, \tag{A.2}$$

where c is the speed of light in the vacuum. A calculation of the electron acceleration, $\mathbf{a}$, yields

$$\mathbf{a} = -\frac{q}{m} F_0 \cos(kz - \omega t)\left[\frac{v_x}{c}\hat{z} + \left(1 - \frac{v_z}{c}\right)\hat{x}\right], \tag{A.3}$$

where v_x is the velocity in the x direction and v_z the velocity in the y direction. It is clear that if $v_z/c \ll 1$, which is equivalent to stating that the excursion in z is much less than a wavelength over one cycle of radiation, the effects of the magnetic field can be safely ignored, and the dipole approximation holds. The magnetic field is ignored when describing all of the experimental work presented in this thesis as the electron velocities never approach such relativistic speeds.

The expression above is continued in order to give insight into the upper limit

on the electric field strength to satisfy the dipole approximation. The expression for the velocity in z due to the magnetic field component is approximated by

$$v_z \approx \frac{q^2 F_0^2}{2m^2 c\omega^2} \sin^2 \omega t. \tag{A.4}$$

For this to be consistent with the original approximation that $v_z/c \ll 1$ requires that

$$\frac{q^2 F_0^2}{2m^2\omega^2 c^2} \ll 1. \tag{A.5}$$

Thus, as long as

$$F_0 \ll \frac{m\omega c}{q}\sqrt{2}, \tag{A.6}$$

the dipole approximation holds.

Appendix B

Consideration of Emitter Size and Ground State Population

In this section, the emitter size and ground state populations are considered. To do this, a total emission probability for each given initial $\mathbf{k}$ inside of the substrate is defined. This can then be used in conjunction with the initial ground state distribution of any given substrate to determine the total emission yield and outgoing momentum spectrum. For an input optical pulse and incoming ground state plane wave with momentum $\mathbf{k}$ having unity amplitude impinging on a step potential boundary, we define the outgoing charge distribution as a function of the final momentum $\mathbf{p}$ as

$$w_{\mathbf{p}} = \frac{\text{Charge/Area/Pulse Momentum Distribution}}{J_{in}(k_z)} \tag{B.1}$$

$$\approx \frac{4k_z m_z^*}{B(k_z^2+\alpha^2)}|M_{\mathbf{p}}|^2, \tag{B.2}$$

where $J_{in}(k_z)$ is the charge current density at initial longitudinal momentum k_z incident on the barrier. We have also taken account of a general effective mass tensor m^* by using the effective mass in the z direction inside of the material, m_z^*. In deriving equation (B.2), it has been assumed that the emission is constant over some area B, and that the the electric field is constant in this region. Finally, the top

integral is over all outgoing momenta $\mathbf{p}$, and α describes the evanescently decaying portion of the ground state in the vacuum half space, and is expressed as

$$\alpha = \sqrt{2m\left(U + \frac{k_x^2(m_x^* - m)}{2m_x^* m} + \frac{k_y^2(m_y^* - m)}{2m_y^* m} - k_z^2/(2m_z^*)\right)}, \tag{B.3}$$

where U is the step-barrier height. Note that the transverse terms disappear if the effective mass is the same in the transverse direction as that in the vacuum. We assume the external electric field, $\mathbf{F}$, to be polarized parallel to the surface normal of the emitter as earlier in the text. Note also that the curvature of the tip has been neglected in the potential barrier and ground state assumptions, assuming it is an extended flat surface. Thus, the localization is approximated by assuming that there is an electric field "hot-spot" just over a region of area B on the emitter surface.

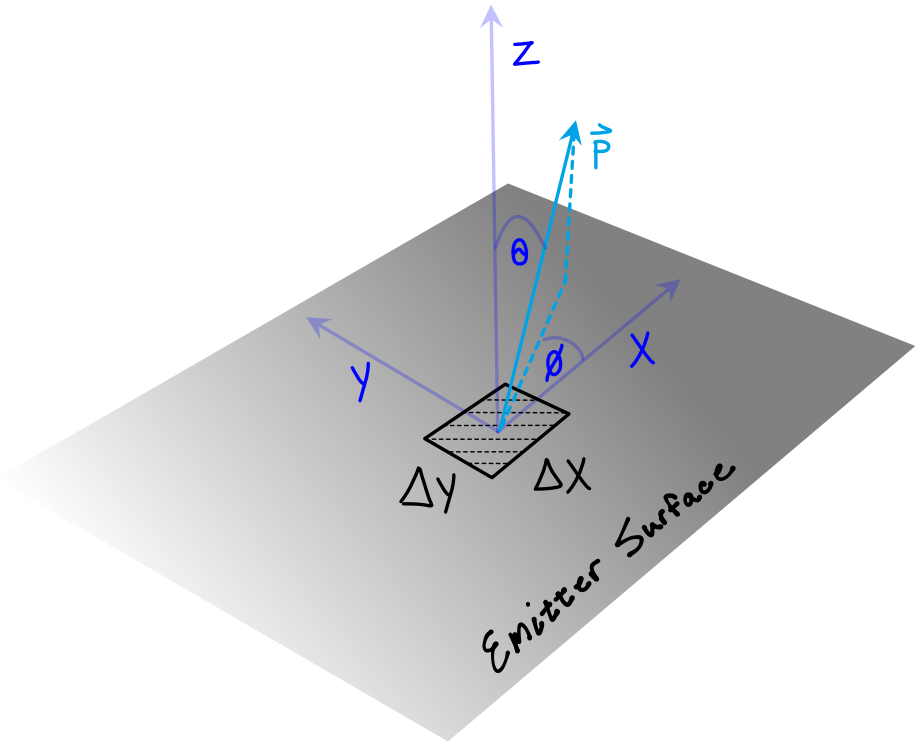

Figure B-1: Schematic of an emitter as simulated. There is a hot-spot (square dashed region) of width Δx by Δy where a driving electric field pulse, $\mathbf{F}(t)$, is present. For all of the discussion that follows, $\mathbf{F}$ is assumed to be pointing along z. The relevant angles in spherical coordinates are also shown along with a potential outgoing momentum vector $\mathbf{p}$.

Moving forward, the expression of $M_{\mathbf{p}}$ is approximated to the first order using strong-field perturbation theory as

$$M_{\mathbf{p}}^{(1)} = \frac{-i}{\hbar}\int d\tau \exp\left\{\frac{i}{\hbar}\left(S_{p_z}(\tau) + \left(\frac{p_\perp^2}{2m} - W(\mathbf{k})\right)\tau\right)\right\} qF(\tau)\times \\ \frac{1}{(2\pi)^{3/2}}\int d^3\mathbf{r} e^{-i(p_z+qA(\tau))z/\hbar} e^{-i(p_x-k_x)x/\hbar} e^{-i(p_y-k_y)y/\hbar} e^{-\alpha z/\hbar} z, \tag{B.4}$$

where $p_\perp$ is the outgoing transverse momentum magnitude, and

$$W(\mathbf{k}) = k_x^2/(2m_x^*) + k_y^2/(2m_y^*) + k_z^2/(2m_z^*) - U \tag{B.5}$$

is the electron energy for an initial state $\mathbf{k}$. We can break up the spatial portion of the matrix element calculation in equation (B.4) into the integral along z (normal to the tip), and that along the surface in x and y. This leads us to our discussion on the effects of limiting the emission region in space. If we assume area B extends over a small region Δx in x and Δy in y, we can then pull the surface integral portion out of the calculation of $|M_{\mathbf{p}}|^2$ as a pre-factor, Γ, being

$$\Gamma(\Delta x, \Delta y, k_x, k_y, p_x, p_y) = \frac{\Delta x^2 \Delta y^2}{(2\pi)^2}\,\mathrm{sinc}^2((k_x - p_x)\Delta x/(2\hbar))\times \\ \mathrm{sinc}^2((k_y - p_y)\Delta y/(2\hbar)). \tag{B.6}$$

Thus the expression of $|M_{\mathbf{p}}^{(1)}|^2$ becomes

$$|M_{\mathbf{p}}^{(1)}|^2 = \Gamma\left|\frac{-i}{\hbar}\int d\tau \exp\left\{\frac{i}{\hbar}\left(S_{p_z}(\tau) + \left(\frac{p_\perp^2}{2m} - W(\mathbf{k})\right)\tau\right)\right\} qF(\tau)\times \\ \frac{1}{\sqrt{2\pi}}\int_0^\infty dz e^{-i(p_z+qA(\tau))z/\hbar} e^{-\alpha z/\hbar} z\right|^2. \tag{B.7}$$

For now, we can focus on Γ, as it dictates the behavior of the outgoing transverse momentum distribution of the emitted electron bunch as a function of the emitter area. As Δx and Δy are reduced, the width of each respective sinc function widens in p_x and p_y around a center value of k_x and k_y. The interpretation of this

is that, due to the uncertainty principle, as the location of the emitter area is more and more well defined, the outgoing transverse momentum becomes less well defined. When the emitter area is squeezed down to a point source of infinitesimal area, the central lobes of the sinc functions become infinitely wide, and the electrons are equally emitted in all directions with no conservation of initial transverse momentum.

On the other hand, for a large enough emitter area, the sinc functions become more peaked around the initial transverse momenta in x and y, leading to the interpretation that for an infinitely large emitter area the initial transverse momentum is conserved after emission. In fact, this is mathematically shown by taking the limit of Γ as both Δx and Δy both go to infinity. This task is simplified by noting that

$$\lim_{\Delta x \to \infty} \Delta x \operatorname{sinc}^2((k_x - p_x)\Delta x/(2\hbar)) = 2\pi\delta((k_x - p_x)/\hbar). \tag{B.8}$$

By plugging this into the expression for Γ, we have

$$\lim_{\Delta x \to \infty, \Delta y \to \infty} \Gamma = B\delta((k_x - p_x)/\hbar)\delta((k_y - p_y)/\hbar). \tag{B.9}$$

Clearly, the delta functions imply conservation of initial transverse momentum, and only make sense when coupled with an integration over the initial ground state momentum distribution, which will be performed later. Furthermore, note that for a large enough emission area, the emission rate scaling is linearly proportional with the emitter area, B. While seemingly obvious that tiny emitters should at some point have a transverse momentum spread dominated by the uncertainty principle, this analysis is often ignored (such as in [38]). As the state of the art in fabrication and characterization of such emitters continues, such analysis should be performed to properly characterize the spatial emission profile and fundamental emittance of such devices.

We can rewrite the expression for $w_{\mathbf{p}}$ as

$$w_{\mathbf{p}} = \frac{4k_z m_z^*}{B(k_z^2 + \alpha^2)} \left(\Gamma \left| M_{p_z}^{(1)} \right|^2 \right), \tag{B.10}$$

where

$$M_{p_z}^{(1)} = \frac{-i}{\hbar}\int d\tau \exp\left\{\frac{i}{\hbar}\left(S_{p_z}(\tau) + \left(\frac{p_\perp^2}{2m} - W(\mathbf{k})\right)\tau\right)\right\} qF(\tau)\times \frac{1}{\sqrt{2\pi}}\int_0^\infty dz e^{-i(p_z+qA(\tau))z/\hbar} e^{-\alpha z/\hbar} z. \tag{B.11}$$

This expression should look familiar to the one-dimensional calculation of the strong-field emission rate, just with a modified ground state energy that depends on the initial transverse momentum. In fact, if the effective mass is simply the same as the rest mass in vacuum, this expression only depends on k_z, and is identical to the one-dimensional calculation. Thus, this further justifies the calculation for total electron yield used in Chapter 5, where it was assumed the 1D calculation is valid to within some constant pre-factor proportional to the emitter area.

While not shown explicitly here, this same analysis can be extended to higher order terms of strong-field perturbation theory, which accounts for rescattering events with the tip surface. In each case, if the emitter area is large enough, the transverse momentum is conserved, and the emission rate is directly proportional to that given by the 1D calculation to within a constant pre-factor.

The analysis above is extended in a similar form as that found in [38] to fully incorporate the ground state distribution into the final yield calculation. The total current density incident on the surface of the emitter, J_s is given by

$$J_s = \frac{1}{\hbar^3}\int d^3\mathbf{k} F(\mathbf{k}), \tag{B.12}$$

where $F(k)$ defines the ground state momentum distribution. To calculate the total charge yield then requires a rather complex series of integrations, where we sum over all initial state momenta $\mathbf{k}$, weighting each term with the probability of a transition to final state momentum, $\mathbf{p}$, given by $w_{\mathbf{p}}$. Finally, we integrate over all possible final momenta $\mathbf{p}$ to give the total emitted charge Q,

$$Q = \frac{1}{\hbar^6}\int d^3\mathbf{p}\int d^3\mathbf{k} F(\mathbf{k}) w_{\mathbf{p}}(\mathbf{k}). \tag{B.13}$$

The expression above can be simplified significantly if it is assumed we are in the "large emitter regime", thus making the sinc functions in Equation (B.6) collapse into the form given by Equation (B.9). In this case, due to momentum conservation, k_x and k_y can be written as

$$k_x = p_z \tan(\theta)\cos(\phi) \tag{B.14}$$

$$k_y = p_z \tan(\theta)\sin(\phi), \tag{B.15}$$

where θ and ϕ are the outgoing momentum angles relative to the z and x axes respectively. It can then also be shown that

$$\int dp_x \int dp_y = \int dk_x \int dk_y = \int d\Omega \sec^3(\theta) p_z^2, \tag{B.16}$$

where the integral over Ω is the integral over the outgoing solid angle.

Equation (B.13) can now be combined with Equation (B.16) to give the differential cross section $\frac{dQ}{d\Omega}$,

$$\frac{dQ}{d\Omega} = \frac{\sec^3(\theta)}{\hbar^4} \int dp_z p_z^2 \int dk_z F(\theta, \phi, k_z, p_z) \times \frac{4 k_z m_z^*}{k_z^2 + \alpha(\theta, \phi, k_z, p_z)^2} \left| M_{p_z}^{(1)}(\theta, \phi, k_z) \right|^2. \tag{B.17}$$

This gives the spatial charge distribution, and can be integrated over to give the total charge yield. The integral is rather complicated for most general ground-state charge distributions if there is a mismatch in the transverse effective mass values and the electron rest mass in vacuum. This difference makes $M_{p_z}^{(1)}$ and α both depend on θ and ϕ. However, it also leads to potential applications where the effective masses can be chosen in such a way to help engineer the emittance of the outgoing electron packet.

If we assume that the effective mass is simply $m_x^* = m_y^* = m$, then the total yield Q can be written in a similar form as that found in [38]. The ground state distribution can be taken from the Fermi-Dirac distribution in a general conduc-

tor/semiconductor.

$$F(\mathbf{k}) = \frac{k_z}{4\pi^3 m_z^* (e^{\beta[k_x^2/(2m_x^*)+k_y^2/(2m_y^*)+k_z^2/(2m_z^*)-\Delta E]}+1)} \tag{B.18}$$

The major parameter that controls the shape of the distribution relative to the ground state momentum is ΔE. For a metal, $\Delta E = E_f$, the Fermi energy, and the potential barrier height is described as $U = W + E_f$, where W is the metal work function. However, for a semiconductor, the barrier height is given by the electron affinity, χ, which is the energy difference between the bottom of the conduction band and the vacuum level. In this case, $\Delta E = E_f - E_c$, where E_c is the conduction band energy, which is typically negative even for the case of a doped semiconductor. For a clearer picture of the energy levels within each type of material see Figure B-2.

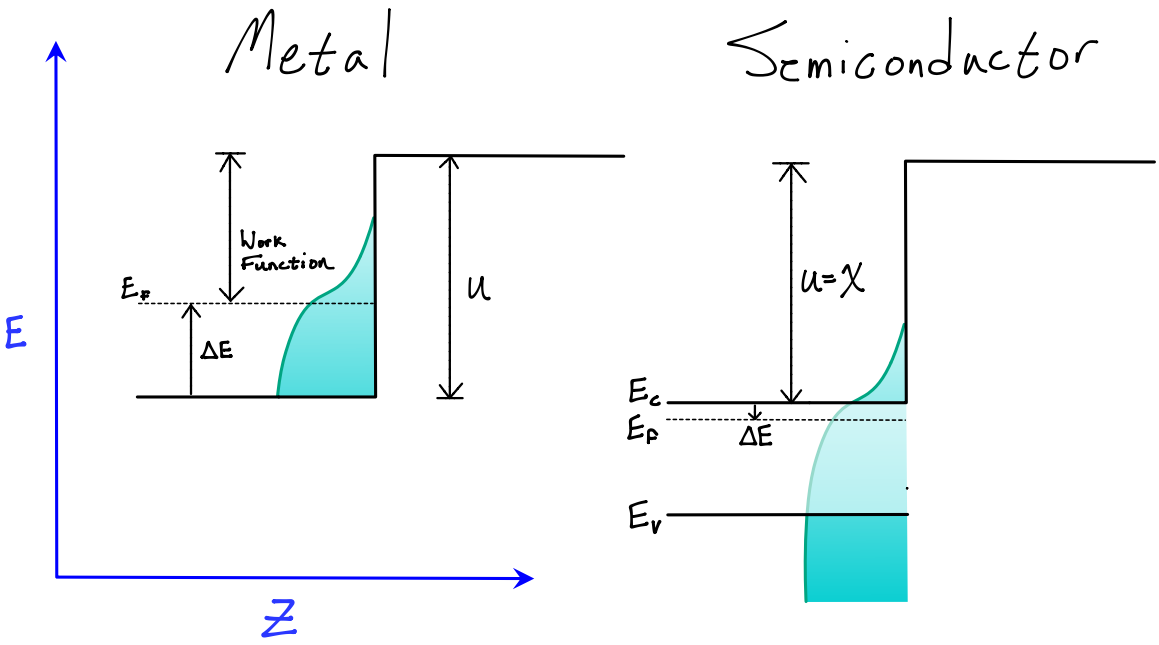

Figure B-2: Schematic of relevant energy levels for both a metal and a semiconductor. In each, the barrier at the material/vacuum interface has been idealized as a step-potential. The shaded region shows a typical Fermi-Dirac distribution of Equation (B.18). Due to the bandgap, the distribution of available electrons is different within a semiconductor as compared to a metal.

Since $m_x^* = m_y^* = m$, $F(\theta, k_z, p_z)$ is the only term that depends on the outgoing polar angle of the electron, θ. However, due to the cylindrical symmetry of the

problem, there is no dependence on the azimuthal angle, ϕ. Thus, all of the terms that depend on the outgoing angle can be pulled out, and an integration performed over a 2π solid angle above the surface to give the following expression for Q,

$$Q = \frac{2m_z^*}{\pi^2\beta\hbar^4}\int dk_z\left(\frac{k_z^2}{k_z^2+\alpha(k_z)^2}\right)\ln\left[1+e^{\beta(\Delta E-k_z^2/(2m_z^*))}\right]\times \int dp_z\left|M_{p_z}^{(1)}(k_z)\right|^2. \tag{B.19}$$

This expression is a direct analogue to that found in [38] where the derivation has been performed for a pulsed electric field rather than a continuous wave source. This explains why the summation of discrete final energies p_n is replaced by an integration over a continuous energy distribution in p_z. Note that if the electron energy distribution over $\mathbf{k}$ is sufficiently narrow, the expression reduces to within a constant factor of $\int dp_z\left|M_{p_z}^{(1)}(k_z)\right|^2$, which was used to describe the total charge yield from Si tips.

Bibliography

[1] R. Velotta, S. Stagira, S. De Silvestri, M. Nisoli, G. Sansone, E. Benedetti, F. Calegari, C. Vozzi, L. Avaldi, R. Flammini, L. Poletto, P. Villoresi, and C. Altucci, "Isolated single-cycle attosecond pulses," *Science*, vol. 314, no. 5798, pp. 443–446, Jan. 2006, 000241382500035. [Online]. Available: http://www.sciencemag.org/cgi/content/abstract/314/5798/443

[2] P. M. Paul, E. S. Toma, P. Breger, G. Mullot, F. Auge, P. Balcou, H. G. Muller, and P. Agostini, "Observation of a train of attosecond pulses from high harmonic generation," *Science*, vol. 292, no. 5522, pp. 1689–1692, Jun. 2001. [Online]. Available: http://www.sciencemag.org/cgi/content/abstract/292/5522/1689

[3] E. Goulielmakis, M. Schultze, M. Hofstetter, V. S. Yakovlev, J. Gagnon, M. Uiberacker, A. L. Aquila, E. M. Gullikson, D. T. Attwood, R. Kienberger, F. Krausz, and U. Kleineberg, "Single-cycle nonlinear optics," *Science*, vol. 320, no. 5883, pp. 1614–1617, Jun. 2008. [Online]. Available: http://www.sciencemag.org/cgi/content/abstract/320/5883/1614

[4] F. Krausz and M. Ivanov, "Attosecond physics," *Reviews of Modern Physics*, vol. 81, no. 1, pp. 163–72, Jan. 2009. [Online]. Available: http://link.aps.org/abstract/RMP/v81/p163

[5] M. J. Abel, T. Pfeifer, P. M. Nagel, W. Boutu, M. J. Bell, C. P. Steiner, D. M. Neumark, and S. R. Leone, "Isolated attosecond pulses from ionization gating of high-harmonic emission," *Chemical Physics*, vol. 366, no. 1-3, pp. 9–14, Dec. 2009. [Online]. Available: http://www.sciencedirect.com/science/article/B6TFM-4X8CD34-2/2/caa009128f7ae89aeb974af0b763afa4

[6] T. Pfeifer, M. J. Abel, P. M. Nagel, W. Boutu, M. J. Bell, Y. Liu, D. M. Neumark, and S. R. Leone, "Measurement and optimization of isolated attosecond pulse contrast," *Optics Letters*, vol. 34, no. 12, pp. 1819–1821, Jun. 2009. [Online]. Available: http://ol.osa.org/abstract.cfm?URI=ol-34-12-1819

[7] P. B. Corkum and F. Krausz, "Attosecond science," *Nat Phys*, vol. 3, no. 6, pp. 381–387, Jun. 2007. [Online]. Available: http://dx.doi.org/10.1038/nphys620

[8] Y. Nabekawa, T. Shimizu, T. Okino, K. Furusawa, H. Hasegawa, K. Yamanouchi, and K. Midorikawa, "Conclusive Evidence of an Attosecond Pulse Train Observed with the Mode-Resolved Autocorrelation Technique," *Physical Review Letters*, vol. 96, no. 8, p. 083901, Feb. 2006. [Online]. Available: http://link.aps.org/doi/10.1103/PhysRevLett.96.083901

[9] M. Hentschel, R. Kienberger, C. Spielmann, G. A. Reider, N. Milošević, T. Brabec, P. Corkum, U. Heinzmann, M. Drescher, and F. Krausz, "Attosecond metrology," *Nature*, vol. 414, no. 6863, pp. 509–513, Nov. 2001. [Online]. Available: http://dx.doi.org/10.1038/35107000

[10] B. Piglosiewicz, S. Schmidt, D. J. Park, J. Vogelsang, P. Grof, C. Manzoni, P. Farinello, G. Cerullo, and C. Lienau, "Carrier-envelope phase effects on the strong-field photoemission of electrons from metallic nanostructures," *Nature Photonics*, vol. 8, no. 1, pp. 37–42, Jan. 2014. [Online]. Available: http://www.nature.com/nphoton/journal/v8/n1/abs/ nphoton.2013.288.html

[11] M. E. Swanwick, P. D. Keathley, A. Fallahi, P. R. Krogen, G. Laurent, J. Moses, F. X. Kärtner, and L. F. Veálsquez-García, "Nanostructured Ultrafast Silicon-Tip Optical Field-Emitter Arrays," *Nano Letters*, vol. 14, no. 9, pp. 5035–5043, Sep. 2014. [Online]. Available: http://dx.doi.org/10.1021/nl501589j

[12] P. Dombi, A. Hörl, P. Rácz, I. Márton, A. Trügler, J. R. Krenn, and U. Hohenester, "Ultrafast strong-field photoemission from plasmonic nanoparticles," *Nano Letters*, Jan. 2013. [Online]. Available: http://dx.doi.org/10.1021/nl304365e

[13] G. Herink, D. R. Solli, M. Gulde, and C. Ropers, "Field-driven photoemission from nanostructures quenches the quiver motion," *Nature*, vol. 483, no. 7388, pp. 190–193, Mar. 2012. [Online]. Available: http://www.nature.com/nature/journal/v483/n7388/full/nature10878.html

[14] M. Krüger, M. Schenk, M. Forster, and P. Hommelhoff, "Attosecond physics in photoemission from a metal nanotip," *Journal of Physics B: Atomic, Molecular and Optical Physics*, vol. 45, no. 7, p. 074006, Apr. 2012. [Online]. Available: http://iopscience.iop.org/0953-4075/45/7/074006

[15] M. Krüger, M. Schenk, and P. Hommelhoff, "Attosecond control of electrons emitted from a nanoscale metal tip," *Nature*, vol. 475, no. 7354, pp. 78–81, Jul. 2011. [Online]. Available: http://dx.doi.org/10.1038/nature10196

[16] R. Bormann, M. Gulde, A. Weismann, S. V. Yalunin, and C. Ropers, "Tip-enhanced strong-field photoemission," *Physical Review Letters*, vol. 105, no. 14, p. 147601, 2010. [Online]. Available: http://link.aps.org/doi/10.1103/PhysRevLett.105.147601

[17] J. L. Krause, K. J. Schafer, and K. C. Kulander, "High-order harmonic generation from atoms and ions in the high intensity regime," *Physical Review Letters*, vol. 68, no. 24, pp. 3535–3538, Jun. 1992. [Online]. Available: http://link.aps.org/doi/10.1103/PhysRevLett.68.3535

[18] A. L'Huillier and P. Balcou, "High-order harmonic generation in rare gases with a 1-ps 1053-nm laser," *Physical Review Letters*, vol. 70, no. 6, pp. 774–777, Feb. 1993. [Online]. Available: http://link.aps.org/doi/10.1103/PhysRevLett.70.774

[19] N. Sarukura, K. Hata, T. Adachi, R. Nodomi, M. Watanabe, and S. Watanabe, "Coherent soft-x-ray generation by the harmonics of an ultrahigh-power KrF laser," *Physical Review A*, vol. 43, no. 3, pp. 1669–1672, Feb. 1991. [Online]. Available: http://link.aps.org/doi/10.1103/PhysRevA.43.1669

[20] M. Lewenstein, P. Balcou, M. Y. Ivanov, A. L'Huillier, and P. B. Corkum, "Theory of high-harmonic generation by low-frequency laser fields," *Physical Review A*, vol. 49, no. 3, p. 2117, Mar. 1994. [Online]. Available: http://link.aps.org/doi/10.1103/PhysRevA.49.2117

[21] F. Quéré, Y. Mairesse, and J. Itatani, "Temporal characterization of attosecond XUV fields," *Journal of Modern Optics*, vol. 52, pp. 339–360, Jan. 2005. [Online]. Available: http://www.ingentaconnect.com/content/tandf/tmop/2005/00000052/F0020002/art00013

[22] J. Gagnon, E. Goulielmakis, and V. Yakovlev, "The accurate FROG characterization of attosecond pulses from streaking measurements," *Applied Physics B*, vol. 92, no. 1, pp. 25–32, Jun. 2008. [Online]. Available: http://adsabs.harvard.edu/abs/2008ApPhB..92...25G

[23] Y. Mairesse and F. Quéré, "Frequency-resolved optical gating for complete reconstruction of attosecond bursts," *Physical review A*, vol. 71, no. 1, p. 011401, Jan. 2005, 000227283300008. [Online]. Available: http://pra.aps.org/abstract/PRA/v71/i1/e011401

[24] G. Laurent, W. Cao, I. Ben-Itzhak, and C. L. Cocke, "Attosecond pulse characterization," *Optics Express*, vol. 21, no. 14, pp. 16 914–16 927, Jul. 2013. [Online]. Available: http://www.opticsexpress.org/abstract.cfm?URI=oe-21-14-16914

[25] M. Chini, S. Gilbertson, S. D. Khan, and Z. Chang, "Characterizing ultrabroadband attosecond lasers," *Optics Express*, vol. 18, no. 12, pp. 13 006–13 016, Jun. 2010. [Online]. Available: http://www.opticsexpress.org/abstract.cfm?URI=oe-18-12-13006

[26] P. D. Keathley, A. Sell, W. P. Putnam, S. Guerrera, L. Velásquez-García, and F. X. Kärtner, "Strong-field photoemission from silicon field emitter arrays," *Annalen der Physik*, 2012.

[27] W. Becker, F. Grasbon, R. Kopold, D. Milošević, G. Paulus, and H. Walther, "Above-threshold ionization: From classical features to quantum effects," in *Advances In Atomic, Molecular, and Optical Physics*. Academic Press, 2002, vol. Volume 48, pp. 35–98. [Online]. Available: http://www.sciencedirect.com/science/article/pii/S1049250X02800064

[28] D. B. Milošević, G. G. Paulus, D. Bauer, and W. Becker, "Above-threshold ionization by few-cycle pulses," *Journal of Physics B: Atomic, Molecular and Optical Physics*, vol. 39, pp. R203–R262, Jul. 2006. [Online]. Available: http://iopscience.iop.org/0953-4075/39/14/R01

[29] Á. Valfells, D. W. Feldman, M. Virgo, P. G. O'Shea, and Y. Y. Lau, "Effects of pulse-length and emitter area on virtual cathode formation in electron guns," *Physics of Plasmas (1994-present)*, vol. 9, no. 5, pp. 2377–2382, Apr. 2002. [Online]. Available: http://scitation.aip.org/content/aip/journal/pop/9/5/10.1063/1.1463065

[30] L. V. Keldysh, "Ionization in the Field of a Strong Electromagnetic Wave," *Sov. Phys. JETP*, vol. 20, no. 5, pp. 1307–1314, 1965.

[31] W. Gordon, "Der Comptoneffekt nach der Schrödingerschen Theorie," *Zeitschrift für Physik*, vol. 40, no. 1-2, pp. 117–133, Jan. 1926. [Online]. Available: http://link.springer.com/article/10.1007/BF01390840

[32] D. M. Wolkow, "Über eine Klasse von Lösungen der Diracschen Gleichung," *Zeitschrift für Physik*, vol. 94, no. 3-4, pp. 250–260, Mar. 1935. [Online]. Available: http://link.springer.com/article/10.1007/BF01331022

[33] M. Boca, "On the properties of the Volkov solutions of the Klein-Gordon equation," *Journal of Physics A: Mathematical and Theoretical*, vol. 44, no. 44, p. 445303, Nov. 2011. [Online]. Available: http://iopscience.iop.org/1751-8121/44/44/445303

[34] L. B. Madsen, "Strong-field approximation in laser-assisted dynamics," *American Journal of Physics*, vol. 73, no. 1, p. 57, 2005.

[35] P. C. J. Joachain, N. J. Kylstra, and R. M. Potvliege, *Atoms in Intense Laser Fields*, 1st ed. Cambridge ; New York, NY: Cambridge University Press, Jan. 2012.

[36] S. Bhardwaj, "Modeling generation and characterization of attosecond pulses," Thesis, Massachusetts Institute of Technology, 2014. [Online]. Available: http://dspace.mit.edu/handle/1721.1/91127

[37] S. Bhardwaj, S.-K. Son, K.-H. Hong, C.-J. Lai, F. X. Kärtner, and R. Santra, "Recombination-amplitude calculations of noble gases, in both length and acceleration forms, beyond the strong-field approximation," *Physical Review A*, vol. 88, no. 5, p. 053405, Nov. 2013. [Online]. Available: http://link.aps.org/doi/10.1103/PhysRevA.88.053405

[38] S. V. Yalunin, M. Gulde, and C. Ropers, "Strong-field photoemission from surfaces: Theoretical approaches," *Physical Review B*, vol. 84, no. 19, p. 195426, Nov. 2011. [Online]. Available: http://link.aps.org/doi/10.1103/PhysRevB.84.195426

[39] D. G. Arbó, J. E. Miraglia, M. S. Gravielle, K. Schiessl, E. Persson, and J. Burgdörfer, "Coulomb-Volkov approximation for near-threshold ionization by short laser pulses," *Physical Review A*, vol. 77, no. 1, p. 013401, Jan. 2008. [Online]. Available: http://link.aps.org/doi/10.1103/PhysRevA.77.013401

[40] A. S. Kornev and B. A. Zon, "Testing of Coulomb-Volkov functions," *Journal of Physics B: Atomic, Molecular and Optical Physics*, vol. 35, no. 11, p. 2451, Jun. 2002. [Online]. Available: http://iopscience.iop.org/0953-4075/35/11/304

[41] J. Itatani, F. Quéré, G. L. Yudin, M. Y. Ivanov, F. Krausz, and P. B. Corkum, "Attosecond Streak Camera," *Physical Review Letters*, vol. 88, no. 17, p. 173903, Apr. 2002. [Online]. Available: http://link.aps.org/doi/10.1103/PhysRevLett.88.173903

[42] J. P. Marangos, S. Baker, N. Kajumba, J. S. Robinson, J. W. G. Tisch, and R. Torres, "Dynamic imaging of molecules using high order harmonic generation," *Physical Chemistry Chemical Physics*, vol. 10, no. 1, pp. 35–48, Dec. 2007. [Online]. Available: http://pubs.rsc.org/en/content/articlelanding/2008/cp/b714126m

[43] X. Feng, S. Gilbertson, H. Mashiko, H. Wang, S. D. Khan, M. Chini, Y. Wu, K. Zhao, and Z. Chang, "Generation of Isolated Attosecond Pulses with 20 to 28 Femtosecond Lasers," *Physical Review Letters*, vol. 103, no. 18, p. 183901, Oct. 2009. [Online]. Available: http://link.aps.org/doi/10.1103/PhysRevLett.103.183901

[44] Z. Chang, "Controlling attosecond pulse generation with a double optical gating," *Physical Review A (Atomic, Molecular, and Optical Physics)*, vol. 76, no. 5, p. 051403, 2007. [Online]. Available: http://dx.doi.org/10.1103/PhysRevA.76.051403

[45] D. Kane, "Recent progress toward real-time measurement of ultrashort laser pulses," *Quantum Electronics, IEEE Journal of*, vol. 35, no. 4, pp. 421–431, 1999.

[46] L. Plaja, R. Torres, and A. Zaïr, Eds., *Attosecond Physics*, ser. Springer Series in Optical Sciences. Berlin, Heidelberg: Springer Berlin Heidelberg, 2013, vol.

177. [Online]. Available: http://link.springer.com/10.1007/978-3-642-37623-8

[47] A. Wirth, M. T. Hassan, I. Grguraš, J. Gagnon, A. Moulet, T. T. Luu, S. Pabst, R. Santra, Z. A. Alahmed, A. M. Azzeer, V. S. Yakovlev, V. Pervak, F. Krausz, and E. Goulielmakis, "Synthesized Light Transients," *Science*, vol. 334, no. 6053, pp. 195–200, Oct. 2011.

[48] S.-W. Huang, G. Cirmi, J. Moses, K.-H. Hong, S. Bhardwaj, J. R. Birge, L.-J. Chen, E. Li, B. J. Eggleton, G. Cerullo, and F. X. Kärtner, "High-energy pulse synthesis with sub-cycle waveform control for strong-field physics," *Nature Photonics*, vol. 5, no. 8, pp. 475–479, Aug. 2011.

[49] M. U. Wehner, M. H. Ulm, and M. Wegener, "Scanning interferometer stabilized by use of pancharatnam's phase," *Optics Letters*, vol. 22, no. 19, pp. 1455–1457, Oct. 1997. [Online]. Available: http://ol.osa.org/abstract.cfm?URI=ol-22-19-1455

[50] M. Schultze, M. Fieß, N. Karpowicz, J. Gagnon, M. Korbman, M. Hofstetter, S. Neppl, A. L. Cavalieri, Y. Komninos, T. Mercouris, C. A. Nicolaides, R. Pazourek, S. Nagele, J. Feist, J. Burgdörfer, A. M. Azzeer, R. Ernstorfer, R. Kienberger, U. Kleineberg, E. Goulielmakis, F. Krausz, and V. S. Yakovlev, "Delay in Photoemission," *Science*, vol. 328, no. 5986, pp. 1658–1662, Jun. 2010. [Online]. Available: http://www.sciencemag.org/content/328/5986/1658

[51] P. Johnsson, R. López-Martens, S. Kazamias, J. Mauritsson, C. Valentin, T. Remetter, K. Varjú, M. B. Gaarde, Y. Mairesse, H. Wabnitz, P. Saliìres, P. Balcou, K. J. Schafer, and A. L'Huillier, "Attosecond Electron Wave Packet Dynamics in Strong Laser Fields," *Physical Review Letters*, vol. 95, no. 1, p. 013001, Jun. 2005. [Online]. Available: http://link.aps.org/doi/10.1103/PhysRevLett.95.013001

[52] A. L. Cavalieri, N. Müller, T. Uphues, V. S. Yakovlev, A. Baltuška, B. Horvath, B. Schmidt, L. Blümel, R. Holzwarth, S. Hendel, M. Drescher, U. Kleineberg, P. M. Echenique, R. Kienberger, F. Krausz, and U. Heinzmann, "Attosecond spectroscopy in condensed matter," *Nature*, vol. 449, no. 7165, pp. 1029–1032, Oct. 2007. [Online]. Available: http://www.nature.com/nature/journal/v449/n7165/abs/nature06229.html

[53] E. Goulielmakis, Z.-H. Loh, A. Wirth, R. Santra, N. Rohringer, V. S. Yakovlev, S. Zherebtsov, T. Pfeifer, A. M. Azzeer, M. F. Kling, S. R. Leone, and F. Krausz, "Real-time observation of valence electron motion," *Nature*, vol. 466, no. 7307, pp. 739–743, 2010. [Online]. Available: http://dx.doi.org/10.1038/nature09212

[54] T. T. Luu, M. Garg, S. Y. Kruchinin, A. Moulet, M. T. Hassan, and E. Goulielmakis, "Extreme ultraviolet high-harmonic spectroscopy of solids,"

Nature, vol. 521, no. 7553, pp. 498–502, May 2015. [Online]. Available: http://www.nature.com/nature/journal/v521/n7553/full/nature14456.html

[55] W. A. Okell, T. Witting, D. Fabris, C. A. Arrell, J. Hengster, S. Ibrahimkutty, A. Seiler, M. Barthelmess, S. Stankov, D. Y. Lei, Y. Sonnefraud, M. Rahmani, T. Uphues, S. A. Maier, J. P. Marangos, and J. W. G. Tisch, "Temporal broadening of attosecond photoelectron wavepackets from solid surfaces," *Optica*, vol. 2, no. 4, pp. 383–387, Apr. 2015. [Online]. Available: http://www.opticsinfobase.org/optica/abstract.cfm?URI=optica-2-4-383

[56] J. Burkardt and R. Brent, "BRENT," Jul. 2011.

[57] R. P. Brent, *Algorithms for Minimization Without Derivatives*. Courier Corporation, Jun. 2013.

[58] T. Zuo, A. D. Bandrauk, M. Ivanov, and P. B. Corkum, "Control of high-order harmonic generation in strong laser fields," *Physical Review A*, vol. 51, no. 5, pp. 3991–3998, May 1995. [Online]. Available: http://link.aps.org/doi/10.1103/PhysRevA.51.3991

[59] P. Baum and A. H. Zewail, "Attosecond electron pulses for 4D diffraction and microscopy," *Proceedings of the National Academy of Sciences*, vol. 104, no. 47, pp. 18 409–18 414, Nov. 2007, PMID: 18000040. [Online]. Available: http://www.pnas.org/content/104/47/18409

[60] W. S. Graves, F. X. Kärtner, D. E. Moncton, and P. Piot, "Intense superradiant x rays from a compact source using a nanocathode array and emittance exchange," *Physical Review Letters*, vol. 108, no. 26, p. 263904, Jun. 2012. [Online]. Available: http://link.aps.org/doi/10.1103/PhysRevLett.108.263904

[61] R. H. Fowler and L. Nordheim, "Electron emission in intense electric fields," *Proceedings of the Royal Society of London. Series A*, vol. 119, no. 781, pp. 173–181, May 1928. [Online]. Available: http://rspa.royalsocietypublishing.org/content/119/781/173

[62] S. Link, C. Burda, B. Nikoobakht, and M. A. El-Sayed, "Laser-Induced Shape Changes of Colloidal Gold Nanorods Using Femtosecond and Nanosecond Laser Pulses," *The Journal of Physical Chemistry B*, vol. 104, no. 26, pp. 6152–6163, Jul. 2000. [Online]. Available: http://dx.doi.org/10.1021/jp000679t

[63] L. Velasquez-Garcia, S. Guerrera, Y. Niu, and A. Akinwande, "Uniform High-Current Cathodes Using Massive Arrays of Si Field Emitters Individually Controlled by Vertical Si Ungated FETs #x2014;Part 2: Device Fabrication and Characterization," *Electron Devices, IEEE Transactions on*, vol. 58, no. 6, pp. 1783 –1791, Jun. 2011.

[64] G. G. Paulus, W. Becker, and H. Walther, "Classical rescattering effects in two-color above-threshold ionization," *Physical Review*

A, vol. 52, no. 5, pp. 4043–4053, Nov. 1995. [Online]. Available: http://link.aps.org/doi/10.1103/PhysRevA.52.4043

[65] S. Passlack, S. Mathias, O. Andreyev, D. Mittnacht, M. Aeschlimann, and M. Bauer, "Space charge effects in photoemission with a low repetition, high intensity femtosecond laser source," *Journal of Applied Physics*, vol. 100, no. 2, p. 024912, Jul. 2006. [Online]. Available: http://scitation.aip.org/content/aip/journal/jap/100/2/10.1063/1.2217985

[66] B. J. Siwick, J. R. Dwyer, R. E. Jordan, and R. J. D. Miller, "Ultrafast electron optics: Propagation dynamics of femtosecond electron packets," *Journal of Applied Physics*, vol. 92, no. 3, pp. 1643–1648, Aug. 2002. [Online]. Available: http://scitation.aip.org/content/aip/journal/jap/92/3/10.1063/1.1487437

[67] X. J. Zhou, B. Wannberg, W. L. Yang, V. Brouet, Z. Sun, J. F. Douglas, D. Dessau, Z. Hussain, and Z. X. Shen, "Space charge effect and mirror charge effect in photoemission spectroscopy," *Journal of Electron Spectroscopy and Related Phenomena*, vol. 142, no. 1, pp. 27–38, Jan. 2005. [Online]. Available: http://www.sciencedirect.com/science/article/pii/S0368204804003421

[68] R. Arafune, K. Hayashi, S. Ueda, and S. Ushioda, "Energy Loss of Photoelectrons by Interaction with Image Charge," *Physical Review Letters*, vol. 92, no. 24, p. 247601, Jun. 2004. [Online]. Available: http://link.aps.org/doi/10.1103/PhysRevLett.92.247601

[69] J. Moses, S.-W. Huang, K.-H. Hong, O. D. Mücke, E. L. Falcão-Filho, A. Benedick, F. O. Ilday, A. Dergachev, J. A. Bolger, B. J. Eggleton, and F. X. Kärtner, "Highly stable ultrabroadband mid-IR optical parametric chirped-pulse amplifier optimized for superfluorescence suppression," *Optics Letters*, vol. 34, no. 11, pp. 1639–1641, Jun. 2009. [Online]. Available: http://ol.osa.org/abstract.cfm?URI=ol-34-11-1639

[70] J. Moses and F. W. Wise, "Controllable Self-Steepening of Ultrashort Pulses in Quadratic Nonlinear Media," *Physical Review Letters*, vol. 97, no. 7, p. 073903, Aug. 2006. [Online]. Available: http://link.aps.org/doi/10.1103/PhysRevLett.97.073903

[71] H. Qing-An, "Field emission from the surface quantum well of silicon," *Applied Surface Science*, vol. 93, no. 1, pp. 77–83, Jan. 1996.

[72] Q. Huang, "Instability of field emission from silicon covered with a thin oxide due to electron trapping," *Journal of Applied Physics*, vol. 79, no. 7, pp. 3703–3707, Apr. 1996.

[73] ——, "Field emission from a silicon surface potential well through a thin oxide," *Journal of Applied Physics*, vol. 78, no. 11, pp. 6770–6774, Dec. 1995.

[74] M. Schenk, M. Krüger, and P. Hommelhoff, "Strong-Field Above-Threshold Photoemission from Sharp Metal Tips," *Physical Review Letters*, vol. 105, no. 25, p. 257601, Dec. 2010. [Online]. Available: http://link.aps.org/doi/10.1103/PhysRevLett.105.257601

[75] C. Bourassin-Bouchet and M.-E. Couprie, "Partially coherent ultrafast spectrography," *Nature Communications*, vol. 6, Mar. 2015. [Online]. Available: http://www.nature.com/ncomms/2015/150306/ncomms7465/full/ncomms7465.html